Chair of Functional Materials and Materials Systems

Doctoral Thesis

Sputter Deposition of Multifunctional Thin Films

Dipl.-Ing. Martin Rausch, B.Sc.

October 2019

EIDESSTATTLICHE ERKLÄRUNG

Ich erkläre an Eides statt, dass ich diese Arbeit selbständig verfasst, andere als die angegebenen Quellen und Hilfsmittel nicht benutzt, und mich auch sonst keiner unerlaubten Hilfsmittel bedient habe.

Ich erkläre, dass ich die Richtlinien des Senats der Montanuniversität Leoben zu "Gute wissenschaftliche Praxis" gelesen, verstanden und befolgt habe.

Weiters erkläre ich, dass die elektronische und gedruckte Version der eingereichten wissenschaftlichen Abschlussarbeit formal und inhaltlich identisch sind.

Datum 15.10.2019

Unterschrift Verfasser/in
Martin, Rausch

“Run if you can,
walk if you have to,
crawl when you must
– just never give up.”

unknown ultramarathonist

“If you're going through hell,
keep going.”

unknown, but possibly Winston Churchill (1941)

ACKNOWLEDGEMENTS

Up and foremost, I want to thank my supervisor Prof. Dr. Christian Mitterer, head of the Department Materials Science and the Chair of Functional Materials and Materials Systems at Montanuniversität Leoben, for offering the chance to conduct the present work within his group. Thank you, for putting so much trust in me from the very beginning onwards to the end of this journey. A PhD consists of ups and downs, but you excel in offering guidance and freedom at the same time. I have learned a lot from you. Thank you!

I am most grateful to Prof. Dr. Jochen Schneider, head of the Chair of Materials Chemistry at RWTH Aachen (Germany), for offering the opportunity to conduct research at his department. Thank you for your guidance and critical point of view – I appreciate it! I owe my gratitude to Dr. Stanislav Mraz, scientist at the Chair of Materials Chemistry at RWTH Aachen, for his help and support during my stay at RWTH and his time and efforts during the publication process. Your eye for detail is incredible.

I appreciate the selfless help my mentor Prof. Dr. Megan Cordill, scientist at Erich Schmid Institute of the Austrian Academy of Sciences, offered whenever needed. I appreciate your attitude to get things done without compromise and your courage and vision.

Next, I have to thank my colleagues at the Department Materials Science for offering a relaxed, yet incredibly productive work environment. I have enjoyed spending time with all of you. However, especially grateful I am to Veli and Anna, who shared the office with me, and Mehran, Niki, Sari, and Stefan. You guys made the downs of the work feel like vacation. You are simply the best and without you, I would have not enjoyed work half the way I did. I want to thank Patrice for scientific discourse and selfless help, whenever needed – your SEM and FIB skills are amazing! Thank you. I also owe gratitutde to Asaf Sabag, former student of ORT Braude College of Engineering (Israel), who did an amazing job in film characterization and therefore contributed to large parts of the current thesis. I appreciate your diligence and hard work, thank you for everything.

At this point, I want to gratefully acknowledge Dr. Jörg Winkler, Dr. Judith Köstenbauer and Dr. Harald Köstenbauer from Plansee SE, for providing valuable input and discussions during project meetings over the last 2.5 years. Your input always took me a step further. Thank you for that!

Meinen Eltern Heidi und Gerhard bin ich für immer für ihre kompromisslose Liebe dankbar. Ohne eure Unterstützung und Kritik wäre ich nicht da, wo ich bin. Ihr habt mir die Basis mitgegeben, auf die ich heute bauen kann. Meiner Schwester Katharina und meinem Schwager Niklas möchte ich hier auch Danke sagen. Ihr seid unglaublich tolle Menschen, auf die man immer zählen kann. Daher, werte Familie: Vielen Dank für alles, ich hab‘ euch lieb!

My best friends Max and Carmen must be mentioned here. Max, you are more like a brother to me. You have always been here, no matter there was need or not. I am most grateful for our friendship, which will accompany us doubtlessly for the rest of our lifes. Carmen, thank you for being such an amazing and wearm-hearted person!

Last, but definitely not least, I want to thank my partner Lisa for her support and love. I am aware of the drawbacks a daily commute from Graz to Leoben means for a partnership. However, I am also aware that mastered obstacles ultimately bring us closer together. You are the best partner I could wish for and I want to spend my life with you. Thank you for being by my side – I love you.

TABLE OF CONTENTS

1. Introduction....1
2. Magnetron sputter deposition....2
2.1 Vapor generation 4
2.2 Transport through the gas phase 7
2.3 Film growth 9
3. Thin film deposition 13
3.1 Sputter deposition on industrial-scale 13
3.2 Sputter deposition on laboratory-scale 14
4. Simulation and modeling of sputter deposition 16
5. The sputter performance of an industrial-scale planar Mo-target over its lifetime: target erosion and film properties 18
5.1 Introduction.... 18
5.2 Experimental details.... 19
5.2.1 Target erosion 19
5.2.2 Thin film deposition 20
5.2.3 Thin film characterization 22
5.3 Results and discussion.... 23
5.3.1 Target erosion 23
5.3.2 Thin film characterization 27
5.4 Conclusions.... 38
6. Sputter deposition of Mo-based multicomponent thin films from rotatable targets: experiment and simulation.... 39
6.1 Introduction.... 39
6.2 Experimental and theoretical methods 40
6.2.1 Thin film deposition 40
6.2.2 Thin film characterization 41
6.2.3 Simulation and modeling 41
6.3 Results and discussion.... 42
6.3.1 Thin film deposition 42
6.3.2 Chemical composition 46
6.3.3 Film morphology 48
6.3.4 SRIM simulations.... 50

6.4 Conclusions 55

7. Angular resolved mass-energy analysis of species emitted from a d.c. magnetron sputtered NiW-target 56

7.1 Introduction 56

7.2 Experimental methods 57

7.2.1 Angular resolved plasma characterization 57

7.2.2 Thin film deposition 59

7.2.3 Thin film characterization 59

7.3 Results and discussion 60

7.3.1 Angular resolved plasma characterization 60

7.3.2 Angular resolved thin film deposition 67

7.3.3 Correlation of MEA-measurements with thin film growth 69

7.4 Conclusions 71

8. Sputter deposition of NiW films from a rotatable target 72

8.1 Introduction 72

8.2 Experimental details 73

8.2.1 Thin film deposition 73

8.2.2 Thin film and target characterization 74

8.2.3 Simulation 75

8.3 Results 76

8.3.1 Thin film deposition 76

8.3.2 Target characterization 78

8.3.3 Simulation 79

8.4 Discussion 79

8.5 Conclusions 83

9. Conclusions and outlook 85

References 87

1. INTRODUCTION

Around 5,000 years ago, Egyptians were the first to produce decorative inorganic thin films by beating Au to thicknesses < 3,000 Å [1]. Over the centuries, various techniques were developed that allowed the growth of other thin films. Among these techniques was Egyptian "cold mercury" gilding [2], allowing the growth of copper/mercury amalgam as adhesion layer for press-bonding of gold leaf on a copper substrate, and electroless plating [3], developed by the Moche Indians around 100 BC allowing the growth of Au coatings on Cu artifacts. With the development of vacuum and electrical power technologies in the 1600s and 1700s however, the development of modern thin film deposition techniques became available [4]. One of those techniques, based on vacuum and electrical power technologies and developed in the 1800s, is direct current diode sputter deposition. The combination of direct current diode sputter deposition with magnetic fields in the 1920ies increased the efficiency of the process significantly and gave rise to a technique called magnetron sputter deposition (MSD). MSD is a form of physical vapor deposition (PVD), which allows depositing thin films of nearly all classes of source materials, both liquid and solid [5].

2. Magnetron sputter deposition

MSD is widely used to grow thin films used for microelectronics-, solar-, and display-applications or for cutting tools [6,7]. These films are applied as diffusion barriers, metallization and dielectric layers or tribological and optical coatings [8]. MSD utilizes the kinetic energy of gas ions that bombard the surface of a target, where consequently target atoms are emitted. These atoms travel towards a suitable substrate and form a film [9]. Most commonly, Ar is used as background gas [10] because of its relatively high natural abundance and an atomic mass that is suitable to effectively sputter erode a large variety of materials [11].

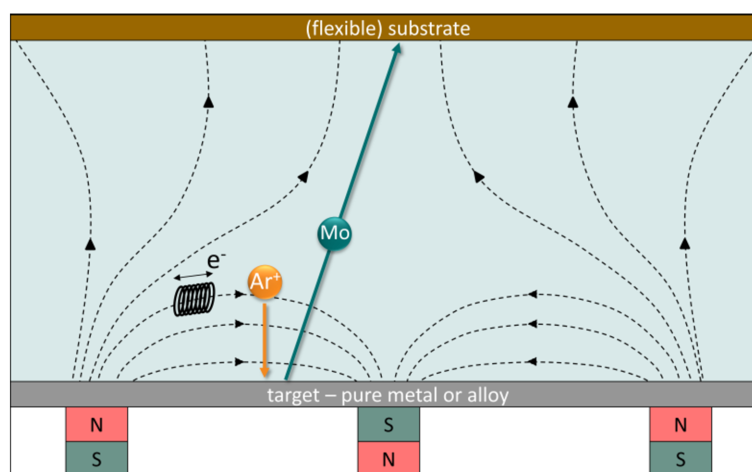

Figure 1: Schematic representation of an unbalanced magnetron sputtering system, based on the work of Sproul [12]. Permanent magnets located behind the target induce a magnetic field that predominantely influence the trajectory of electrons. Inelastic collisions of electrons with Ar neutrals locally increase the number of Ar^+ ions. These Ar^+ ions bombard the target, from which metal atoms are sputtered. After their transport through the gas phase, the sputtered atoms condense on a substrate located opposite the target. Note that the strength of the inner and outer magnets is unbalanced in order to keep parts of the magnetic field lines open pointing towards the substrate carrier.

The basic principle of MSD is as follows: An electrically isolated magnetron (consisting of the target of the desired coating material, magnet bars and cooling elements that are located behind the target) is placed in a grounded vacuum chamber opposite a substrate carrier. After evacuating the chamber to a sufficient base pressure $\lesssim 10^{-3}$ Pa, a constant Ar flow leads to a dynamic vacuum with an Ar pressure of 0.1 to 10 Pa. Between target and grounded vacuum chamber, a potential difference of some hundred volts (U_{dc}) with currents of 0.1 to some ten amperes (I_{dc}) is applied. That potential difference leads to a partial charge separation of Ar atoms to Ar^+ ions and electrons e^- and the formation of a quasi-neutral plasma with an degree of ionization $\lesssim 1\%$ [13]. Due to the applied negative potential on the target, some of the Ar^+ ions are extracted from the plasma and bombard the target surface, causing the emission of target atoms (Figure 1).

The magnetic field lines (B) of the permanent magnets located behind the target affect the movement of electrons and force them into circular motion due to the Lorentz force ([9], Figure 1). With an electric field E applied between target and substrate carrier, the $E \times B$ drift leads to an additional circular or elliptical drift movement of the electrons over the target area. Where the E×B drift confines the electrons, an increased number of inelastic collisions of electrons with Ar results in an increased number of Ar^+ ions $N(Ar^+)$ [9] and the formation of an erosion groove on the target surface, limiting target utilization and lifetime [14]. However, in contrast to direct current diode sputter deposition, the increased number of Ar^+ ions in MSD leads to higher deposition rates and the concentration of electrons in front of the target to decrease the substrate temperatures [9].

Considerable efforts have been put into the optimization of the ratio of E and B and to correlate erosion groove depth with film properties [15–23]. However, although being studied extensively on laboratory-scale and via computer simulations, only little is known on the effect of an erosion groove formed on industrial-scale rectangular planar targets on the properties of films deposited at different stages of target usage. Therefore, one of the aspects investigated within this thesis is the effect of the evolution of an erosion groove on film properties and its relevance on the MSD process stability.

As stated and exemplified by the author of this thesis [24], besides the need for high process stability, an increasing technological demand for films that fulfill specific needs is noticeable. Single-element films can no longer satisfy some of those needs. Therefore, the use of multi-element systems becomes necessary. For basic research on a laboratory-scale, these films are often deposited via co-sputtering from the respective single element targets. On an industrial-scale, films are commonly grown from multi-element targets. Compared to co-sputtering from single element targets, these multi-element targets ensure the required process stability on a large scale [25–27]. However, the complexity of the process increases when more elements are involved in the deposition process – which can also affect the final film properties. Therefore, the behavior of multi-element systems has been the focus of extensive research over the last years [25,27–49], but to date hardly any general rules can be drawn for the deposition behavior when sputtering multi-element targets. Compared to the target composition, either light [27–37] or heavy elements are enriched within the film [25,38–49]. The reported results are on the first sight contradicting and represent the complexity of sputtering of multi-element systems.

According to Bunshah [50], MSD can be separated into three interlinked processes, each of which distinctly influencing final film properties, namely: (*i*) the emission of particles from the target (vapor generation), (*ii*) the transport of those particles from target to substrate (transport through the gas

phase), and (*iii*) the condensation of those particles on the substrate (film growth). The current thesis systematically investigates the respective influence of those three processes on the final properties of films grown from multi-element targets.

2.1 Vapor generation

According to Sigmund [51], the dominant process causing sputtering is a momentum transfer from energetic gas ions to atoms within the target. This momentum transfer can lead to sputtering of target atoms, with typical emission depths of some atomic layers below the surface [50]. Depending on the initial energy of the impinging Ar^+ ions (E_{Ar}), three different sputtering regimes have to be distinguished (Figure 2): According to Westwood [9], for $E_{Ar} \lesssim 300$ eV, single knock-on sputtering leads to direct emission of surface atoms (Figure 2 (a)). In that case, a target atom has received a certain amount of energy from an impinging Ar^+ ion and is directly emitted. For $E_{Ar} \gtrsim 300$ eV, the momentum from an impinging Ar^+ initiates a linear collision cascade between target atoms (Figure 2 (b)). This collision cascade leads to sputtering of surface atoms, when its initial direction is sufficiently changed and enough of its energy is conserved throughout the ongoing collisions. For $E_{Ar} > 1{,}000$ eV, multiple collision cascades within the target develop simultaneously, leading to thermal "spikes" [5]. Since E_{Ar} in magnetron sputtering (with its dominating fraction of single-charged ions) directly relates to the applied target voltage of some hundred volts ($\mathrm{E_{Ar}} \cong \mathrm{U}_{dc}$), the spike regime is not relevant for MSD and therefore not discussed here in further detail.

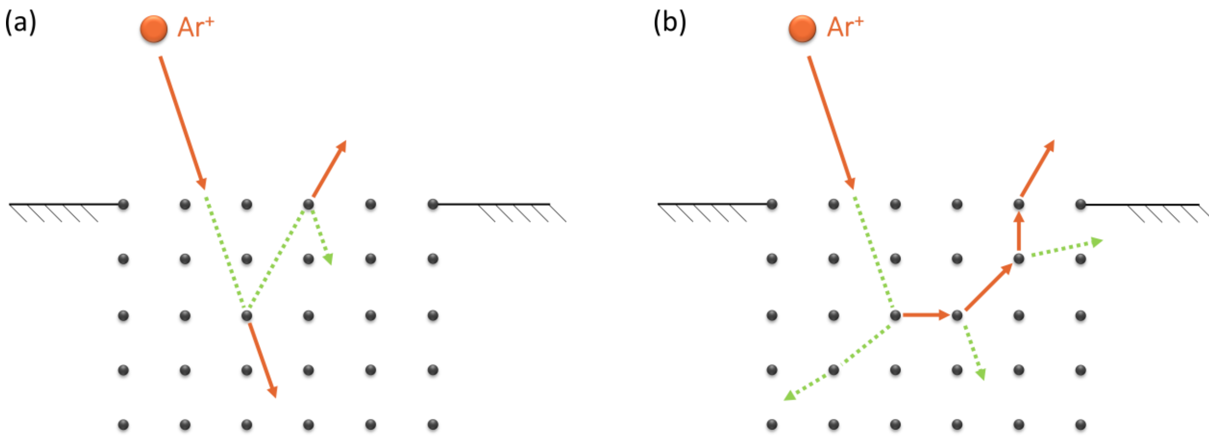

Figure 2: Schematic representation of sputter mechanism in the (a) single knock-on ($E_{Ar} \lesssim 300$ eV) and (b) the linear-cascade regime ($E_{Ar} \gtrsim 300$ eV) after Sigmund [51].

The sputter yield (Y), defined as the number of sputtered atoms per incident particle, quantifies the efficiency of sputtering processes [5]. It directly depends on the target element and its specific surface binding energy (E_b, corresponding to the heat of sublimation U_{sb}), the ion's energy (E_{Ar}), the ratio of

ion to target atomic mass (m_{Ar}/m_M), and the ion's incidence angle (θ) [9] – factors that will be discussed in the following.

As evident from Figure 3(a), an increase of Ar⁺ ion energy leads to an increase of the sputter yield for all shown elements Ag, Cu, Ni, Mo, Ti and C, as published by Maissel *et al.* [52]. However, the increase of Y is element-specific and correlates with the respective surface binding energies of the particular elements [11]. Elements with low surface binding energies in general show high sputter yields, since less energy is needed to overcome the binding force of neighboring atoms to emit an atom from the surface, with a reverse trend for elements with high surface binding energies. However, not only the binding energies, but also the ratio of atomic mass of ions and target constituents determines the resulting sputter yield. The effective energy transfer coefficient for head-to-head collisions ε specifies the amount of energy that is transferred between two colliding atoms [31] and is defined as

$$\varepsilon = \frac{4m_{Ar} \cdot m_M}{(m_{Ar} + m_M)^2} . \qquad (1)$$

The closer the masses of ions and target atoms match, the higher the effective energy transfer is. In the case of vapor generation, high ε values mean that more of the ions' initial energy is transferred to target atoms. Therefore, when $m_M \simeq m_{Ar}$, target atoms have more energy to overcome the surface binding energy and higher kinetic energies in the plasma compared to the case when $m_M \not\simeq m_{Ar}$.

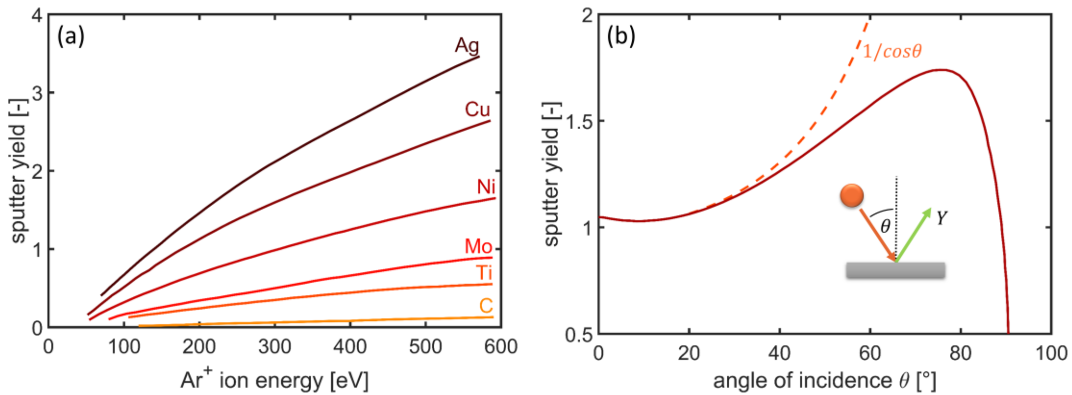

Figure 3: (a) Sputter yield of Ag, Cu, Ni, Mo, Ti and C, bombarded with Ar⁺ ions parallel to the target normal of varying energy, after [52]. (b) Schematic representation of the evolution of the sputter yield for oblique incidence of Ar⁺ ions of constant energy. θ defines the incidence angle from the target normal.

When Ar⁺ ions hit the target surface, a certain amount of kinetic energy (E_k) is transferred to target atoms. For a target atom of given kinetic energy E_k, the probability to overcome the surface binding energy is higher when it is emitted close to the target normal compared to an emission at oblique angles [11]. Since the energy of a particle within a collision cascade in the target moving with a velocity

v is given by $E_k = 1/2\, mv^2$, the velocity of the particle can be split into a component parallel ($v_\parallel = v\, cos\theta$) and a component perpendicular ($v_\perp = v \sin\theta$) to the target normal. A sufficient condition for sputtering of a surface particle in the collision cascade with $v_\parallel$ and the corresponding energy $E_\parallel$ is that $E_\parallel > E_b$. The relation between $E_\parallel$ and total particle energy E_k is given by

$$E_\parallel = \frac{1}{2} m(v \cdot \cos\theta)^2 = \frac{1}{2} mv^2 \cos^2\theta = E_k \cos^2\theta. \qquad (2)$$

Therefore, sputtered particles are usually emitted in a $\cos^n\theta$ distribution, with $n > 1$ [9]. However, deviations from this distribution have been observed with respect to Ar^+ ion energies [53], the crystallographic orientation of the target [54], and the target surface roughness [55], so that the emission profiles can be either “over-cosine” or “under-cosine”, with the preferential emission angles being closer or further to/from the target normal, respectively. An “under-cosine” distribution is also referred to as “heart-shaped” [9].

The kinetic energy of atoms emitted from the target can reach values of some ten eVs [5]. The energy distributions functions of sputtered atoms are close to the Maxwell-Boltzmann distribution of energy for thermal gas atoms [10] shifted towards higher energies, with a high-energy tail up to 50-100 eV that decays with $1/E^2$ [11]. The energy distribution functions of sputtered atoms at fixed emission angle usually show a peak energy E_{peak} of some eVs, as defined in Equation 3, with E_b being the specific surface binding energy and i a constant that varies between i = 0.2-0.3 for ion energies E_{Ar} > 1 keV and i = 0 for $E_{Ar} \sim E_b$ [51].

$$E_{peak} = \frac{E_b}{2(1-i)} \qquad (3)$$

Considerations so far were based on an Ar^+ ion incidence angle parallel to the surface normal, i.e. under an angle θ = 0°, which is reasonable for MSD. Due to the plasma properties, in close proximity to the target (where the negative potential is applied), a sheath region develops that is commonly referred to as dark space and virtually separated from the bulk plasma region. Within that dark space, the entire voltage drop occurs between the bulk plasma region and the target (with a negative potential of some hundred volts). In that region, Ar^+ ions are accelerated to energies corresponding to the applied potential, before hitting the target surface in an angle parallel to the local target surface normal [11]. Therefore, an Ar^+ ion incidence angle of θ = 0° in general applies for magnetron sputtering [9]. However, as will be outlined in more detail in the following chapters, a certain surface roughness can develop over target usage – especially when sputter eroding multi-element targets. This surface

roughness can locally cause sputtering under oblique angles. When the Ar^+ ion incidence angle changes from θ = 0° up to 70° [9], a rise of Y comes along that roughly scales with $1/cos\theta$ [56], as schematically shown in Figure 3(b). When the ions hit the target under oblique angles, the interaction volume of the collision cascade stays closer to the surface. Therefore, more energy is available for surface atoms to overcome the surface binding energy, and the sputter yield increases. For an Ar^+ incidence angle θ > 80°, ions tend to be reflected from the target surface rather than to induce a collision cascade [11] and Y displays a sharp drop, as evidenced by Figure 3(b).

Besides sputtering, energetic ion bombardment of a surface can also lead to the reflection of Ar^+ ions as Ar neutrals from the target – even when the incidence angle of Ar^+ is close to the target normal. In general, Ar^+ ions that approach the target surface are neutralized by electrons from the near-surface region [11]. When $m_{Ar} \ll m_M$, a considerable amount of impinging Ar^+ ions can therefore be reflected as Ar neutrals, with the number of reflected Ar neutrals scaling with m_M. According to Drüsedau [57], up to 25 % of Ar^+ ions hitting the target are reflected as neutrals from a Mo target, whereas up to 40 % are reflected from a W target. It is worth noting that those reflected Ar neutrals are not affected by any potential difference in the plasma and therefore maintain considerable amounts of kinetic energies, corresponding up to the initial energy of the Ar^+ ions before hitting the target surface [9].

2.2 Transport through the gas phase

Atoms that are sputtered from the target surface with a given angular and energy distribution function have to travel through the bulk plasma region before arriving at a given substrate, where the desired film is grown. In MSD, this target-substrate distance d is usually in the cm range [11]. Depending on the used Ar pressure, which usually ranges between 0.1 and 10 Pa, the sputtered particles experience a defined number of collisions with Ar background gas atoms that lead to scattering. Since the kinetic energy of the background gas atoms relates to the deposition temperature as $E_k = \frac{3}{2} k_B T$, with Boltzmann's constant (k_B) and temperature (T, corresponding to the kinetic energy of the thermal Ar background gas atoms), the kinetic energy of Ar background gas atoms is only 0.05 eV for an assumed deposition temperature of 400 K [49]. Therefore, Ar background gas atoms are commonly considered static compared to sputtered atoms with energies of some ten eVs. Moreover, as stated by Depla et al. [58], it can be assumed that scattering of the sputtered particles is dominated by elastic collisions with neutral background gas atoms and no collisions with other metal atoms take place, since the overall number of sputtered atoms is negligibly small compared to the number of background gas atoms. It is hence justified for further considerations that only collisions of metal with Ar atoms are taken into account.

The concept of the thermal mean free path (λ), as described by Equation 4 with gas pressure (p) and atomic radii (r_{Ar}, r_M), allows to obtain insights into the average number of collisions a sputtered atom undergoes during the transport through the bulk plasma region [35]. The mean free path expresses the average distance an arbitrary sputtered atom can travel between two subsequent collisions with background Ar atoms. Increased temperatures as well as low gas pressures allow atoms to travel farther without collision. The average number of collisions a sputtered particle experiences on its way from the target to the substrate is defined as $N = d/\lambda$, with high Ar pressures increasing the number of collisions.

$$\lambda = \frac{1}{\sqrt{2}} \cdot \frac{k_B \cdot T}{p} \cdot \frac{1}{\pi \cdot (r_{Ar} + r_M)^2} \qquad (4)$$

The amount of energy that is effectively transferred in any of those collisions is defined by Equation 1 in section 2.1, with the most effective energy transfer for atoms of equivalent mass. The maximum possible scatter angle between two particles of different mass ($\theta^{\max}$, stemming from classical mechanics of elastic collisions [59]) is defined in Equation 5, with the mass of the metal atom in motion (m_M) and the mass of the Ar atom at rest (m_{Ar}). When $m_M < m_{Ar}$, sputtered atoms can be scattered in any direction. In contrast, when $m_M > m_{Ar}$ the scatter angle is $0 < \theta^{\max} < 90°$ from the initial trajectory, with light elements ($m_M > m_{Ar}$) being deflected more than heavy elements ($m_M \gg m_{Ar}$).

$$sin\theta^{max} = \left.\frac{m_{Ar}}{m_M}\right|_{m_M \geq m_{Ar}} \qquad (5)$$

From above considerations, it is evident that any collision of sputtered particles with Ar background atoms influence their respective trajectory and kinetic energy. However, as already pointed out, the deposition pressure plays a crucial role in determining the number of collisions a sputtered atom undergoes on its way from the target to the substrate. Therefore, according to Rossnagel [29], three pressure-dependent regimes can be distinguished in MSD, namely: (*i*) a ballistic, (*ii*) an intermediate, and (*iii*) a diffusive regime. The ballistic regime is characterized by low pressure, $\lambda \gg d$, and $N \ll 1$. Therefore, the sputtered particles do not collide with any background atoms and their initial emission angles and energies are conserved throughout their journey from target to substrate. This in reverse means that the ballistic regime is directional, with films being grown only in a line-of-sight. Since the deposition conditions are rather energetic [11], films grown in ballistic mode are usually dense and small-grained, showing compressive stresses. Moreover, since conditions are kinetic and not thermal, metastable films can be grown [8]. In the intermediate regime, a slightly increased deposition pressure solely influences the trajectory and energy of atoms with $m_M < m_{Ar}$, which selectively scatters light

elements. Therefore, films grown from multi-element targets with constituents of considerable difference in atomic mass in the intermediate regime are usually depleted with respect to the light element. Compared to the ballistic regime, films tend to be denser [9]. In the diffusive regime, all sputtered atoms have undergone several collisions on their way from target to substrate, since $\lambda \ll d$ and $N \gg 1$. With every collision, their respective kinetic energy lowers, so that in the end they are thermalized – they only possess the thermal energy of the surrounding gas. In that regime, growth conditions are closer to thermal evaporation, with films usually showing large grains and tensile stresses [11].

2.3 Film growth

Atoms that were successfully transmitted through the gas phase eventually hit the substrate surface. Here, they either condense to form a loosely adsorbed adatom or are directly reflected ([9,60], Figure 4). The sticking coefficient relates the number of atoms that remain on the substrate to the number of reflected particles. A maximum value of the sticking coefficient of one means that all transmitted atoms remain on the substrate. Adatoms on the substrate surface in general show a certain mobility that depends on the energy and species of the adatom, the species of the substrate, and the substrate temperature [10]. That mobility allows adatoms to diffuse over the surface, so that they are eventually trapped at low-energy sites or re-sputtered by impinging atoms with sufficiently high energy [5]. According to Mattox [10], low-energy sites suitable to trap adatoms could be steps or scratches, lattice defects (such as point defects, grain boundaries or foreign atoms), or surface areas showing different chemistry or crystallographic orientations. Moreover, when diffusing over the surface, two adatoms could meet – which could also happen when an incoming atom from the plasma directly hits the diffusing atom at sufficiently low energy, so that re-sputtering is hindered. In both cases, nucleation may take place, which means that clusters of several atoms (called nuclei) form. These nuclei form the basis for further incorporation of other adatoms, so that finally islands of deposited material form on the substrate to reduce the surface free energy [9].

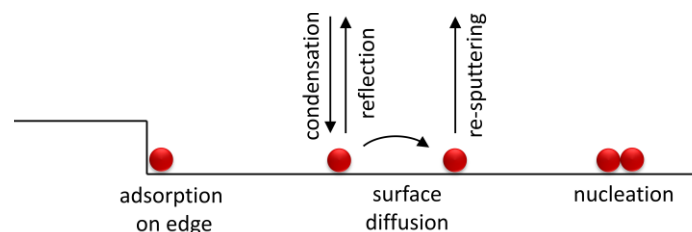

Figure 4: Schematic representation of adatom processes on the substrate surface, after [60].

According to Venables [61], these islands can behave in different ways, since different species of adatoms show different attraction to other adatoms and substrate atoms. Depending on the respective contribution of these two factors, different film growth modes can be distinguished, namely (*i*) Volmer-Weber, (*ii*) Stranski-Krastanov, and (*iii*) Frank-van der Merwe, as schematically shown in Figure 5. When adatoms are more attracted to each other than to substrate atoms, the Volmer-Weber or island growth mode is predominant. When adatoms are stronger bound to the substrate than to each other, the Frank-van der Merwe or layer-by-layer growth mode results. The Stranski-Krastanov or layer-plus-island growth mode displays an intermediate regime, with both layers and islands formed simultaneously. With respect to the particular growth mode a material exhibits on a given substrate and the specific substrate properties (like surface roughness and temperature), different film properties develop with increasing film thickness [10]. Films grown on a flat substrate at elevated temperature in island or layer-plus-island growth mode tend to show a dense columnar morphology, with grains growing like logs that are aligned to each other. Films grown on a rough surface at low temperature also show a columnar structure, however due to geometrical shadowing effects and decreased adatom mobility, these columns are further separated than in the former case. Shadowing means that peaks of the rough substrate receive more adatoms than valleys of the substrate, which lets the film on peaks grow faster. This shadowing can be exacerbated when the atom flux from the plasma is at oblique angles, leading to porous films [8].

From above findings, it is evident that processes on an atomic scale influence the macroscopic appearance of a thin film. Therefore, great effort has been put into the systematic study of the influence of deposition conditions on the final film structure, which ultimately led to the development of so called structure zone models (SZM), as outlined below.

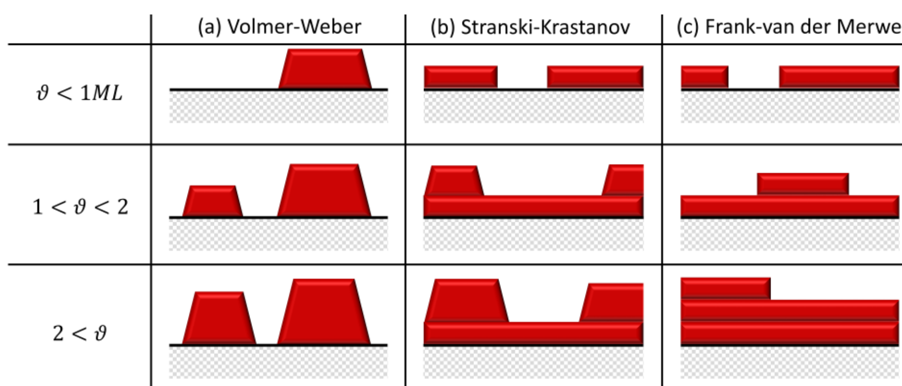

Figure 5: Schematic representation of three different thin film growth modes in dependence of the surface coverage ϑ with respect to the number of multilayers (ML) formed, based on the work of Bauer [62], adapted from Venables [61].

First proposed by Movchan and Demchishin for thick evaporated films [63] and adapted to MSD by Thornton [64], structure zone models relate deposition conditions with film properties. Both models are based on the homologous temperature $T_h = T/T_m$, with substrate temperature T and melting temperature of the coating material T_m (both in Kelvin). In contrast to the model of Movchan and Demchishin, the work of Thornton also includes the Ar pressure, which (as was discussed in section 2.2) eventually decreases the energy of sputtered atoms via collisions and influences respective film growth conditions. Therefore, Anders [65] changed Thornton's linear pressure axis to a logarithmic axis for the normalized energy E^*, making the SZM more universally applicable. E^* represents the sum of kinetic energy of impinging atoms and relates it to ε. Moreover, Anders proposed to change the linear T_h axis with a generalized temperature T^*, which also includes a contribution of potential energy to the homologous temperature. Last, the so far parameterless z-axis was replaced by a net-film thickness t^*, leading to the SZM shown in Figure 6. In contrast to the other SZMs, Anders' SZM can therefore also be extended towards high-energy conditions, leading to re-sputtering or even ion etching of the film.

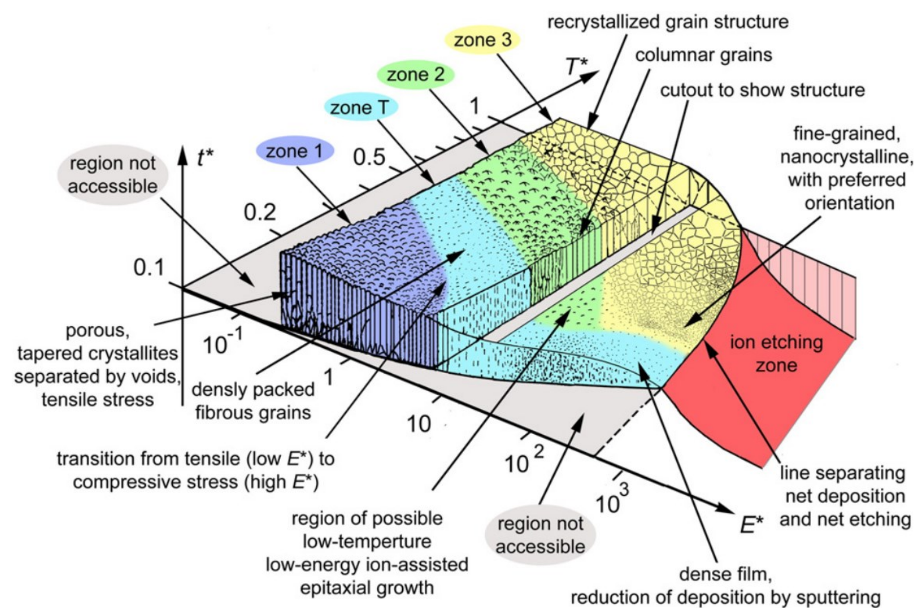

Figure 6: Structure zone model proposed by Anders [65].

Different growth conditions lead to films with varying properties. In general, Ander's SZM can be separated – as Thornton's SZM – into four growth regimes, namely (*i*) zone 1, (*ii*) zone T, (*iii*) zone 2, and (*iv*) zone 3. Films grown in zone 1 are porous and under-dense with a high surface roughness, due to shadowing effects and low energetic growth conditions in combination with low T^*, basically immobilizing adatoms [5]. Zone T films represent a transition from zone 1 to zone 2 when

T^* and/or E^* is increased. Films grown in zone T have a smooth surface and show a fibrous morphology that is increasingly dense, since the adatom diffusion is slightly increased preventing the formation of pores. However, the average grain size tends to be smaller than for zone 1 films [9,10]. In zone 2, the film growth is governed by adatom diffusion, leading to films with densities corresponding to bulk materials. However, the columnar morphology remains, although the grain size is slightly increased again compared to zone T films. This columnar morphology leads to faceted surfaces of the single columnar grains, separated by dense boundaries. Films grown in zone 3, which are prone to recrystallization due to bulk diffusion, show equiaxed recrystallized grains.

3. Thin film deposition

Experiments for the current thesis were either conducted in an industrial-scale in-line magnetron sputter system of type FHR Line.600 V or in a custom-built DN160 six-way cross vacuum chamber. In both cases, Ar was used as working gas at pressures ranging from 0.09 to 1.07 Pa. Both devices were operated in direct current (d.c.) mode with varying power densities, depending on the particular aim of the experiment. When films were grown, (100) Si wafers were used as substrates that were ultrasonically cleaned in ethanol or isopropanol for 10 min prior mounting on the substrate carrier with Kapton tape. Before each deposition, a plasma etch step was carried out for substrate cleaning and surface activation to increase film adhesion.

3.1 Sputter deposition on industrial-scale

In general, the industrial-scale magnetron sputter system of type FHR Line.600V is used for microelectronic and solar cell applications in industry. It consists of a load lock chamber separated from a process chamber by a gate valve (Figure 7). The cylindrical load lock chamber allows applying substrates on both sides of the electrically grounded and by 360° tiltable substrate carrier, without breaking vacuum of the process chamber. The carrier allows a maximum substrate size of 500 × 500 mm² with the substrates being transported and coated in an upright position. When the base pressure of the load lock chamber is < 1×10^{-3} Pa, the gate valve opens and the substrate carrier moves in front of a radio frequency (r.f.) source (Advanced Energy Cesar 1310) for a plasma etch step. Subsequently, films can either be grown from a rectangular planar target with dimensions 600 × 125 × 14 mm³ (shown in green in Figure 7) or from a cylindrical rotatable target with dimensions Ø 152 × 600 mm (shown in red in Figure 7), both powered by a d.c. power supply (Advanced Energy Pinnacle 20 kW). For a new and uneroded target the target-substrate distance for both targets is 75 mm. Depending on the desired film properties, depositions can be carried out with no substrate carrier movement (static deposition) or with the substrate carrier oscillating in front of the source (oscillated deposition) at a chosen velocity. Depositions are conducted with no further substrate heating, although thermoelement measurements showed a significant increase of substrate temperature during deposition to more than 300 °C within 3 min for a target power of a rotatable Mo target of 10 kW [7]. According to Westwood that temperature rise stems from the bombardment of the substrates with high energetic particles [9].

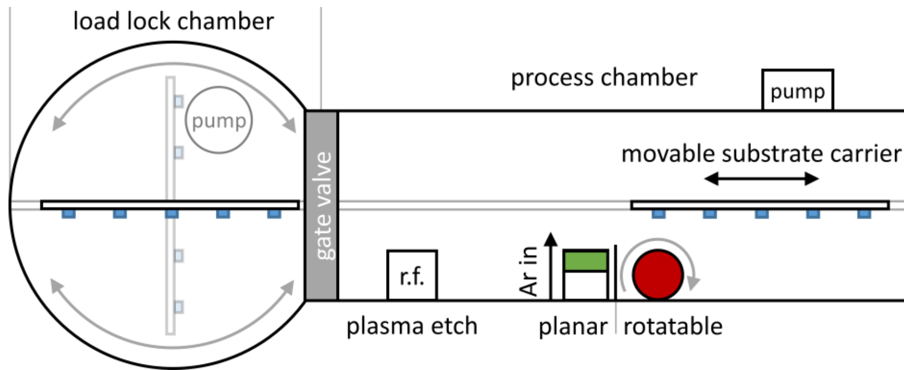

Figure 7: Schematic top view of an industrial-scale in-line magnetron sputter system of type FHR Line.600 V.

3.2 Sputter deposition on laboratory-scale

The used laboratory-scale magnetron sputter system is based on a DN160 six-way cross, evacuated by a combination of rotary-vane and turbomolecular pump. The particularity of the used system is its custom-built magnetron tiltable by +/- 90°, as schematically shown in Figure 8. A differential pumped mass-energy analyzer (MEA, Pfeiffer Vacuum plasma process monitor PPM 422) was mounted exactly opposite the target on the target axis at a distance of d = 80 mm. That combination of tiltable magnetron with static MEA allowed to assess the (*i*) nature of species present in the plasma and (*ii*) their respective ion energy distribution functions (IEDF) at any angle θ = ± 90° from the target normal. The Ar pressure could be varied between 0.09 and 1.07 Pa. The lowest pressure represents ballistic conditions for particles travelling from target towards MEA, making the emission profiles of the used target materials directly accessible.

Mass-energy analyzer measurements are based on the mass-to-charge ratio (m/z) of arbitrary particles. Therefore, it is of vital importance that the desired particles possess a charge different to zero, since neither ion optics nor mass-energy analyzer can interact with neutrals. In the used setup, particles may enter the MEA through a grounded 0.1 mm diameter orifice. Already charged particles are focused by a first set of ion optics. Neutrals in principal could be ionized via electron impact ionization in the ionization chamber afterwards and focused by subsequent ion optics (Figure 8). However, due to the small collision cross-section of electrons and particles at the energies common in MSD (up to some ten eVs), no sufficient ionization rates of neutral particles could be achieved, as observed before by Zeuner *et al.* [66]. Therefore, only IEDFs of charged particles stemming from the plasma were recorded.

An electrostatic cylindrical mirror analyzer (CMA) with a resolution of 0.3 eV was used to filter particles of set energy from -512 to +512 eV. A quadrupole mass analyzer (QMS) allowed to selectively measure

particles with a set m/z-ratio from 1 to 512. A secondary electron multiplier was used to read the ion current. The resulting signal was recorded with the Pfeiffer Quadstar software package, yielding RAW data files that were subsequently converted to x-y ASCII data.

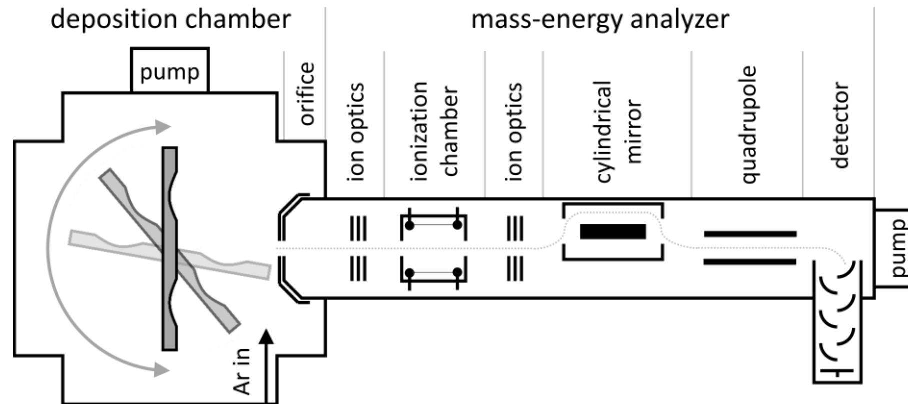

Figure 8: Schematic representation of the magnetron sputter system used for mass-energy analyzer (MEA) measurements. The left cross represents the deposition chamber with a +/- 90° tiltable magnetron. The right part represents the assembly of the mass-energy analyzer, with the grey dashed line displaying the path of the ions in the MEA.

The measurements done at each investigated angle usually comprise of (*i*) an energy-scan of $^{40}Ar^{+}$ to determine its specific energy with the highest signal intensity (I_{peak}), followed by (*ii*) a mass-scan at this specific energy to determine which species are present in the plasma. Subsequently, (*iii*) energy-scans of the target isotopes with the highest natural abundance are recorded. To exclude any experimental drift, a succeeding (*iv*) mass-scan is performed at the specific energy determined in (*i*) and compared to the data recorded in (*ii*). In the current thesis, this comparison did not show any deviation of (*iv*) to (*i*). Therefore, within this thesis only a single dataset of (*i*) is shown.

Besides MEA measurements, the magnetron sputter system can also be used for angular resolved film depositions. There, a spherical shell substrate holder with Ø = 70 mm with samples positioned at θ = ± 80° from the target normal in steps of 10° replaces the mass-energy analyzer. That approach allows directly correlating MEA measurements with film growth experiments.

4. Simulation and modeling of sputter deposition

Popular computer simulation methods currently used in materials science include (*i*) molecular dynamics (MD, [67]), (*ii*) density functional theory (DFT, [68,69]), and (*iii*) Monte-Carlo (MC, [70]) simulations. MD mainly yields insight into the motion of molecules obeying Newton's equations of motion [71], whereas DFT is often used to calculate and predict material properties for material development [72]. MC makes use of repeated random sampling of quasi-similar experiments to yield statistically significant numerical results and is therefore often applied for systems that are too complex to be solved otherwise [70]. For the current thesis, the method of choice to investigate the behavior of multi-element targets on an industrial-scale was MC.

The Scattering and Range of Ions in Matter (SRIM) is a software package initially developed by Biersack and Ziegler to simulate the range and trajectories of ions being implanted into solid materials with energies in the keVs range [73]. However, over the years it has been adapted to suit also the needs of low energy processes to simulate sputtering of surface atoms [74]. SRIM bases on the MC method and simulates binary nuclear collisions of arbitrary particles (with concomitant energy transfer and change of direction) with straight free-flight-paths in between the collisions. In general, SRIM is capable of simulating both sputtering and transport processes.

Depending on the desired statistical significance of the simulation, SRIM follows a large number of particles with basically identical starting conditions emitted from a source towards a defined amorphous target, which could be a sputter target or the bulk plasma region. Basically identical starting conditions in the current context mean that the ion's lateral starting position is altered within an atomic scale [75] and only emission angle and energy are equal for all particles. The trajectory of each ion is recorded, so that for any collision with other atoms the conditions (with respect to energy and trajectory of the particle) are well defined. Each collision is assumed to change the ion's direction and energy. The mentioned slight modifications of the lateral starting position of each ion lead to random trajectories of successively simulated ions and, in combination with a large number of iterations, yield statistically significant information about the final energy, angular, and lateral distribution of initially "identical" particles after a given number of collisions.

SRIM is fast, precise and easy to use. However, the scope of SRIM is somehow limited due to the point-like and mono-energetic character of the software, preventing it from application close to reality. Therefore, SRIM can be combined with S^3M [76] or SIMTRA [58], with the former being a tool to exactly define arbitrary starting conditions for subsequent SRIM simulations and the latter being a tool to

model magnetron sputter chambers and related transport processes based on SRIM simulations. In detail, S^3M can be used to model an Ar plasma with a geometrical appearance close to the form of the real racetrack of a desired magnetron. Both energy and incidence angle of the Ar^+ ions can be exactly defined and saved in a TRIM.dat file, which in subsequent steps can be further modified with a suitable software (like Matlab) to control the geometrical appearance of the target. Moreover, it can also directly be used as input file for SRIM simulations. SRIM successively reads the data of every single defined ion from the TRIM.dat file and uses that information as starting condition for its MC-based code. The results of that simulations are by default saved in SRIM output files, in a structure related to the TRIM.dat file. S^3M can be used to create new TRIM.dat files from these output files. Doing so, successive SRIM simulations based on each other can be conducted, which tremendously increases the applicability of SRIM to problems close to reality.

In contrast to S^3M, SIMTRA does not generate data for SRIM, but solely can make use of data that was generated by SRIM. Thus, sputtering of various target materials can be simulated with SRIM and the resulting data used for simulation of transport from target to substrate with SIMTRA. SIMTRA allows to model any deposition chamber with exact dimensions and properties. Its library allows to add magnetrons, substrate carriers and both planary and rotatable targets to the model. Simulations focus on the transport characteristics from target to substrate and record all areas, where sputtered atoms are deposited. Thus, in principle also the path of thermalized particles could be investigated.

Chapter 5 was almost identically submitted by the author of this thesis for publication. In the current thesis, all superfluous equations were replaced with references to the main text. Moreover, the figure numbering was adapted to fit to the thesis.

5. The sputter performance of an industrial-scale planar Mo-target over its lifetime: target erosion and film properties

5.1 Introduction

Magnetron sputtering is widely used to deposit Mo thin films for display and microelectronic applications [14,49]. This method utilizes the kinetic energy of Ar^+ ions bombarding the surface of a target, where the ejected target atoms create a vapor phase and subsequently form a film with adjustable properties on a chosen substrate [9]. These Ar^+ ions are extracted from a magnetron-confined sputter plasma, consisting of Ar neutrals, Ar^+ ions and electrons. The magnetic field lines (B) of the permanent magnets located behind the target affect the movement of electrons. With an electric field E applied to the magnetron, the E×B drift leads to a circular or elliptical drift movement of the electrons over the target area. Where the E×B drift confines the electrons, an increased number of inelastic collisions of electrons with Ar results in an increased number of Ar^+ ions $N(Ar^+)$ [9] and the formation of an erosion groove on the target surface, limiting target utilization and lifetime [14]. Considerable efforts have been put into the optimization of the ratio of E and B and to correlate erosion groove depth with film properties [15–23]. Although being studied extensively on laboratory-scale and via computer simulations, only little is known on the effect of an erosion groove formed on an industrial-scale rectangular planar target on the properties of films deposited at different stages of target usage. Dewald *et al.* [77] correlated different race track depths of a ceramic $ZnO:Al_2O_3$ target with local variations of visual absorption and electrical resistivity of synthesized films. Kupfer *et al.* [78] used two magnetrons operated as dual magnetron to deposit indium tin oxide (ITO) films. Langmuir probe measurements allowed them to correlate changes of the ratio of charge carrier density (n_i) to deposition rate (R) with differences in film properties. These changes of n_i/R were attributed to the cross-magnetron effect [79]. Pflug *et al.* performed Monte Carlo simulations for an industrial-scale magnetron and found differences in plasma density at different positions over the target area [80]. However, only limited data is available about the influence of the change of the magnetic field strength with proceeding target erosion on film growth conditions [14]. To improve our present understanding of film growth with respect to erosion groove depth, the current thesis consists of two parts, (*i*) target

erosion in order to create an erosion groove of defined depth and (*ii*) thin film deposition at regular steps of the target erosion progress. This approach allows to correlate the progressing erosion of the target with possible changes in film microstructure and properties.

5.2 Experimental details

5.2.1 Target erosion

A new rectangular planar Mo-target (600 × 125 × 14 mm³, sintered and rolled, Plansee SE) was mounted in an industrial-scale in-line magnetron sputter facility (FHR Line.600V) and sputter eroded in non-reactive mode using an Ar plasma. In the used FHR SR600/125 magnetron, the outer magnets behind the target were arranged in the shape of a rectangle with rounded edges, with countermagnets in the center of the target. The sputter system consists of a load-lock and a process chamber. In order to minimize the contamination of the process chamber during target erosion with excessive coating material, the target was shielded with a custom-built austenitic stainless steel box, similar to the setup used in an earlier study [14]. For target erosion, the target was operated using a d.c. power supply (Advanced Energy Pinnacle 20 kW) at a constant power of 3.5 kW (power-controlled mode) for an overall duration of 85 h 42 min 51 sec, corresponding to a target utilization of 300 kWh, marking the end of the erosion process used for the present investigation. The target's geometry permits a maximum erosion depth of 10 mm. At the beginning of the erosion process and every other 50 kWh, the process chamber was vented and the austenitic stainless steel box removed. The geometrical shape of the erosion groove as well as its depth were evaluated using a custom-built aluminum measuring bridge with a depth gauge. The magnetic field strength was evaluated for the non-eroded new target using the aforementioned measuring bridge in combination with a Gauss meter (Lake Shore Cryotronics, Model 410). Two different probes were used to access the magnetic field parallel ($B_{\parallel}$) and perpendicular ($B_{\perp}$) to the target surface. For the evaluation of $B_{\parallel}$ at 0 and 180 ° the x-component, for the evaluation of $B_{\parallel}$ at 90 ° the y-component of the magnetic field was measured (for definition of x and y see Figure 9). For the evaluation of $B_{\perp}$, two measurements were conducted with the probe's x-y-orientation tilted by 90 °. During these measurements, both probes were in contact with the surface of the non-eroded target. The measurements were conducted as line scans with a lateral distance of 1 cm between the measurements. After characterization of the erosion groove and magnetic field, the process chamber was evacuated without the austenitic stainless steel box for 48 h. The base pressure p_B for the following film deposition runs was below 1×10^{-4} Pa. Before film deposition, the target was sputter cleaned for 15 min to remove oxides and contaminants from the surface and to yield constant deposition conditions.

5.2.2 THIN FILM DEPOSITION

For thin film deposition, two different substrate carrier oscillation modes were used: (*i*) No carrier oscillation, referred to as "static deposition" in further discussions (blue color code), with the center of the carrier positioned opposite the target center. (*ii*) Oscillation of the substrate carrier in x-direction (Figure 9), with the center of the substrate carrier moving ±280 mm off the target center with a velocity of 20 mm/s, referred to as "oscillated deposition" in further discussions and "osc" in the figures (orange color code). Table 1 gives an overview of static and oscillated depositions performed at different stages of target usage.

Table 1: Overview of static and oscillated deposition runs performed (marked with +) at different stages of target usage.

target usage [kWh]	static	oscillated (±280 mm)
0	+	-
50	-	+
100	+	+
150	+	+
200	+	+
250	+	+
300	+	+

Thin films were deposited in independent runs on a 9 × 5 matrix of (100) oriented Si substrates (21 × 7 mm², p-type, 325 µm thick, electrical resistivity 1,000 to 10,000 µΩcm, MicroChemicals) that were ultrasonically cleaned in ethanol for 10 min and dried with hot air prior deposition. All substrates were mounted at equidistant positions with Kapton tape on the 550 × 550 mm² substrate carrier, as schematically shown in Figure 9. The horizontal distance between all nine substrates in each row was 25 mm, the vertical distance between all five rows 110 mm. The central column E as well as the central row 3 were positioned exactly opposite the central vertical and horizontal target axis.

Figure 9: Schematic representation of (a) the front view of the lateral arrangement of the 9 × 5 matrix of (100) Si substrates of size 21 × 7 mm², shown enlarged for better visibility and (b) the top view of the deposition setup. The spacing of the substrates is described in the text. Thin films were deposited in static deposition mode (static) and oscillated deposition mode (osc). The white rounded rectangle within the dark gray target rectangle in (a) shows the erosion track of the eroded target at the end of usage, whereas the 550 ×550 mm² outer square in (a) represents the substrate carrier.

The base pressure p_B in the load-lock-chamber was ≤ 1×10^{-3} Pa for all depositions. Before each deposition, a radio frequency (r.f., Advanced Energy Cesar 1310) powered etching step at 13.56 MHz was carried out in the process chamber for surface cleaning and activation of the Si substrates. There, the power was held at constant 0.8 kW (power-controlled mode) and the Ar gas pressure p set to 0.32 Pa. The grounded substrate carrier oscillated 12 times in front of the r.f. source with a velocity of 20 mm/s. For all film deposition runs, a constant Ar pressure p of 0.53 Pa, corresponding to a gas flow of 300 sccm, at a constant d.c. power of 3.5 kW (power-controlled mode) was used. The deposition time was held constant at 5 min for both, the static and the oscillated deposition mode. For the latter, this deposition time corresponds to 10 oscillation cycles with a velocity of 20 mm/s. The target-substrate distance was 75 mm at the beginning of the test. No additional substrate heating was applied to the grounded substrate carrier. During deposition, all available target voltage (U), target current (I), pressure (p) and substrate carrier movement data were logged.

5.2.3 Thin film characterization

Film thickness was obtained using a white light optical profilometer (Veeco Wyko NT 1000) with Vison64 software package via automatic step measurement in batch mode. Scanning electron microscopy (SEM, Zeiss Evo 50) and focused ion beam milling (FIB, Zeiss Leo 1540XB) with stepwise reduced ion currents down to 100 pA allowed to access topography and cross-sections of the films. Energy-dispersive X-ray spectroscopy (EDX, Oxford Instruments INCA), using built-in sensitivity factors, was used to investigate the elemental composition of the films. The microstructure of the films was assessed using X-ray diffractometry (XRD, Bruker-AXS D8 Advance) in $\Theta/2\Theta$ geometry. The used device was equipped with a Cu-K_α X-ray source and parallel beam optics. In order to minimize peaks stemming from the (100) Si substrate, measurements were conducted in unlocked-coupled mode with the X-ray tube and detector tilted by 1 °. During measurements the samples were constantly rotated. The obtained Mo (110) peaks were fitted using a Pseudo-Voigt approach with linear background correction from 40 to 41 ° and the respective full widths at half maxima (FWHM) calculated. The macroscopic residual film stresses σ_y (for definition of y see Figure 9) were calculated using the wafer curvature method with a custom-built device with two parallel laser beams in combination with the modified Stoney equation [81,82]

$$\sigma_y = M_s \frac{t_s^2}{6t} \frac{1}{r} \qquad (6)$$

with M_s being the biaxial modulus of (100) Si (M_s=180 GPa [82]), t_s and t the thickness of the substrate (325 µm) and the films, and r the curvature of the substrate on the longer side. The calculated film stresses represent the sum of intrinsic film stresses and thermal stresses due to different thermal expansion coefficients of Mo and Si. A four point probe (Jandel RM2) was used to determine the electrical resistance R of the deposited thin films. The electrical resistivity ρ was then calculated according to

$$\rho = \frac{R \cdot t \cdot W}{L}, \qquad (7)$$

with W and L representing the width and length of the Si substrates [7]. For graphical representation, the measured erosion groove depth, thickness, stress, and electrical resistivity data was plotted using the *contourf* function of Matlab R2019a.

5.3 Results and discussion

5.3.1 Target erosion

5.3.1.1 Geometrical shape of the target erosion groove

Figure 10 shows the evolution of the erosion groove depth over target usage. The erosion rates for the point of deepest erosion remained constant at 1.3 ± 0.2 mm from 0 to 300 kWh per 50 kWh. A maximum erosion groove depth of 7.85 mm, as represented in Figure 10(d), marks the end of target usage at 300 kWh in the present investigation. With a usable target thickness of 10 mm, this corresponds to a usage of roughly 80 % of the maximum target erosion. When examining the shape of the erosion groove in Figure 10(d), it is evident that the depth of the erosion groove is not equal all around the target, but more pronounced at the upper right and the lower left corner. This inhomogeneous target erosion is commonly known as “cross-corner effect” [22,23] and can be correlated to differences in the magnetic field strength in the straightway and the turnaround regions of the target (for the definition of the straightway and turnaround region see Figure 9), stemming from the magnets located behind the target. Due to geometric reasons (because of size limitations within the magnetron with concomitant restrictions of the used countermagnet size and strength in the center of the magnetron), the magnetic field strength usually is smaller in the turnaround region compared to the straightway [23].

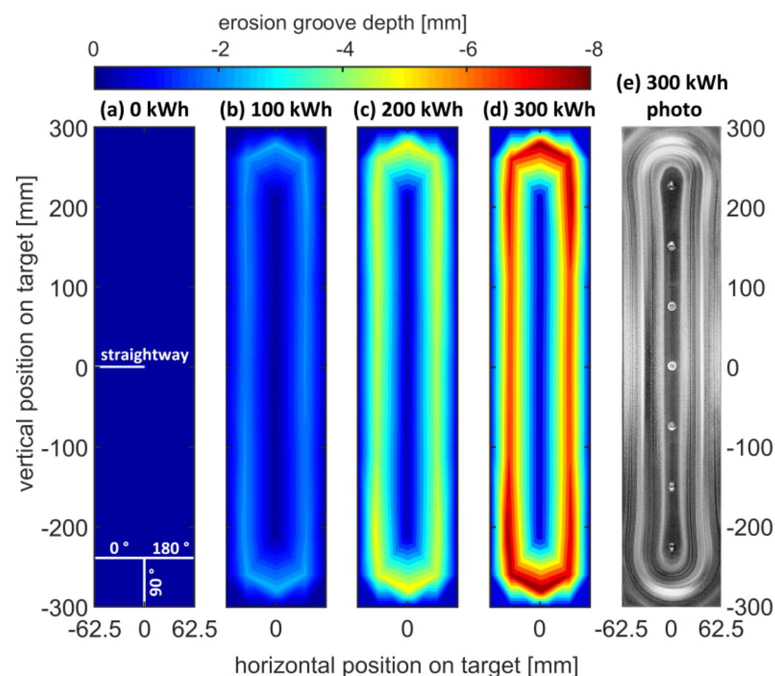

Figure 10: Evolution of the erosion groove depth over target usage, i.e. after (b) 100, (c) 200 and (d) 300 kWh. The schematics in (a) depicts the position of the magnetic field measurements, conducted on the new target (0 kWh). (e) shows a photograph of the fully eroded target after 300 kWh. Note that the shapes in the contour plot are a result of data interpolation due to a limited set of measurement points.

As shown by Shidoji *et al.* [22], differences in magnetic field strength lead to differences in the drift velocity of the electrons that are confined in front of the target, so that at every crossover from a weak to a strong magnetic field, the velocity of the electrons decreases. With this observable decrease in electron velocity, an increase in electron density is associated. Higher electron density leads to a greater number of inelastic collisions of electrons with Ar background atoms and a concomitant higher degree of ionization in the respective areas. More ions lead to a higher erosion rate of the target and hence explain the observed diagonally more pronounced erosion groove areas of the target (see Figure 10(d)). Shidoji *et al.* modeled the energetic electron impact ionization process to predict the erosion profile [22]. This infers that the macroscopic change of the target's erosion groove depth over the target area stems from differences in the plasma properties, with a greater number of Ar^{+} ions in the turnaround region compared to the straightway.

5.3.1.2 Magnetic field strength and its influence on particle energy

Figure 11(a-c) show the magnetic field strength parallel ($B_{\parallel}$, open symbols) and perpendicular ($B_{\perp}$, filled symbols) to the target surface, measured in the straightway (dashed lines) and turnaround region (solid lines, at angles of 0, 90 and 180 ° - see Figure 10(a)) of the target. Both, $B_{\parallel}$ and $B_{\perp}$, have higher magnitudes in the turnaround region compared to the straightway region, indicating that the magnetic field in the turnaround region is stronger than in the straightway region. This implies that the magnetic field strength of the magnetron used in the current thesis has a different setup compared to that studied by Fan *et al. [23]*, where the magnetic field was weaker in the turnaround region compared to the straightway region. In any case, the observed maximum erosion groove depth of 7.85 mm at 0 ° at the turnaround region, compared to an average depth of 6.0 mm in the straightway region (see Figure 10(a) and Figure 11 (d)), is in perfect agreement with the fundamental work of Shidoji *et al.* [22]. Inferred from that work, it can be expected that the highest target erosion is found in the crossover region from a weak to a strong magnetic field and not, as maybe expected intuitively, where the magnetic field strength is highest. If that was the case, the highest erosion should be found at 90 ° (see Figure 10(a), Figure 11 (b) and Figure 11 (e)). At 90 °, the erosion groove depth is only 7.6 mm compared to 7.85 mm at 0 °, followed by an erosion groove depth of 7.15 mm at 180 ° (Figure 11 (f)). This decrease of erosion groove depth with increasing angle indicates that the drift movement of the electrons is in clockwise direction and that it accelerates again at the exit of the turnaround region, as shown by Fan *et al. [23]*. The consequently higher electron velocity at the exit of the turnaround region leads to a decrease in electron density and hence less inelastic collisions of electrons with Ar background gas atoms. This infers a smaller number of Ar^{+} ions at 180 ° compared to 0 ° and therefore less erosion in this particular area.

Besides lateral differences in electron and Ar^+ density due to the cross-corner effect, the overall evolution of the erosion groove will also impact film growth conditions due to several reasons. These are (*i*) an increase in the target-substrate distance from 75 mm to 75+7.85=82.85 mm, corresponding to an increase of about 10 %. Since all other deposition parameters (power, pressure and deposition time) were held constant, the rising target-substrate distance will increase the number of collisions of sputtered atoms with Ar background gas atoms and decrease the deposition rate. (*ii*) The development of a slope on the edges of the erosion groove will affect the emission angle of the sputtered atoms [55]. This slope will also change the angle of reflected Ar neutrals. These neutrals stem from elastically reflected and neutralized Ar^+ ions, which consequently maintain considerable energies up to the initial acceleration energy [83]. According to Drüsedau et al. [57], this high energy of the reflected Ar neutrals contributes up to 50 % of the total energy per incorporated atom for the growth of Mo thin films. The total energy per incorporated atom $\langle E_t \rangle$ – defining the growth conditions of the respective film – is defined after Thornton [16] and Drüsedau [57] as

$$\langle E_t \rangle = U_0 + \langle E_{at} \rangle + E_0 \frac{R_E}{\gamma} + \langle E_P \rangle, \qquad (8)$$

with the heat of condensation (U_0), the average energy per sputtered atom ($\langle E_{at} \rangle$), the contribution of reflected neutrals ($E_0 \frac{R_E}{\gamma}$, with E_0 being the initial energy of Ar^+, given by the applied voltage on the target, R_E being the energy reflection coefficient [57,84] and γ the sputter yield) and plasma radiation ($\langle E_P \rangle$). Since the individual energy contributions to $\langle E_t \rangle$ should change over the course of target erosion, it is expected that film growth conditions should change simultaneously. (*iii*) Over target usage, the eroded target surface will get closer to the magnetron beneath. Therefore, the confinement of electrons close to the target surface will become more pronounced, leading to an increased number of charged particles in front of the target. In the power-controlled sputter mode, this effect has been reported by Hofer-Roblyek *et al.* [14] as an increase in current accompanied by a decrease in voltage, when eroding a new rotatable Mo target until the end of its lifetime. As shown by Andritschky *et al.* [85], the sputter current is proportional to the number of Ar neutrals $N(Ar^0)$ reflected from the target. Therefore, an increase in sputter current over target usage will also increase the number of reflected Ar neutrals impinging on the substrate. This increase in number of Ar neutrals over target usage will counteract the decrease of $\langle E_t \rangle$, stemming from a wider angular emission of Ar neutrals due to the increasing slope on the edges of the erosion groove – and increase $\langle E_t \rangle$ again.

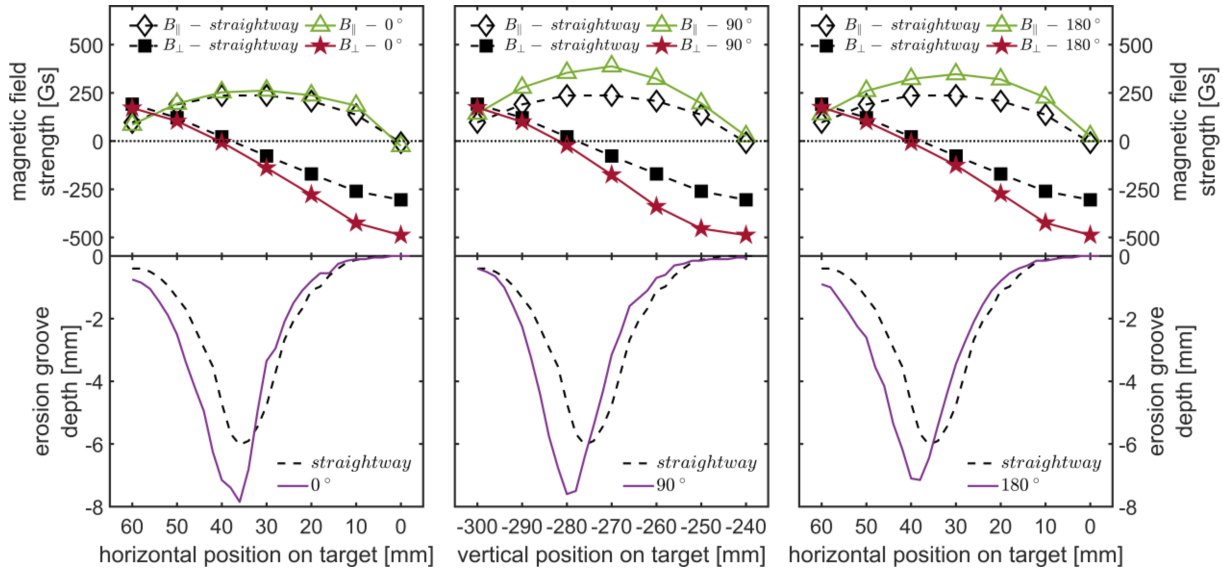

Figure 11: Correlation of magnetic field strength and erosion groove depth. All values are plotted from the edge towards the center of the target. (a-c) show the evolution of the magnetic field strength parallel ($B_\parallel$, open symbols) and perpendicular ($B_\perp$, filled symbols) to the target surface, measured in the straightway (dashed lines) and turnaround region (solid lines), whereas (d-f) compare the evolution of the erosion groove depth in the straightway (dashed lines) to the turnaround (solid lines) region (see Figure 10(a) for angle descriptions). Note that for (a, c, d, f) y = 0, whereas for (b, e) x = 0.

5.3.1.3 Voltage and current evolution

Figure 12 shows the evolution of voltage and current at constant discharge power obtained for static and oscillated film depositions for increasing target usage. The plotted values represent the average voltage and current for each deposition run. The measured Ar gas pressure p for a constant gas flow of 300 sccm remained constant for all depositions at 0.53 Pa. For both deposition modes, static (Figure 12(a)) and oscillated deposition (Figure 12(b)), the current rises over target usage. For static depositions, an increase from $I = 8.33 \pm 0.07$ to 10.0 ± 0.35 A was observed for depositions performed at the beginning (0 kWh) and end of target usage (300 kWh), respectively. For oscillated depositions, the current rises from $I = 8.47 \pm 0.33$ (0 kWh) to 9.70 ± 0.30 A (300 kWh). Since the target thickness in the erosion groove decreases with ongoing target erosion, both the magnetic field strength and the current increase [14]. Since the power during deposition was kept constant, the voltage follows an opposite trend, namely a drop of voltage over target usage from $U = 420 \pm 1$ to 349 ± 4 V for static depositions performed at the beginning (0 kWh) and end of target usage (300 kWh). For oscillated depositions, the voltage drops from $U = 412 \pm 1$ (0 kWh) to 360 ± 7 V (300 kWh).

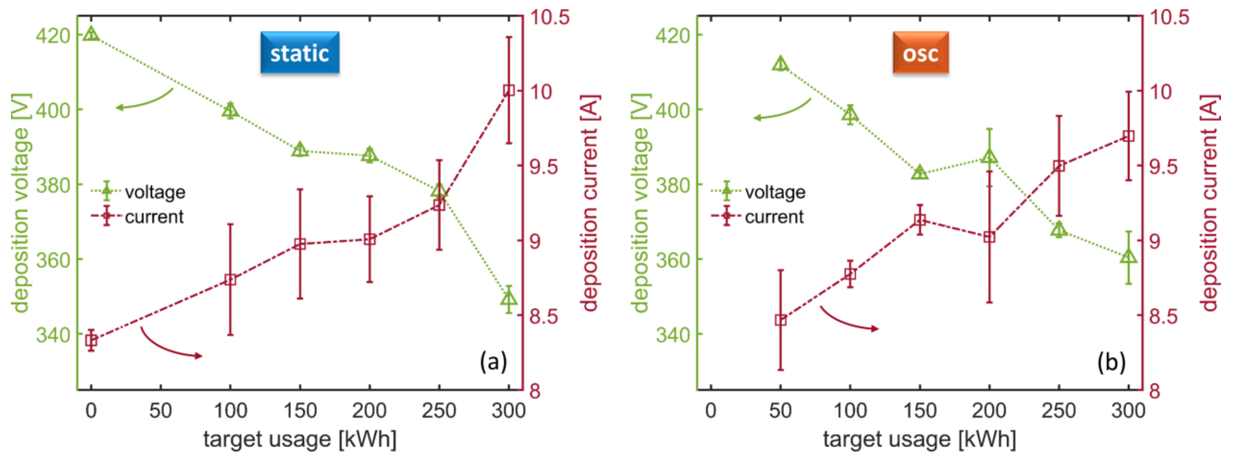

Figure 12: Voltage and current of (a) static and (b) oscillated thin film depositions done at different stages of target usage.

5.3.2 Thin film characterization

5.3.2.1 Film thickness

Thin films were synthesized on a 9 × 5 matrix of (100) Si substrates and characterized by several techniques. For films deposited outside the central target area, i.e. in rows A, B and H, I, a drastic drop in film thickness was observed. Since film deposition is usually done opposite the target, all further reported film characteristics focus on rows C to G that were positioned opposite the central target area.

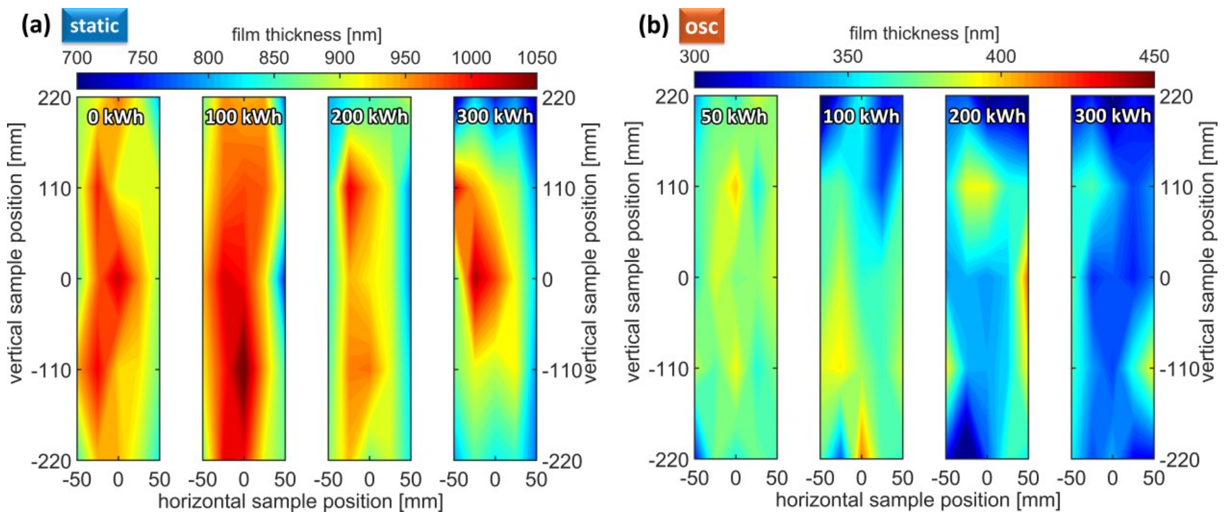

Figure 13: Evolution of the film thickness of films synthesized in (a) static and (b) oscillated deposition mode over target usage. Note the different z-scale of the film thickness color bar. The horizontal and vertical sample positions refer to the center of the 9 × 5 substrate matrix shown in Figure 9. A sample position of (0/0) hence refers to the target center and sample 3E. Note that diamond-like shapes in the contour plot stem from local maxima of the film thickness on a certain sample; they are therefore a result of data interpolation.

As visible in Figure 13(a), the film thickness homogeneity deteriorates over the course of target erosion. It is apparent that the film thickness decreases especially close to the turnaround compared to the straightway region. When considering the form of the plasma lobes over the target, one can expect the highest deposition rate in the straightway of the target (with two plasma lobes close to each other). The circular form of the plasma lobes in the turnaround region should yield much smaller deposition rates compared to the straightway. However, the cross-corner effect (see section 5.3.1.2) counterbalances this geometrical appearance of the plasma lobes and increases the deposition rate in the turnaround region and close to it. This explains the high degree of film thickness homogeneity for films deposited with a new target (Figure 13(a), 0 kWh). Over target usage the geometrical appearance of the target changes with the evolution of the erosion groove, which changes the emission profile of the sputtered Mo atoms from a heart shaped towards a cosine-like distribution [55]. For the straightway region, this should not have a large influence due to superposition of the emission profiles of the left and right plasma lobe. For samples positioned close to the turnaround region (see Figure 9), this change in emission profile will decrease the deposition rate, since the plasma lobes are not parallel to each other. Figure 13(b) shows the lateral distribution of film thickness for films deposited in oscillated mode. Note that due to the smaller film thickness, the z-scaling of the color bar is different than in Figure 13(a). It is evident that the film thickness distribution is, as expected, much more homogeneous compared to the static deposition mode. Nevertheless, the film thickness varies with target usage and lateral position of the sample on the substrate carrier.

5.3.2.2 Film morphology

Figure 14 shows surface topographies and cross-sectional morphologies of thin films deposited in static deposition mode with a new target (0 kWh, left column) and at the end of its usage (300 kWh, right column), recorded with SEM and FIB techniques. The upper row displays samples deposited in the straightway region, at position 3E, whereas the lower row samples were grown close to the turnaround region, at position 5E (see Figure 9). These micrographs infer that neither target age nor deposition position greatly influence surface topography and cross-sectional morphology of the films. In all cases, the films consist of dense columnar structures with fish scale-like surface features. These structures usually develop due to competitive growth of grains with different initial orientations [8,86,87].

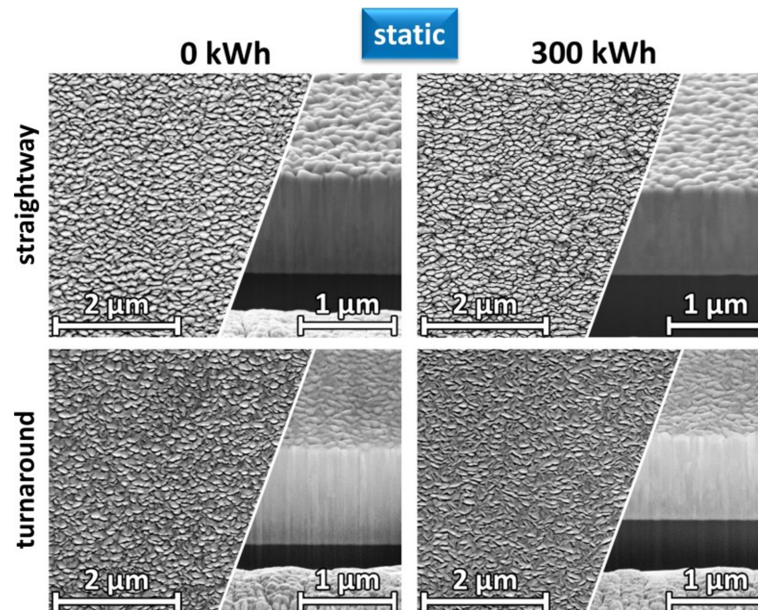

Figure 14: SEM images of the surface (left side) and FIB cross-sections (right side) of films grown in static deposition mode in the straightway (corresponding to sample 3E, upper row) and close to the turnaround region (corresponding to sample 5E, lower row), deposited with a new target (0 kWh, left column) and at the end of the target's usage (300 kWh, right column).

Similar conclusions can be drawn for films synthesized in oscillated deposition mode (see Figure 15), although slight differences are visible compared to the static deposition mode. It is worth noting that the films grown in oscillated deposition mode are thinner and therefore in an earlier stage of film growth than films grown in static deposition mode, which will also affect the visible grain size on the film surface [88]. However, it is evident that the movement of the carrier influences both the grain size as well as the morphology, so that the grains become smaller and the porosity of the film slightly increases. These findings are in good agreement with our earlier study [14] where the deposition behavior of an industrial-scale rotatable Mo-target over its lifetime was studied using the same deposition system. There, the decrease in grain size and increase in film porosity from static to oscillated depositions was ascribed to differences in growth conditions opposite and at extended distances from the target. In another work [49], we found a strong correlation between surface structure and morphology of films and the energy of the arriving particles with respect to the distance from the target center, being in good agreement with Anders' SZM [65], with higher energies leading to denser structures. At extended distances from the target center we could show that a higher fraction of thermalized particles lead to more porous morphologies. A decreased adatom mobility due to lower substrate carrier temperature, stemming from the less-intense particle bombardment compared to the target center as well as shading effects, enforces this effect. As reported in our previous work, the temperature opposite the target was determined to reach up to 500 K for

deposition times > 5 min [7,89], whereas at extended distances from the target center a temperature of 300 K can be assumed [49]. This means that at extended distances from the target center, or at the vertex of the oscillation movement, low energy growth conditions are predominant, leading to the observed more open voided structures. Although EDX analysis showed no contamination of the grown Mo films with Ar or O_2 that could have been incorporated at the vertex of the oscillation movement during growth, we are well aware that the extended exposure time to residual gas for oscillated depositions will influence growth conditions and contribute to the observed smaller grain size. This could negatively affect film properties such as stress or electrical resistivity.

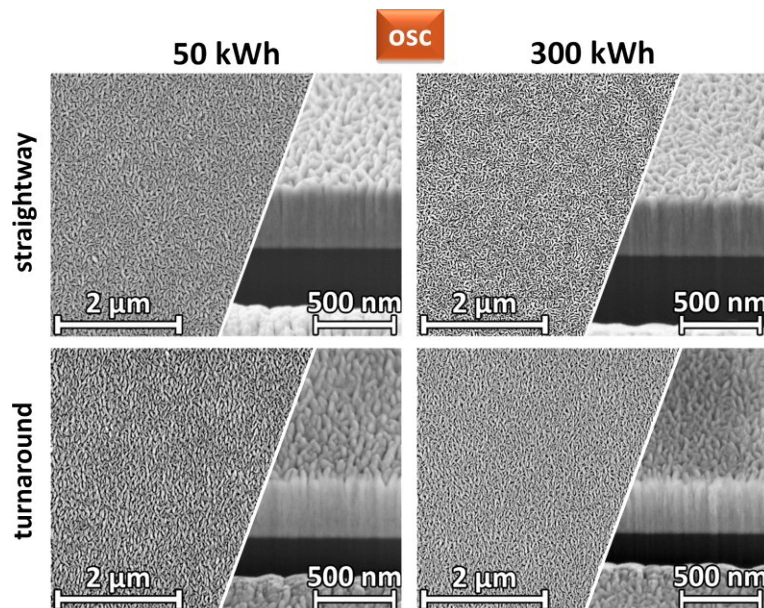

Figure 15: SEM images of the surface (left side) and FIB cross-sections (right side) of films grown in oscillated deposition mode in the straightway (corresponding to sample 3E, upper row) and close to the turnaround region (corresponding to sample 5E, lower row), deposited with an almost new target (50 kWh, left column) and at the end of the target's usage (300 kWh, right column).

5.3.2.3 Microstructure

The findings obtained by SEM in section 5.3.2.2 are corroborated by XRD, as evidenced by Figure 16 and Figure 17. All films are characterized by the single-phase body-centered cubic (bcc) Mo structure [90]. Due to the strong preferential (110) orientation of the films, the presented diffractograms solely focus on this peak. Comparison of the peaks obtained for static and oscillated depositions show that the substrate carrier movement not only affects the surface and film morphology (Figure 14 and Figure 15), but also the resulting microstructure. Moreover, a change of the microstructure over target usage and the respective position on the substrate carrier is evident.

For static depositions with a new target (Figure 16, 0 kWh), no distinct differences in microstructure are visible for films deposited at different positions opposite to the straightway region. Close to the turnaround region, the peak intensity for the film deposited opposite the cross-corner area (samples 5C and 5E, denoted as 0 ° in Figure 10) more than doubles compared to the film deposited opposite the less eroded target area (5G, denoted as 180 ° in Figure 10), meaning that the degree of crystallinity is higher for samples 5C and 5E than for sample 5G. This is in good agreement with the conclusion of a higher number of Ar^+ ions in the cross-corner region at 0 ° compared to 180 ° (Figure 10) as discussed in section 5.3.1.2. In general, a higher ion to metal atom ratio $\phi = J_i/J_{Me}$ will improve growth conditions and lead to denser films with a higher degree of crystallinity [91,92]. Since for the studied conditions $J_{Me} \gg J_i$, this effect will only contribute slightly to the increased crystallinity of sample 5C compared to 5G. But, as stated in section 5.3.1.2, an increase of $N(Ar^+)$ will also increase $N(Ar^0)$ and therefore increase $\langle E_t \rangle$ – leading to more crystalline films. With the evolution of the erosion groove, this difference for samples deposited close to the turnaround region (5C, 5E and 5G) vanishes and their peak intensities level towards a constant value for all sample positions. This is probably because of averaging effects due to the formation of a slope at the edges of the erosion groove. Besides these observable differences in peak intensity of samples 5C, 5E and 5G, all peak intensities for samples deposited close to the turnaround region decrease over target usage. The distribution of film thickness with respect to target usage summarized in Figure 13(a) already revealed that the film thickness close to the turnaround region decreases over time. Since the thinner film samples are in an earlier stage of film growth [88], smaller peak intensities are obtained. This effect was also described by Hofer *et al.* for Mo films with varying thicknesses [93].

Due to the observed difference in film thickness between the straightway and turnaround region (see Figure 13(a)), peak intensities for films grown in both regions are not directly comparable. In any case it is evident for samples deposited in the straightway that the respective peak intensities of samples positioned opposite the plasma lobes from columns C and G in the straightway (see Figure 9) decrease from 0 to 150 kWh target usage, in order to slightly increase again from 150 to 300 kWh. Only the diffraction intensities obtained for the samples of the central column E decrease over the entire target usage. Two concurring effects can explain these observations, namely an increase of the number of charged particles over target usage (due to the increase in current evident from Figure 12(a)) and the evolution of the erosion groove. The higher number of charged particles will increase the overall number of reflected Ar neutrals, leading to a higher energy per incorporated atom $\langle E_t \rangle$, which improves the film quality with respect to increased grain size and lower electrical resistivity [91,92]. On the contrary, the evolution of the erosion groove will decrease the energy per incorporated atom

$\langle E_t \rangle$ due to a wider angular distribution of reflected Ar atoms as well as sputtered Mo atoms because of the progressing evolution of the slope of the edges of the erosion groove, as proposed in section 5.3.1.2. The combination of these two phenomena could lead to the observed differences in crystallinity for samples deposited in the straightway region at different positions and stages of target usage.

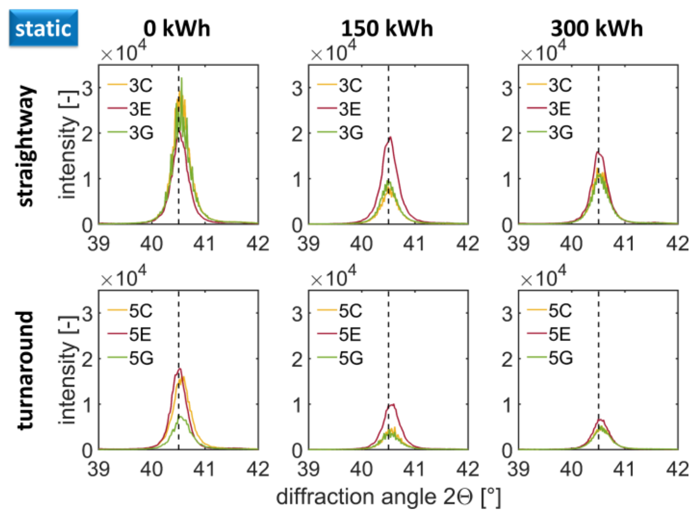

Figure 16: Absolute intensity X-ray diffractograms obtained for the (110) peak of Mo films deposited in static deposition mode on (110) Si at different substrate carrier positions (straightway and turnaround, in the center (samples 3E, 5E – see Figure 9) and exactly opposite the plasma lobes (3C, 3G, 5C, 5G – see Figure 9)) at different stages of target usage.

In comparison to the static deposition mode, all films deposited via oscillated deposition mode exhibit smaller X-ray diffraction intensities (Figure 17) that can be attributed to the smaller average thickness for films deposited via oscillated deposition mode compared to the static deposition mode (356 ± 12 nm vs. 898 ± 27 nm average film thickness for all films deposited in the respective deposition modes in columns C to G). Of course, the intention of the carrier movement from one side of the target to the other is to yield homogeneous films over the whole area of the substrate carrier. As visible in Figure 17, a high degree of homogeneity can be reached. However, especially the samples of the central column E show different microstructures compared to samples of column C and G, both in the straightway as well as close to the turnaround region. For oscillated depositions with an almost new target (Figure 17, 50 kWh), films synthesized on either position in the straightway region are characterized by very similar microstructures. This changes after a target usage of 150 kWh, with the central sample 3E having the highest diffraction intensity, indicating the highest degree of crystallinity. At the end of the target's usage after 300 kWh, all samples show identical microstructures again. Close to the turnaround region, the central sample 5E has always the highest diffraction intensity, although its intensity decreases, being least pronounced after 300 kWh of target usage. These changes in

crystallinity for the central column E compared to columns C and G could be explained by the different distance the substrates are located off the target center during deposition. For column E, the maximum distance is 280 mm, for columns C and G the maximum distance is 330 mm. The enlargement of the distance by 50 mm for columns C and G can contribute substantially to differences in growth conditions due to an increased number of collisions of energetic particles with background atoms on their way to the substrates [49]. The mean free path (λ, [35]), defined in section 2.2, allows to calculate the average distance an atom can travel through the gas phase without collision. For a deposition pressure p of 0.53 Pa and an assumed temperature T of 300 K [7,49], the mean free path of sputtered Mo atoms is 41.4 mm. For (reflected) Ar atoms λ = 87.2 mm. This means that with an increase of 50 mm from target to substrate, sputtered Mo atoms on average exhibit one more collision with background Ar gas atoms when travelling to columns C or G compared to column E. This collision reduces the energy of the particles, so that they reach the surface of the growing film with lower energy. Low energetic adatoms will result in the formation of additional nuclei on the surface of the growing films instead of moving to already existing grains, thus, decreasing the overall crystallinity of the films grown in columns C and G. The difference in crystallinity obtained for films grown in columns E and C/G decreases over target usage. This could be attributed to the evolution of the erosion groove, changing the initial emission angle of sputtered and reflected atoms and subsequent averaging effects.

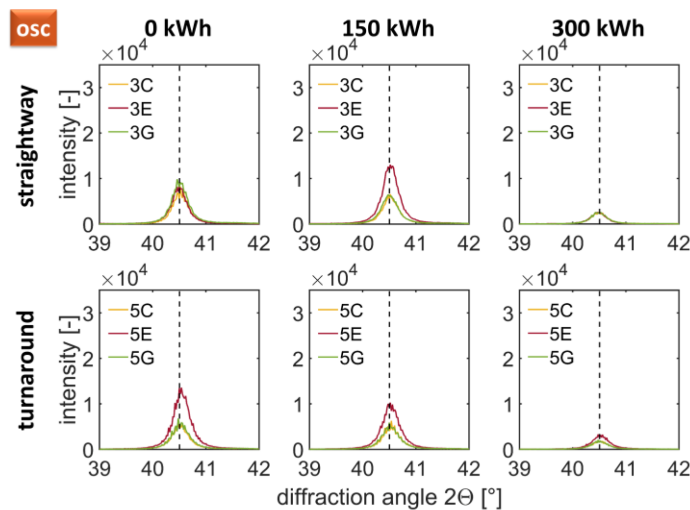

Figure 17: Absolute intensity X-ray diffractograms of the (110) peak of Mo films deposited in oscillated mode on (110) Si at different substrate carrier positions (straightway and turnaround, in the center (samples 3E, 5E – see Figure 9) and exactly opposite the plasma lobes (3C, 3G, 5C, 5G – see Figure 9)) at different stages of target usage. Note that all samples 3C, 3E and 3G show similar X-ray reflections after 300 kWh.

In order to qualitatively assess the average coherently diffracting domain sizes of films deposited in static deposition mode at different positions on the substrate carrier over target usage, the full widths at half maximum (FWHM) of the Mo (110) peak were calculated (see Figure 18). Despite the relatively

small changes of the FWHM of the Mo (110) peak over target usage, the similar trends observed for all samples suggest a statistically relevant underlying mechanism. For all sample positions investigated, the FWHM are similar in the beginning of the target usage, with a distinct trend towards higher values at 150 kWh. This indicates a slight decrease in average domain size from 0 to 150 kWh, in order to increase again after a target usage of 200 kWh, being in good agreement with the proposed change of energy per incorporated atom $\langle E_t \rangle$ due to the evolution of an erosion groove (section 5.3.1.2). A drop of $\langle E_t \rangle$ leads to a deterioration of film growth conditions, leading to the formation of smaller domains. On the other hand, with ongoing target usage an increased number of charged particles – directly increasing the number of reflected Ar neutrals [85] and therefore increasing $\langle E_t \rangle$ – counterbalances the worsening in growth conditions. As evident from Figure 12(a), a pronounced increase in current was observed for depositions done after 200 kWh, leading to an enhanced density of charged particles and reflected Ar neutrals, consequently improving film growth conditions and leading to formation of larger domains.

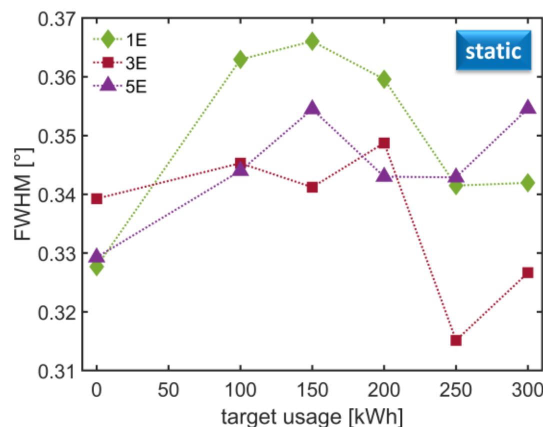

Figure 18: Full width at half maxima (FWHM) of the Mo (110) X-ray diffraction peak for films deposited via static mode. The lines connecting the data points have no mathematical meaning but are solely drawn to guide the eye.

5.3.2.4 Film stress

Film stresses σ_y were measured and found to be tensile (Figure 19). Films grown in static mode using the new target (0 kWh) are characterized by an average tensile stress of 726 ± 116 MPa, at the end of the target's usage (300 kWh) the average tensile stress is 795 ± 82 MPa. The reported stress values are in good agreement with the fundamental work of Hoffman [94], who found tensile stresses up to 1 GPa in Mo films deposited from a planar magnetron source at similar Ar pressures as in the current thesis. With target usage from 0 to 100 kWh, this average tensile stress drops to 525 ± 106 MPa. As already discussed in section 5.3.2.3, the rise of the FWHM of the Mo (110) X-ray diffraction peak indicates a reduction of the average domain size in that regime. This decrease in domain size is attributed to a

decrease of the energy per incorporated atom $\langle E_t \rangle$. The observed decrease of the FWHM after 200 kWh indicates that $\langle E_t \rangle$ rises again after that amount of target usage.

In general, after Müller *et al.* and Vink *et al.*, two competing effects lead to tensile stresses, namely (*i*) stress buildup due to intracolumnar voids and (*ii*) stress relaxation due to lost intercolumnar coupling because of an increased porosity at column boundaries [95,96]. Müller [96] has conducted molecular dynamics simulations of the growth of Ni thin films and found a direct correlation between $\langle E_t \rangle$ and the void size distribution between adjacent grains, which represents the porosity of a nanocolumnar atomic network. Vink *et al.* [95] studied the relationship between film stresses and nanostructure of magnetron sputter deposited Mo thin films by transmission electron microscopy and correlated nanoporosity and respective stresses of the films with the working gas pressure, which directly influences $\langle E_t \rangle$. At low $\langle E_t \rangle$, films are characterized by large nanopores with scarcely any interaction between adjacent domains. This results in low tensile stress. With increasing $\langle E_t \rangle$ the size of these pores shrinks and an increase of film density is observed, leading to an increased intercolumnar coupling and therefore higher tensile stresses.

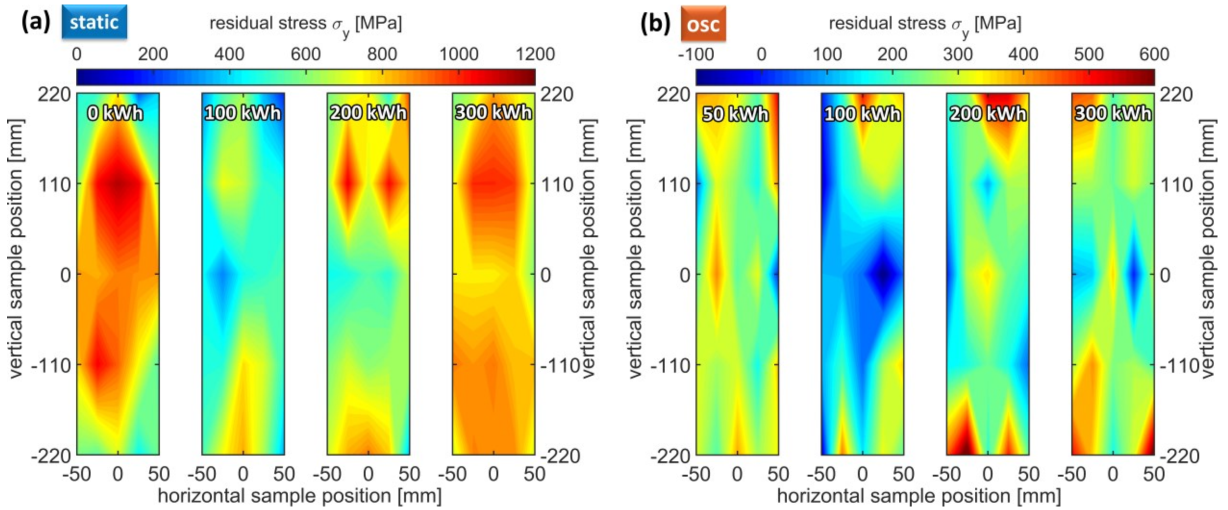

Figure 19: Overview of the stress distribution for samples synthesized in (a) static and (b) oscillated deposition mode for selected target usage. Note the different z-scale of the residual stress color bar. The horizontal and vertical sample positions refer to the center of the 9 × 5 substrate matrix shown in Figure 9. A sample position of (0/0) hence refers to the target center and sample 3E. Note that diamond-like shapes in the contour plot stem from local maxima of the residual stress on a certain sample; they are therefore a result of data interpolation.

Therefore, the expected differences in $\langle E_t \rangle$ over target usage could not only lead to differences in domain size, but also change the porosity of the nanocolumnar atomic network. These considerations explain the observed trends in film stress distribution, as shown in Figure 19(a). Reflected Ar neutrals lead to high energetic growth conditions and to larger domains in the beginning of the target usage. These domains experience high tensile stress due to strong intercolumnar coupling and a high number

of intracolumnar voids (Figure 19(a), 0 kWh). With the evolution of the erosion groove, the emission angle of these reflected Ar neutrals changes. The distribution of reflected Ar atoms becomes much wider and the film growth conditions become less energetic, as discussed in section 5.3.1.2. Less energetic growth conditions lead to smaller average domain sizes (see Figure 18) and more shadowing effects, so that the individual domains are slightly separated from each other. This leads to a decrease in intercolumnar coupling and a concomitant decrease of tensile stress (Figure 19(a), 100 and 200 kWh). With an increase in current over target usage (see Figure 12(a)), the available higher fraction of charged particles increases the number of reflected Ar neutrals and therefore $\langle E_t \rangle$. With increasing $\langle E_t \rangle$, the growth conditions improve, leading to larger domains and denser structures. Therefore, the tensile stresses increase again to the observed values (Figure 19(a), 300 kWh). These observations are also valid for films grown in oscillated deposition mode (Figure 19(b)). The overall film stress homogeneity for films deposited in oscillated deposition mode is higher than for films deposited in static mode. Nevertheless, similar trends are visible for films grown in oscillated deposition mode compared to static mode: High energetic growth conditions in the beginning of the target usage lead to tensile stress due to intercolumnar coupling and a high number of intracolumnar voids (Figure 19(b), 0 kWh). With increasing target usage, the stress decreases (Figure 19(b), 100 kWh), in order to slightly increase again towards the end of target usage (Figure 19(b), 300 kWh).

5.3.2.5 Electrical resistivity

Figure 20 displays the lateral distribution of the electrical resistivity of films deposited at different positions opposite the target after 0, 100, 200 and 300 kWh, both in static (a) and oscillated (b) deposition mode. Since the electrical resistivity of the Si substrates is much larger than the film resistivities, the shown values closely represent the actual film resistivities. Two phenomena are evident, namely a change of electrical resistivity for films deposited (*i*) at different stages of target usage and (*ii*) at different lateral positions opposite the target. For films deposited in the static deposition mode (Figure 20(a)), the former effect can be attributed to changes in the energy per incorporated atom $\langle E_t \rangle$ due to the evolution of an erosion groove, as discussed before. This change in $\langle E_t \rangle$ over target usage leads to large domains in the beginning of the target usage (Figure 20(a), 0 kWh) with a low fraction of grain boundaries and therefore low electrical resistivities [97]. With a decrease of $\langle E_t \rangle$ from 0 to 100 kWh, the domains become smaller and the fraction of grain boundaries increases. A higher fraction of grain boundaries leads to increased electron scattering and increases the electrical resistivity [97]. With ongoing target erosion, the increased number of charged particles increases the number of reflected Ar neutrals and therefore $\langle E_t \rangle$. This leads to larger domains [91,92] and to smaller electrical resistivities in the end of the target's usage (Figure 20(a), 300 kWh). For films deposited in

the oscillated deposition mode (Figure 20(b)), the resistivity of all films is much higher than of films grown via static deposition mode (note the different z-scaling of the color bar in Figure 20(a) compared to Figure 20(b)). Moreover, an increase of electrical resistivity throughout the whole target usage is observable (Figure 20(b)). This can be attributed to an extended residence time of the substrate carrier in the low flux area at extended distances from the target center. That decreases the energy input into the growing film as well as the substrate carrier temperature and increases the exposure time of the film surface to residual gas. These factors deteriorate film growth conditions [49]. It seems that these effects are predominant compared to the proposed increase of $\langle E_t \rangle$ towards the end of the target's usage (Figure 20(b), 300 kWh), so that an increase in $\langle E_t \rangle$ cannot counterbalance the low adatom mobility and low substrate temperature at extended distances off the target center as well as the influence of residual gas on film growth conditions.

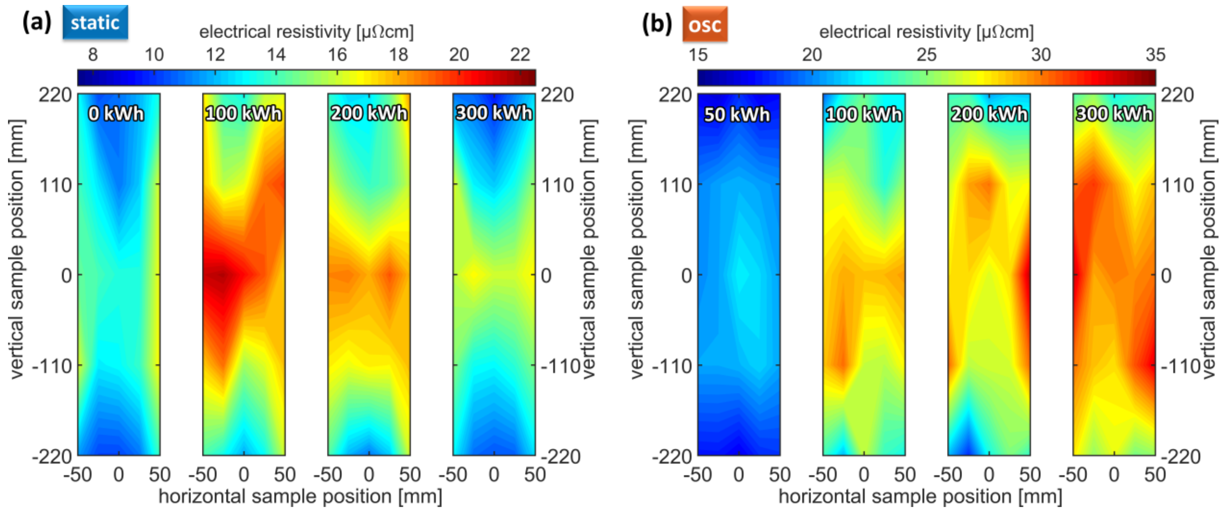

Figure 20: Overview of the electrical resistivity distribution for samples synthesized in (a) static and (b) oscillated deposition mode for selected target usages. Note the different z-scale of the electrical resistivity color bar. The horizontal and vertical sample positions refer to the center of the 9 × 5 substrate matrix shown in Figure 9. A sample position of (0/0) hence refers to the target center and sample 3E. Note that diamond-like shapes in the contour plot stem from local maxima of the electrical resistivity on a certain sample; they are therefore a result of data interpolation.

The latter of the two phenomena mentioned above, namely the lateral differences in electrical resistivity (see Figure 20), can be related to the cross-corner effect. This cross-corner effect leads to an increased ion to metal atom ratio ϕ due to an increased number of Ar^+ ions and therefore an increased number of reflected Ar neutrals close to the turnaround region compared to the straightway region, as discussed in section 5.3.1.2. The increase of $N(Ar^0)$ increases $\langle E_t \rangle$ and improves the film growth conditions, leading to denser films with larger domains [91,92]. Therefore, the electrical resistivity

close to the turnaround region is smaller compared to the straightway region, for films deposited in both static and oscillated deposition mode (Figure 20).

5.4 Conclusions

A new rectangular planar Mo target with the dimensions 600 × 125 mm² was sputter eroded to 80 % of its possible usage, marked by a maximum erosion groove depth of 7.85 mm. The erosion groove depth distribution was not equal, but more pronounced in the upper right and lower left corner. This inhomogeneous target erosion is attributed to the cross-corner effect, which describes a more pronounced erosion of sputter targets at the crossover from a strong to a weak magnetic field. In the crossover region, a higher number of electrons as well as Ar^+ ions are present. The lateral differences of Ar^+ ion density, with more Ar^+ ions in the turnaround region, lead to observable differences in film properties between the straightway and turnaround region of the target. We correlate this observation with a higher fraction of reflected Ar neutrals in this target region that locally increase the total energy per incorporated atom and therefore activate film growth. This results in films with lower electrical resistivity deposited close to the turnaround region compared to films with higher electrical resistivity deposited in the straightway region. Besides lateral differences, the degree of target usage also affects film properties. High intensity growth conditions in the beginning of target usage can be ascribed to a high number of reflected Ar neutrals that interact only with a small area of the substrate carrier. It is proposed that the evolution of the erosion groove widens the emission angle of Ar neutrals, so that the energy input into the growing films becomes distributed over a larger area and the total energy per incorporated atom decreases. Hence, the growth conditions change. With ongoing target erosion, the surface of the target gets closer to the permanent magnets behind the target, leading to an increased number of charged particles. This positively affects the ion to metal atom ratio as well as the number of reflected Ar neutrals, leading to an increase of the total energy per incorporated atom. Thus, film growth conditions towards the end of the maximum target usage improve again. A further detailed characterization of the plasma conditions in the used industrial-scale deposition system would be necessary to corroborate this hypothesis. In order to achieve homogeneous film growth conditions with a planar industrial-scale target, a constant magnetic field strength both over target surface (to minimize the implications of the cross-corner effect) and target usage (to minimize the effects of the erosion groove) would be required.

Chapter 6 was almost identically published by the author of this thesis before in [49]. In the current thesis, all superfluous equations were replaced with references to the main text. Moreover, the figure numbering was adapted to fit to the thesis.

6. SPUTTER DEPOSITION OF MO-BASED MULTICOMPONENT THIN FILMS FROM ROTATABLE TARGETS: EXPERIMENT AND SIMULATION

6.1 INTRODUCTION

Over the last decades, sputter deposited Mo thin films have been widely used in different fields of display and microelectronic applications, including source/drain electrodes, gate material or metallization layers for signal and data bus lines. Their good adhesion combined with a thermal expansion coefficient similar to glass make Mo thin films essential for these applications. Besides these advantages with respect to other materials, new challenges emerge due to the continuous increase of complexity of modern devices. Necessary heat treatments during their manufacturing can, for instance, lead to undesired discoloration of Mo due to surface oxidation, increasing the contact resistivity to adjacent (semiconducting) thin films and limit the accuracy of automatized quality control instruments. As shown by Jörg et al., the alloying of Mo with 20 at.% Al and 10 at.% Ti using co-sputtering from elemental targets can limit the oxidation of Mo without significantly changing other properties like resistivity and wet etching behavior [98]. When applying this new multicomponent MoAlTi system to rotatable sputter targets for the production of large scale flat panel displays, detailed knowledge about processing characteristics is required. In particular, the combination of elements with considerable differences in atomic mass within a multicomponent sputter target can lead to strong deviations of the thin film composition with respect to the target composition. Within the last decades, different coating systems sputtered from the corresponding multicomponent targets have been investigated thoroughly, such as SiC [44], TiB [31,35,99], Ti_2AlC [33], TiSi [28], Ti_3SiC_2 [34,46], TiW [29,39–43,45,100], VC [47], CrAlC [37], NbC [32], MoAl [48], MoSi [28,30], WB [101], and WSi [28]. For the system MoAlTi, the differences in atomic masses are obvious (m_{Mo} = 95.95 u, m_{Al} = 26.98 u, m_{Ti} = 47.87 u). Consequently, for large area depositions, this leads to the assumption that thin films deposited from MoAlTi multicomponent targets could yield different chemical compositions and thus properties depending on their lateral position with respect to the target. While all above mentioned coating systems were investigated using planar sputter targets, little is known about the sputter behavior of rotatable multicomponent targets. Depla et al. investigated the sputter behavior of single-element rotatable Y and Al targets in reactive mode on the laboratory scale and supported their

experiments with simulations using SIMTRA [102,103]. Pronounced differences in the sputter behavior of these targets depending on their rotation speed, due to differences in residence time of metallic and poisoned target areas within the plasma lobes, could be experimentally determined. Eisenmenger-Sittner et al. investigated *in situ* the surface roughness evolution of rotatable Al, Cu and Ti targets in reactive mode on the laboratory scale based on the reflectance pattern of a laser beam and correlated their findings to the degree of poisoning of the target surface [104,105].

The current thesis contributes to filling the gap in the present understanding of sputtering of multicomponent rotatable targets with deposition experiments conducted at different Ar pressures using a $Mo_{0.70}Al_{0.20}Ti_{0.10}$ target in an industrial-scale in-line magnetron sputter system. Deposition rates, chemical composition, surface topography and morphology of samples grown at different target-substrate distances d were investigated. "SRIM Supporting Software Modules" (S^3M) [76], a code initially developed by Strašík and Pavlovič for ion beam applications as a supporting routine of the "Stopping and Range of Ions in Matter" (SRIM) [106], together with subsequent data manipulation was used to model the Ar plasma following realistic geometries found in the used sputter system. Monte-Carlo simulations using SRIM were performed to investigate the sputter behavior of Mo, Al and Ti. Subsequently, SRIM scatter simulations were done to correlate experimental findings to theoretical considerations. This approach allows to explain differences in surface topography and morphology as well as chemical composition of the deposited films. Thus, a deeper understanding of the fundamental processes during deposition of multicomponent thin films from rotatable targets could be obtained.

6.2 Experimental and theoretical methods

6.2.1 Thin film deposition

An industrial-scale in-line magnetron sputter system (FHR Line.600 V), rigged with a rotatable $Mo_{0.70}Al_{0.20}Ti_{0.10}$ target (composition given as atomic fractions, dimensions ∅ 152 × 600 mm, manufactured by cold-gas-spraying [107–110], provided by Plansee SE), was used to deposit a series of thin films on (100) Si wafers (21 × 7 mm²) at Ar pressures p of 0.25, 0.42 and 0.70 Pa, corresponding to gas flows of 150, 300 and 500 sccm, respectively. All substrates were ultrasonically cleaned in acetone and ethanol before mounting on the substrate carrier in a 5 × 5 matrix at equidistant positions over the whole carrier area (550 × 550 mm², distance between samples 110 mm, see Figure 21) with Kapton tape. The base pressure of the chamber before each deposition run was below 1×10^{-5} Pa. For further substrate cleaning and surface activation, a preliminary etching step was carried out, powered by a radio-frequency (r.f.) power supply at 13.56 MHz, at an Ar pressure p of 0.32 Pa and a discharge power of 0.8 kW. The substrate carrier oscillated for 12 times with a velocity of 20 mm/s in front of

the r.f. source. During thin film deposition, the d.c. discharge power applied to the rotatable magnetron was held constant at 4 kW (power-controlled mode) for 30 min. The center of the grounded substrate carrier was kept at a constant offset of 220 mm from the target axis, i.e. held at a static position, at a target-carrier distance d_{TA} of 75 mm (see Fig. 1). No additional substrate heating was applied.

6.2.2 Thin film characterization

The obtained film thicknesses were measured using a Veeco Wyko NT1000 white light optical profilometer with Vision32 software package via automatic step measurement. All deposition rates were calculated as film thickness over time, neglecting eventual differences in film density. The topography of the films was investigated via scanning electron microscopy (SEM, Zeiss EVO 50). Cross-sections of the films were prepared via focused ion beam milling (FIB, Zeiss LEO 1540XB) with stepwise reduced ion beam currents down to 100 pA. The chemical composition of the films was evaluated via energy dispersive X-ray spectroscopy (EDX, Oxford Instruments INCA), using built-in sensitivity factors for calibration.

6.2.3 Simulation and modeling

S^3M was used to model the Ar plasma applied for sputtering of the rotatable target with characteristics close to reality. In combination with Matlab R2017b, a TRIM.dat file was generated that contained a swarm of 250,000 Ar atoms with an incident mean energy of 321 eV and energy spread of ± 1 %, corresponding to the energy of single-charged ions at the averaged experimental magnetron voltage. The spatial distribution of the incident Ar ions followed the magnetic field of the cylindrical magnetron and was modelled as a rectangle with rounded edges. The racetrack was 4 mm wide with a Gaussian density distribution from the middle of each lobe to the corresponding edges. All modelled Ar atoms were assumed to hit the target at an angle close to the surface normal in a Gaussian distribution with an average value of $\mu = 0°$ and a standard deviation of $\sigma = 3°$, as inferred from theoretical considerations [111]. All three target components, i.e. Mo, Al and Ti, were treated as single-element targets, since they are unalloyed and homogeneously distributed over the whole rotatable target used for the deposition experiments.

SRIM is capable of simulating sputter processes of arbitrary elements. In the so-called "Monolayer Collision Steps / Surface Sputtering" mode, it calculates sputter yields of the sputtered elements and records the dynamic characteristics of the sputtered atoms, namely their kinetic energy, position and direction of movement when leaving the target. This data can be recorded in a dedicated SRIM output file. With the help of S^3M, this output file can be converted to a new input file, allowing SRIM to

simulate further transport of the sputtered particles and the corresponding scatter behavior. Both, the SRIM sputter- as well as the scatter-simulations were performed using the “Ions with specific energy/angle/depth using TRIM.dat” mode within the SRIM-2013 package with SRIM-2008 Stopping Powers. Due to the reported lack of sputter yield reliability of SRIM [112], no sputter yield was determined. Instead, a sample of 50,000 sputtered atoms was randomly chosen out of the SPUTTER.txt file as a new TRIM.dat file that served for the subsequent scatter simulation. These sputtered atoms conserve all information about the ejection position within the racetrack, angle and energy when leaving the target, and hence represent a model close to reality for the subsequent scatter simulations. The scatter simulations were carried out at a medium density that corresponds to an Ar pressure p of 0.70 Pa, calculated using the ideal gas law. All atoms found in each TRANSMIT.txt file were evaluated using Matlab R2017b to analyze the corresponding transmittance of each element, the resulting lateral position and the retained energy of Mo, Al and Ti.

6.3 Results and discussion

6.3.1 Thin film deposition

Figure 21(a) shows the setup used for deposition experiments of the MoAlTi thin films grown from a rotatable $Mo_{0.70}Al_{0.20}Ti_{0.10}$ target. The Ar pressure p was varied between 0.25 and 0.70 Pa. At a given Ar pressure, comparison of film thickness over the vertical position of each substrate column A – E revealed only slight and negligible deviations from the corresponding mean values. All further film thickness data gained from the respective columns were thus averaged. The film thickness of samples positioned within column A dropped from 7.4 ± 0.6 µm for p = 0.70 Pa via 6.7 ± 0.6 µm for p = 0.42 Pa to 6.2 ± 0.3 µm for p = 0.25 Pa. The changes at extended distances represented by column E follow the same trend as observed opposite the target; the film thickness dropped from 135 ± 23 nm for p = 0.70 Pa through 130 ± 39 nm for p = 0.42 Pa to 106 ± 51 nm for p = 0.25 Pa. This reduction of the film thickness with decreasing Ar pressure is mainly related to a decrease in plasma discharge current from I = 12.8 A for p = 0.70 Pa via I = 12.3 A for p = 0.42 Pa to I = 11.4 A for p = 0.25 Pa, resulting in a drop of Ar^+ ion flux. Figure 21(b) shows the top view of the setup used for deposition experiments and emphasizes the differences of the incident angle of the particle flux from the target onto the substrates between 0 and 80 ° to the surface normal. The distance $\mathrm{d_{TA}}$ corresponds to the target-carrier distance of 75 mm. The distance $\mathrm{d_{TE}}$ depicts the longest distance between the target and any substrate covered within this study and corresponds to a distance of 446 mm, after the Pythagorean theorem. For simplification, all distances covered within this study, namely $\mathrm{d_{TA}}$, $\mathrm{d_{TB}}$, $\mathrm{d_{TC}}$, $\mathrm{d_{TD}}$ and $\mathrm{d_{TE}}$, will be referred to as d in further discussions, and only exactly referred to when necessary.

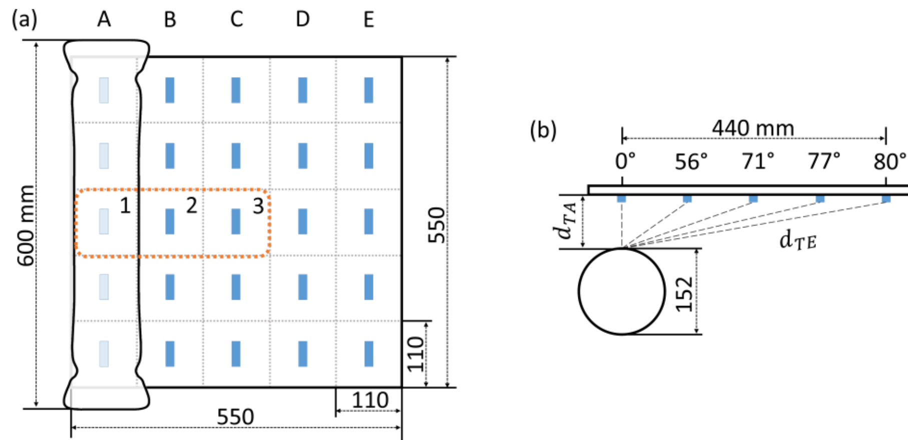

Figure 21: Schematic representation of (a) the arrangement of the 5 × 5 Si substrate (21 × 7 mm²) matrix used for deposition experiments from a $Mo_{0.70}Al_{0.20}Ti_{0.10}$ rotatable target visualized on the far left side. The arrangement of the samples was equidistant in all directions with 110 mm spacing. The samples are shown out of scale (enlarged) for better visibility. The orange dashed rectangle marks the focus of analysis for surface topography as well as FIB cross-sectional investigations and SRIM simulations; (b) the top view of the deposition setup used. The grey dashed lines visualize the incident angle of the particle-flux axis from to target towards the substrates. The distance d_{TA} corresponds to the target-carrier distance of 75 mm, d_{TE} to the longest distance between the target and any substrate covered within this study, namely 446 mm.

Figure 22 gives an overview of averaged deposition rates versus the product $p \cdot d$, allowing a direct comparison of deposition runs at different Ar pressures p. All data points that are connected by dashed lines represent equivalent sample positions at different Ar pressures. When comparing the slopes of these dashed lines, one can observe mainly two different areas, namely with or without Ar pressure-dependent deposition rates (indicated by the reddish and blueish backgrounds, respectively). This directly leads to the assumption that two different growth regimes could exist next to each other: a high-flux area opposite the magnetron and a low-flux area at extended distances to the target. The high-flux area exhibits a direct Ar pressure-dependent deposition rate, whereas the low-flux area exhibits an Ar pressure-independent deposition rate. In both cases, the sputtered atoms experience a different number of collisions with other atoms during their transport through the gas. When comparing the deposition rates of columns A and B, both located within the high-flux area, a pronounced drop is visible. This drop by 50 % can be explained by the geometrical form of the rotatable target. According to Depla et al., rotatable targets feature two “beams” of atom fluxes in an azimuthal angle of ±10 ° < θ < ±35 ° with respect to the 0 ° surface normal on the substrate carrier [113], stemming from the arrangement of the permanent magnets below the parallel erosion tracks. Taking the geometrical arrangement of the substrates on the sample carrier into account (see Figure 21), it can be assumed that samples in column A are exposed to both beams, while samples in column B are only exposed to one beam, resulting in the 50 % drop of the atom flux arriving at the substrate.

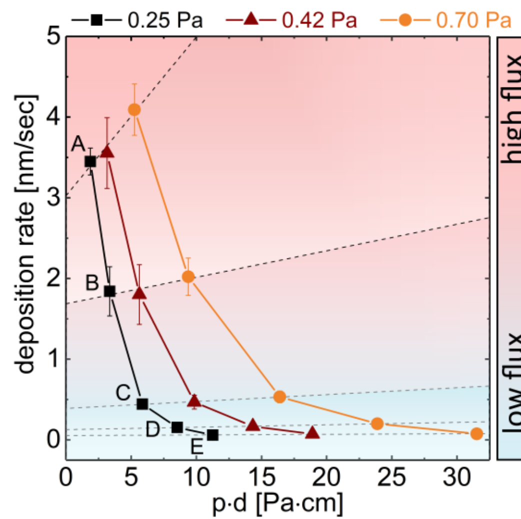

Figure 22: Deposition rates determined for different Ar pressures p, but equivalent sample positions (columns A-E) on the substrate carrier. Dashed lines are drawn to guide the eye, connecting equivalent sample positions at different Ar pressures. Two different flux regimes can be distinguished, namely (i) a high-flux area opposite the target with direct Ar pressure-dependent deposition rates (reddish background), and (ii) a low-flux area with Ar pressure-independent deposition rates (blueish background).

As mentioned above, the sputtered atoms will experience a different number of collisions with other atoms during their transport through the gas. The concept of the thermal mean free path (λ), as described by Equation 4 in section 2.2, with atomic radii (r_{Ar} = 71 pm, [114], $r_M = r_{Metal}$, namely r_{Mo} = 145 pm, r_{Al} = 125 pm, r_{Ti} = 140 pm, [115]), allows to obtain further insights into the average number of collisions the sputtered atoms undergo during the transport through the gas [35]. λ expresses the average distance between two subsequent collisions for an arbitrary atom with defined characteristics. Enhanced temperatures as well as low gas pressures allow atoms to travel farther without collision. According to Westwood [111], bombardment of the growing film with energetic particles, i.e. sputtered target atoms, Ar atoms reflected from the target, ions and electrons, and the concomitant kinetic energy-transfer to the growing film will – in addition to radiation from the plasma and the target surface – contribute to a rise of the surface temperature of the substrates. Westwood reported on substrate temperatures of 300 °C achieved during bombardment with Au atoms having a mean kinetic energy of 13 eV [111]. For the sputter system used within this work, Jörg et al. reported significant heating of the surface of samples placed on the substrate carrier opposite the target with temperatures reaching values above 500 K for deposition times > 5 min [7,89]. Substrate heating also strongly depends on the power applied to the target. Consequently, high powers yield increased substrate temperatures after short sputtering times, whereas for reaching a steady-state temperature plateau at low powers a considerable time is needed. For a deposition time of 30 min, as used within this work, pronounced temperature differences within the sputter system,

in particular on the surface of the substrates opposite the target and at extended positions, will exist. Based on the considerations summarized above, a maximum substrate temperature of 500 K opposite the target, corresponding to column A, was assumed. At extended distance, i.e. the low-flux area, the number of sputtered atoms arriving with high energies is much smaller. Therefore, within this work a temperature of 300 K was assumed for substrates at extended distances, corresponding to column E. Since no external heating was applied, all heating effects of the substrates stem from the kinetic energy of energetic species arriving at the substrates and from radiation effects [111]. Since the individual contribution of these effects is unknown and hardly accessible in an industrial-scale magnetron sputter system, an Ar background gas temperature of 500 K, corresponding to the substrate temperature plateau determined by Jörg et al. [7,89] at an equilibrium state, was assumed to calculate λ of sputtered atoms travelling from the target towards column A. Likewise, for sputtered atoms travelling towards column E, a gas temperature of 300 K, corresponding to room temperature, seems to be appropriate. With these assumptions, λ for atoms travelling the distance d_{TA}, i.e. the shortest distance between the target and the substrate carrier, nearly doubles compared to atoms traveling the distance d_{TE}. In order to calculate the average number of collisions via target-substrate distance over λ, a temperature of 500 K was assumed for the distance of 75 mm, corresponding to the target-carrier distance d_{TA}. For a temperature of 300 K, a target-substrate distance d_{TE} of 446 mm was assumed (see Figure 21). Since in reality a temperature gradient exists, the true number of collisions of sputtered atoms on their path from the target to the substrate at extended positions can be assumed to lie somewhere in between the number of collisions at 300 K and 500 K. Table 2 gives an overview on λ for Mo, Al and Ti at 300 and 500 K together with the corresponding average number of collisions with Ar atoms on their way towards the substrate (N).

Besides the differences of λ for different atomic species, head-to-head collisions of atoms with different atomic mass result in different amounts of effective energy transfer ε [35], as defined in Equation 1 in section 2.1, for the atomic mass of Ar (m_{Ar} = 39.95 u) and the atomic mass of sputtered metal atoms ($m_M = m_{Metal},$ namely m_{Mo} = 95.95 u, m_{Al} = 26.98 u, m_{Ti} = 47.87 u). As stated by Depla et al., it can be assumed that scattering of the sputtered atoms is dominated by elastic collisions with neutral background gas atoms, since the overall number of sputtered atoms is negligibly small compared to the background gas atoms [58,116,117]. It is hence justified for further considerations that only collisions of metal with Ar atoms are taken into account. As expressed by Equation 1 in section 2.1, different fractions of kinetic energy are transferred during collisions of different elements. Since the effective energy transfer is most pronounced for atoms of similar weight, ε for Ar collisions with Ti yields a value of 0.99, with Al a value of 0.96 and with Mo a value of 0.83. As a consequence, it can be

expected that heavy Mo atoms retain more of their initial energy and direction while colliding with Ar compared to Ti and Al that are closer to the maximum energy transfer. The lower effective energy transfer of Mo should also lead to higher energies of Mo atoms that approach the film, allowing re-sputtering of other elements. In other words, for films deposited at low $p \cdot d$ values, an enrichment by heavy atoms can be expected opposite the target with a depletion by lighter elements. For extended distances, i.e. higher $p \cdot d$ values, a reverse trend should be observed.

Table 2: Overview of the mean free paths λ and the corresponding average number of collisions N for Mo, Al and Ti at Ar pressures of 0.25 and 0.70 Pa, respectively. The mean free paths were calculated using Equation 4 defined in section 2.2, with the assumption of an Ar gas temperature of 500 K opposite the target and 300 K at extended distances. The average number of collisions N was calculated as quotient of the target-substrate distance d_{TA} and d_{TE} over λ.

		λ [mm]			N [-]		
		Mo	**Al**	**Ti**	**Mo**	**Al**	**Ti**
0.25 Pa	$\mathbf{d_{TA}}$ **(500 K)**	133	162	140	0.6	0.5	0.5
	$\mathbf{d_{TE}}$ **(300 K)**	79.9	97.0	83.7	5.6	4.6	5.3
0.70 Pa	$\mathbf{d_{TA}}$ **(500 K)**	47.6	57.8	49.8	1.6	1.3	1.5
	$\mathbf{d_{TE}}$ **(300 K)**	28.5	34.7	29.9	16	13	15

6.3.2 Chemical composition

In order to study the chemical composition of the films and correlate it to the scatter behavior of different elements, EDX analyses were conducted for all samples of columns A – C. The results were averaged column by column. The limited film thicknesses of samples from columns D and E of less than 350 nm prevent reliable EDX analyses for any of those samples and were excluded. As also observed in Ref. [35], up to 28 % of oxygen was detected by EDX, exclusively for samples at extended positions (column C) with open and voided morphologies, as will be shown below, but never opposite the target. This can most probably be attributed to *ex situ* oxidation processes taking place after breaking the vacuum, since no nitrogen could be detected. Referring to Neidhardt et al., the presence of nitrogen would be the case for *in situ* incorporation due to outgassing or leaks [35]. Since this study focuses on the scatter behavior of elements of different atomic weights, all EDX results were normalized to 100 % for the three elements Mo, Al and Ti; oxygen was neglected.

As shown in Figure 23, the chemical composition of the grown films is influenced by both factors, the Ar pressure as well as the target-substrate distance. In terms of the $p \cdot d$ value, higher $p \cdot d$ values lead to a depletion of heavy elements and an enrichment of light elements in the films, as predicted by the

theoretical considerations above. The Ti content seems to be influenced by a change of $p \cdot d$ less drastically than the Mo and Al content. The chemical composition of the resulting thin films is influenced by many factors, among of which the initial target emission characteristics of Mo, Al and Ti, the probability of Mo, Al and Ti atoms to be re-sputtered within the growing films by metal and Ar atoms as well as the respective scatter angles of Mo, Al and Ti during the transport through the gas play a crucial role for the resulting chemical composition of the thin films. Although the exact emission characteristics of Mo, Al and Ti, i.e. emission angle and position, are not known for the rotatable target used within this study, they can be considered to remain comparable to each other within the investigated Ar pressure range [35]. Their impact on the differences in chemical composition in dependence of the Ar pressure can be neglected. When comparing the sputter yields of Mo (0.58), Al (0.65) and Ti (0.33) sputtered with 300 eV Ar^+ ions published by Laegreid and Wehner [118], it is evident that Al is sputtered by a factor of 2 more effectively than Ti. When assuming high residual energies of atoms arriving at the substrate within the high-flux area opposite the target, preferential re-sputtering of Al over Ti could explain the observed higher Al depletion. However, since the published sputter yields of Mo and Al are comparable, Mo depletion should be expected as well. Instead, Mo enrichment is observed. Thus, in combination with the observed enrichment of lighter elements in the corresponding films at higher $p \cdot d$ values (see Figure 23), it has to be concluded that Al is scattered much more effectively than Mo. This is in agreement with Equation 5, section 2.2, defining the maximum possible scatter angle between two particles of different mass ($\theta^{\max}$). Due to the pronounced differences of the low energy of Ar background gas atoms, corresponding to the thermal energy of Ar (T_{Ar}), and the energy of the sputtered metal atoms, the Ar atoms can be considered at rest compared to the sputtered metal atoms in motion. When $m_M < m_{Ar}$, as for Al, sputtered atoms can be scattered in any direction. In contrast, when $m_M > m_{Ar}$, as for Mo and Ti, the scatter angle of heavy atoms is much smaller than for light atoms. This contributes to an enrichment of Al in the thin films deposited at higher $p \cdot d$ values.

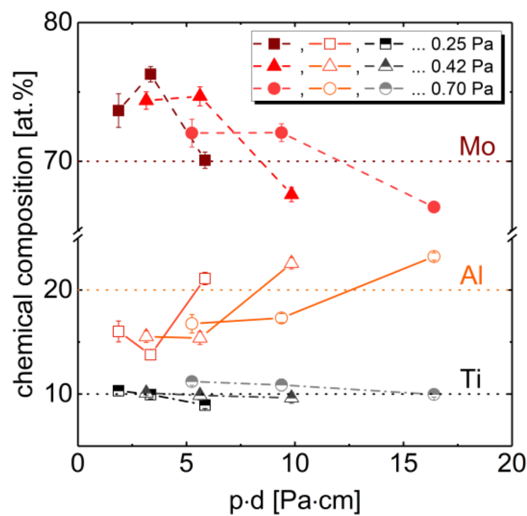

Figure 23: Overview of the chemical composition of the central samples of columns A (small $p \cdot d$), B (medium $p \cdot d$) and C (high $p \cdot d$ values - see Figure 21) grown at different Ar pressures. The dashed lines indicate the target composition. Directly opposite the target, a strong Al depletion in contrast to a pronounced Mo enrichment with respect to the target composition is visible, changing to an opposite trend at extended distances. The Ti content remains comparable with the initial target composition over $p \cdot d$.

6.3.3 Film morphology

Subsequently, the surface topography and cross-sectional morphologies of the deposited thin films were investigated using SEM and FIB analyses techniques. The first row of Figure 24 presents SEM micrographs of the surface topography of the films grown on central samples of columns A, B and C, marked as positions 1 to 3 in Figure 21, at an Ar pressure of 0.70 Pa (1-3a) and 0.25 Pa (3b). Samples at positions 1 and 2 show a predominantly fish scale like surface pattern, probably stemming from non-equiaxed columnar grain growth. This morphology is assumed to develop when initial nuclei having different crystallographic orientations are covered by faster growing grains via a Volmer-Weber like growth with coalescence of islands of different preferential orientation. This is known as competitive growth or evolutionary selection [8,87]. The 90 ° change in orientation of the surface patterns of both samples is the result of the sample at position 1 being exactly opposite the target and the sample at position 2 at a 110 mm offset, with atoms consequently arriving from the left (see Figure 21). In both cases, condensed atoms exhibit high surface mobility and are able to move freely to already existing bigger islands. This mobility is promoted by the combination of the kinetic energy of the sputtered atoms, being conserved throughout the transport through the gas with fewer collisions occurring at low $p \cdot d$ values, with high substrate temperature observed in the sputter system used within this work [7,119]. All samples grown at the Ar pressures used within this study that were located at position 1 and 2 had similar surface patterns. In contrast to position 1 and 2, sample 3a features a completely different topography; fine isolated grains over the whole area. This can be attributed to limited adatom

mobility of thermalized atoms that condense at extended distances. According to Westwood [111], the thermalized atoms exhibit only the thermal energy of Ar atoms (T_{Ar}) due to the high number of collisions during their transport through the gas. Comparing the surface topography of micrographs 3a and 3b in Figure 24(a) allows to correlate adatom mobility and the resulting film topography at equivalent sample positions: The topography of sample 3b, a film grown at 0.25 Pa, is characterized by fine grains that are linked to each other. Lower Ar pressure means that atoms that are transported through the gas experience a smaller number of collisions. In turn, this leads to higher energies of the condensed adatoms, resulting in greater mobility and allows the adatoms to move to already existing and growing grains.

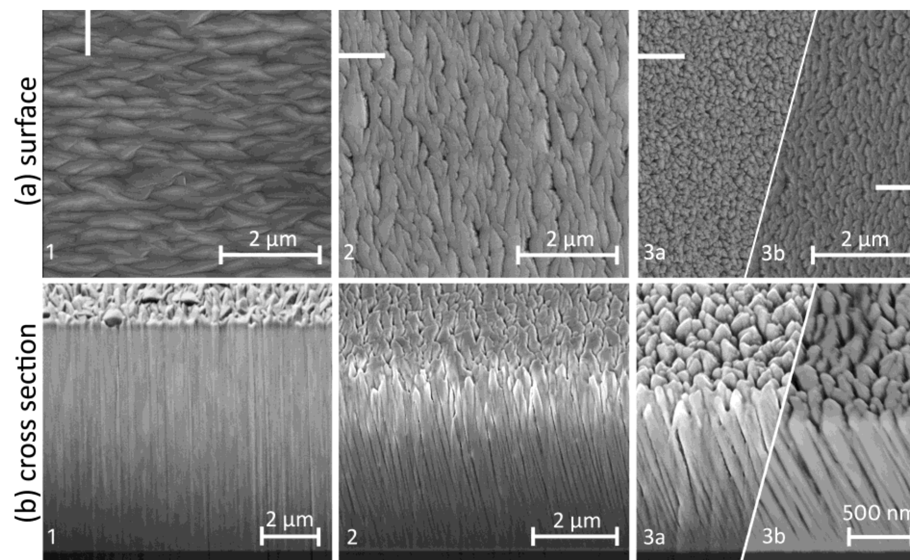

Figure 24: SEM micrographs of (a) the surface topography of the films grown at positions 1, 2 and 3 (see Fig. 1) at an Ar pressure of 0.70 Pa (1 – 3a) and 0.25 Pa (3b) and (b) FIB cross-sections showing pronounced differences in morphology and density of the films. The solid white lines in (a) indicate the direction of the FIB cuts. Directly opposite the target, a fish scale like topography is predominant that changes to a fine granular structure at extended distances. Micrographs 3a and 3b show the surface topography and cross-sections of samples grown at position 3, whereby 3b shows a more island-like structure than 3a. Lower Ar pressure seems to favor more energetic atoms to arrive at extended positions leading to a higher probability of coalescence.

Similar conclusions can be drawn from FIB cross-sections (see Figure 24(b)). Samples at position 1 have a densely packed morphology with straight fibrous columns perpendicular to the substrate surface. With increasing distance d, two main differences in the developing morphology are evident: (*i*) The angle of the single columns deviates from the substrate surface normal and is tilted towards the target, i.e. towards the direction of the arriving atoms. The Ar pressure has a direct influence on this angle (see Figure 24(b), sample 3b). This is in good agreement with the notion of higher adatom mobility at lower Ar pressures favoring coalescence, since the atoms that arrive on the film surface exhibit a more pronounced direct atom flux from the target surface compared to the much less directed movement

of the thermalized particles (see Figure 24(b), sample 3a). (*ii*) The film density decreases with increasing distance from the target, from column A to column C (see Figure 24(b)). This decrease in density in reverse leads to a greater surface area, increasing the overall number of potential *ex situ* oxidation sites and explains the amount of oxygen found by EDX, thus justifying its neglect.

6.3.4 SRIM SIMULATIONS

Since the experiments performed within this work indicate a high influence of collision processes of the sputtered particles with Ar atoms during the transport through the gas on both, the chemical composition as well as the topography of the deposited thin films, Monte-Carlo simulations using SRIM were conducted to receive further insights. Because of the limited practical value of the mono-energetic point-like source SRIM normally provides, the Monte-Carlo simulations were combined with S^3M [76] and subsequent data manipulation using Matlab R2017b. This combination brought the simulations much closer to reality. The resulting SRIM-input TRIM.dat file, containing all necessary Ar plasma information, was used for the sputter simulations of Mo, Al and Ti single element targets. Although the reliability of the SRIM code for determination of sputter yields was questioned by Witmaack et al. [112], this approach seems to be more expedient than modeling of the already sputtered atoms with simplified initial characteristics for subsequent scatter simulations. In that case, many more assumptions, i.e. emission position, angular and energetic distributions, would have to be drawn. In order to investigate the sputter yield reliability of SRIM, sputter calculations were conducted to determine the sputter yield of Mo at normal incident and energies between 0 and 600 eV. Compared to experimental data published by Laegreid and Wehner [118] SRIM overestimates the sputter yield by 30 %. To circumvent the as described drawbacks of SRIM, 250,000 Ar atoms were used for sputter simulations of Mo, Al and Ti. In the next step, a sample of 50,000 sputtered atoms was randomly chosen for subsequent scatter simulations from the SPUTTER.txt file. Figure 25 shows an overview of the simulated kinetic energy distributions of 50,000 sputtered Mo, Al and Ti atoms each when leaving the target. Ti possesses the highest energy of sputtered atoms with a maximum energy E_{max} of 317 eV. This energy corresponds to the voltage applied on the magnetron to achieve the observed deposition rates of a few nm per second (see Figure 22). E_{max} for sputtered Mo and Al atoms yields values of 249 eV and 101 eV, respectively. Accordingly, sputtered atoms exhibit energies far beyond the sputter threshold limit for all metals present within the studied multicomponent target, i.e. 24 eV for Mo, 13 eV for Al and 20 eV for Ti [120]. With respect to these values, 44 %, 19 % and 37 % of sputtered Mo, Al and Ti atoms simulated by SRIM possess energies that exceed these sputter threshold limits, enabling re-sputtering of the growing film when being transmitted successfully without collisions with any Ar background gas atoms.

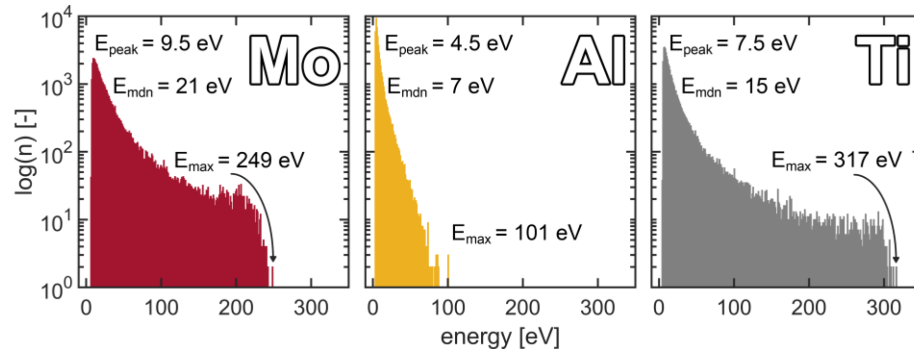

Figure 25: Logarithmic energy distributions of Mo, Al and Ti atoms sputtered with 321 eV Ar when leaving the target. The letter n represents the number of particles. The overall sum of 50,000 sputtered atoms is equal for each element. Pronounced differences in the initial energy spectra of the sputtered atoms are clearly observable, as visible in the peak energies E_{peak}, representing the energies of sputtered atoms with the highest abundance, the median energies E_{mdn}, and the maximum energies E_{max} reached by any sputtered atom.

For subsequent SRIM scatter simulations, an Ar pressure of 0.70 Pa was chosen to meet experimental conditions. The ideal gas law was used to determine the corresponding Ar gas density. The data gained from the sputter simulations of Mo, Al and Ti were converted to new TRIM.dat files and used for subsequent scatter simulations. All atoms that are successfully transmitted through the gas and arrive at the substrate are stored in the SRIM-output TRANSMIT.txt file with information about position, retained energy and incident angle. In the case of Mo, Al and Ti, 90 %, 54 % and 74 % of the sputtered atoms are transmitted over the target-carrier distance d_{TA} = 75 mm, respectively. All other atoms are per definition thermalized in the gas before reaching the substrates.

Figure 26 shows the resulting lateral position distribution of scattered Mo, Al and Ti atoms recorded in TRANSMIT.txt. Each square is equal to a 110 × 110 mm² wide area, exactly representing positions 1, 2 and 3 (see Figure 21). Since the geometrical setup for the simulation was chosen to have equal dimensions, simulation and experiments are directly comparable. The initial sputter simulations using the predefined Ar plasma resulted in two relatively sharp erosion tracks of 10 mm width each, separated by 40 mm, i.e. positioned at x = -20 mm and x = 20 mm. The subsequent transport simulation resulted in a re-distribution of these atoms over the whole area of the substrate carrier via elastic scattering, as visible in Figure 26. The original position distribution of the sputtered particles is no longer preserved. In contrary, a gradient of the number of the transmitted atoms over the whole substrate carrier from an absolute maximum at position 1 via less atoms at position 2 to a minimum at position 3 is created. It has to be noted that only non-thermalized atoms are depicted in Figure 26. All other atoms are not recorded in the TRANSMIT.txt file and hence not displayed in Figure 26.

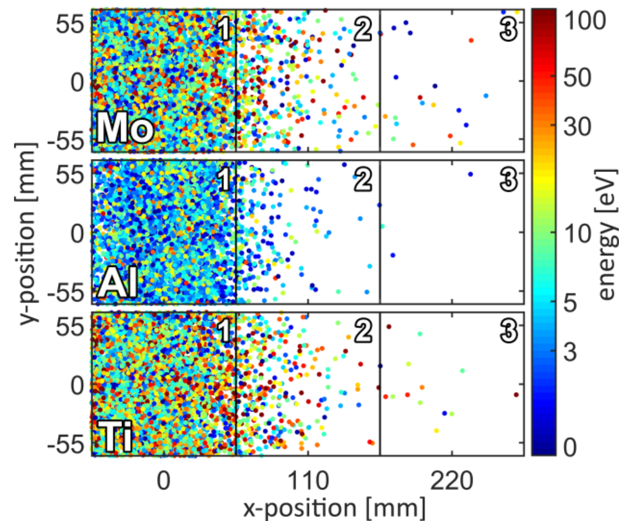

Figure 26: The resulting lateral positions, corresponding to positions 1, 2 and 3 (see Fig. 1) and retained energies of transmitted atoms after SRIM scatter simulations of sputtered Mo, Al and Ti at an Ar pressure of 0.70 Pa.

As visible in Figure 27, there is a correlation between incident energy of transmitted atoms and horizontal distance from the target. Not only does the overall number of transmitted atoms decrease with increasing distance, but also the energies of the atoms. These findings can be attributed to the higher number of collisions with Ar atoms during the transport of the sputtered atoms through the gas and the resulting loss of their kinetic energy. The high number of Ti atoms with energies >250 eV, as observed for the sputtered atoms (see Figure 25), vanished completely and the energy distribution of Ti leveled towards the energy distribution of Mo. The retained energies, as well as the overall number of transmitted atoms, experience a pronounced drop at position 2, but still a large number of transmitted atoms preserve energies above the reported sputter threshold limits of Mo, Al and Ti [120] when arriving at the substrate.

With observed retained energies of over 200 eV for Mo and Ti projectiles exactly opposite the target (position 1), re-sputtering of the growing films will take place. When applying Equation 1, defined in section 2.1, the effective energy transfer ε of Ti to Mo yields a value of 0.89, for Ti to Al of 0.92, for Mo to Ti of 0.89, and for Mo to Al of 0.69 (the maximum energy transfer is 1 for identical atomic species). The energies of the incoming Mo and Ti atoms are directly comparable (see Figure 27), but due to the more effective energy transfer of Ti to Al compared to Mo to Al, Ti can be considered as the main source of re-sputtering (besides re-sputtering via recoiled Ar atoms). This re-sputtering could explain the observed depletion of Al at low $p \cdot d$ values supplementary to the larger scatter angle of light elements.

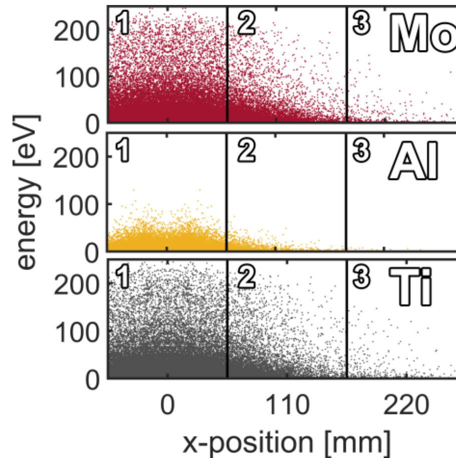

Figure 27: Energy-to-position correlation plots of transmitted Mo, Al and Ti atoms at an Ar pressure of 0.70 Pa sputtered by 321 eV Ar atoms when arriving at the substrates. The probability that a particle reaches a distant position with high retained energy decreases with increasing horizontal distance from the target and can be attributed to a higher number of collisions with Ar atoms during the transport through the gas with longer traveling distance.

Most of the atoms at position 3 exhibit only small energies after the transport through the gas. This position corresponds to the experimentally found open voided film topography and morphology (see Figure 24) and thus confirms the notion that adatoms arriving at substrates positioned at extended distances have only limited to thermal energy, which results in finite mobility and growth of small isolated grains. These findings can be expanded by a model suggested by Rossnagel et al. [29]. They described three regimes to appear during the transport through the gas of atoms from multicomponent targets depending on the gas pressure, namely: (*i*) a ballistic regime at very low gas pressures with linear travel paths of the sputtered atoms with no collisions with Ar atoms, where the film composition should reflect the target composition, (*ii*) an intermediate regime at higher gas pressures, mostly affecting the directional movement of lighter elements due to more pronounced scattering, shifting the film composition opposite the targets towards the heavier element with a reverse trend at extended distances, and (*iii*) a diffusive regime at high gas pressures with an opposite trend because of an increase in the effective scattering of heavy elements as well. When applying their findings to the current thesis, all three different growth regimes can only be found for thin films deposited at an Ar pressure p of 0.25 Pa (see Figure 23). The Mo content opposite the target, i.e. for the smallest $p \cdot d$ value of 1.9 Pa·cm, is smaller compared to the Mo content at position 2, corresponding to a $p \cdot d$ value of 3.3 Pa·cm. This increased value drops again at extended distances, i.e. a $p \cdot d$ value of 5.9 Pa·cm. For Al, an opposite trend is visible. From these findings, it can be concluded that for the smallest $p \cdot d$ value, a ballistic regime with no Ar collisions of sputtered metal atoms is predominant, being in perfect agreement with the values of λ being greater than the target-carrier distance d_{TA} of 75 mm and the average number of collisions <1 (see Table 2).

The increasing number of collisions of sputtered atoms with Ar atoms during the transport through the gas starts to influence the resulting chemical composition of thin films at $p \cdot d$ values >3.3 Pa·cm, corresponding to the diffusive regime described by Rossnagel et al. For higher Ar pressures covered within this study, namely 0.42 Pa and 0.70 Pa, it seems that only the intermediate regime is observable. This regime is schematically visualized and generalized in Figure 28 with the effect of re-sputtering being added. In general, a high- and a low-flux area have to be distinguished. For the high-flux area, which is predominant opposite the target and for small $p \cdot d$ values, the atoms that arrive at the substrate have higher energies due to less scatter processes during the transport through the gas compared to atoms arriving at extended distances. Those energies allow the adatoms to move freely on the surface and decrease their surface energy through coalescence with already existing grains (see Figure 28(a)). Besides the higher mobility, the energy of the arriving metal atoms which reaches values exceeding 200 eV enables preferential re-sputtering, depending on the species and mass of both, the projectile and the film (see Figure 28(b)). For low-fluxes, resulting from scatter-dominated movement of (nearly) thermalized atoms in the gas, low adatom mobility on the growing film leads to fine grains and open voided structures (see Figure 28(c)).

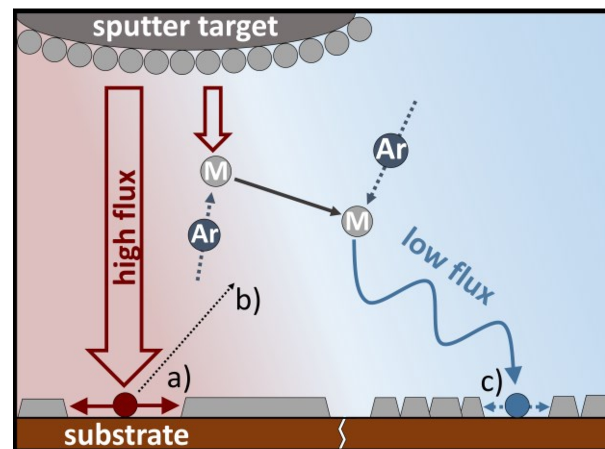

Figure 28: Schematic representation of different growth regimes, namely a high-flux (reddish coloration) and a low-flux (blueish coloration) area. The higher energy of arriving atoms in the high-flux area allows preferential re-sputtering of arbitrary atoms (b). In turn, this energy results in a high adatom surface mobility (a) compared to the low-flux area (c). The lower energy for arriving atoms at extended distances (c) limits their adatom mobility and leads to fine grains and open voided structures.

6.4 Conclusions

MoAlTi thin films, applicable in microelectronics as well as display applications, were deposited from a cold-gas-sprayed multicomponent rotatable target mounted in an in-line magnetron sputter system and systematically investigated. The chosen system with pronounced differences in atomic mass of Mo, Al and Ti turned out to be a well suited model system to investigate the effects of scattering on the chemical composition and topography of the deposited films. A larger scatter angle for lighter elements during the transport through the gas leads to a depletion by light elements with an enrichment by heavy elements in the high-flux regime opposite the target with reverse trends observable within the low-flux regime at extended distances. The combination of experimental results with Monte Carlo computer simulations allowed to distinguish a high- and low-flux regime with pronounced differences in growth conditions. In addition to a correlation between scatter angle and particle mass, re-sputtering has been identified as another important factor influencing the growth conditions of multicomponent thin films. The study improves our present understanding of thin film growth from multicomponent rotatable targets and can be employed to a large variety of target systems with atoms of different atomic mass.

Chapter 7 is based on a manuscript in final preparation to be submitted for publication. In the current thesis, all superfluous equations were replaced with references to the main text. Moreover, the figure numbering was adapted to fit to the thesis.

7. Angular resolved mass-energy analysis of species emitted from a d.c. magnetron sputtered NiW-target

7.1 Introduction

Modern magnetron sputter deposited thin films often consist of multiple elements and are being applied for a large variety of technological applications. For basic research on a laboratory-scale, these films are often deposited via co-sputtering from the respective single element targets. On an industrial-scale, films are commonly grown from multi-element targets. Compared to co-sputtering from single element targets, these multi-element targets ensure the required process stability on a large scale [25]. However, with the use of multiple elements with considerable mass differences in a single target, various challenges arise for the deposition of homogeneous thin films [49]:

(*i*) Element-specific differences in sputter yield (Y), emission angles with respect to the target normal (θ), and energy distributions change the lateral composition of large-area coatings [33,35–37,45].

(*ii*) Depending on the mass of the target constituents, considerable amounts of Ar^+ ions are reflected from the target as Ar neutrals. These Ar neutrals have energies corresponding to the target acceleration voltage of some 100 V and may lead to selective re-sputtering of the growing film [57].

(*iii*) Mass-dependent energy transfer coefficients (ε) and scattering angles (α) for collisions of sputtered species with background gas atoms influence the respective trajectories, energies, and consequently the film composition [29,31,32,35,37,38,47–49].

(i*v*) The mass and charge state of the impinging species on the growing film surface and its respective ion energy distribution function (IEDF) determines the sticking coefficient of the film-forming species and the amount of selective re-sputtering [32,33,38–40,42,49].

(*v*) The substrate temperature influences the degree of selective thermal desorption of film-forming species as well as selective surface segregation, exacerbating the effect of selective re-sputtering [25,33,41].

(*vi*) The use of a substrate bias or reactive magnetron sputtering even increases the complexity of the deposition process due to the contribution of highly energetic and/or reactive particles to film growth [25,36,40].

Although being studied extensively, both on laboratory- and industrial-scale for various material systems [25,27–49], to date hardly any general rules can be drawn for the deposition behavior of multi-element targets. Either light elements [27–37] or heavy elements are enriched opposite the target [25,38–49]. This – on the first sight contradicting result – represents the complexity of sputtering of multicomponent systems. Not only the mass-difference between the target constituents, but also the specific target composition, the manufacturing process of the target, the nature of the film-forming species, the used background gas, and the deposition chamber design and its geometry influence the final film composition.

The goal of the current thesis is to shed light on the impact of emission angles of sputtered species, scattering events, and re-sputtering on the final composition of films grown from a Ni81W19 target. The combination of angular resolved mass-energy analyzer (MEA) measurements and angular resolved film deposition experiments was utilized to unravel the complex interplay between film composition, scattering, re-sputtering and angular distribution of the sputtered flux.

7.2 Experimental methods

In the current thesis, the designation Ni81W19 refers to an elemental composition in at.%, whereas the notation Ni_4W refers to an intermetallic compound.

7.2.1 Angular resolved plasma characterization

A circular planar Ni81W19 target with the dimension Ø 90 × 6mm² (manufactured by cold-gas-spraying [107,108,110], with 3 mm of Ni81W19 on a Ti plate of 3 mm thickness, provided by Plansee SE) was attached to a Cu backing plate and mounted in a DN160 six-way cross. The particularity of the used sputter system is its custom-built magnetron tiltable by +/- 90° (Figure 29(a)). The base pressure of the system of < 1.1×10^{-3} Pa was achieved by a combination of a rotary-vane pump (Edwards E2M28) and a turbomolecular pump (Pfeiffer Vacuum TPU 240). A mass-energy analyzer (MEA, Pfeiffer Vacuum plasma process monitor PPM 422) with a grounded 0.1 mm diameter orifice was mounted opposite the target on the target axis at a distance of d = 80 mm. The arrangement was used to measure the population (*i*) of ions with energies between 0 and 50 eV at fixed mass (energy scan), to assess the ion energy distribution functions (IEDF) and (*ii*) of ions with mass between 0 and 200 amu at fixed energy (mass scan) at any angle θ = ± 90°.

The MEA-measurements were conducted at Ar pressures p of 0.09, 0.13, 0.26, 0.43, 0.62 and 1.07 Pa, in order to receive information of the plasma composition, represented by ions impinging on the growing films in a pressure range relevant for magnetron sputtering. The target was operated with a d.c. power supply (Advanced Energy MDX-5K) that was held at a constant power of 100 W (power-controlled mode, target power density 1.57 W/cm²). Before each experiment, the target was sputter cleaned in Ar for 15 min in order to achieve constant conditions for all performed measurements. The resulting target voltages (U_{MEA}) and currents (I_{MEA}) are summarized in Table 3.

Table 3: Target voltages and currents for the performed MEA experiments (U_{MEA} and I_{MEA}, respectively) and film depositions (U_{dc} and I_{dc}, respectively).

p [Pa]	U_{MEA} [V]	I_{MEA} [A]	U_{dc} [V]	I_{dc} [A]
0.09	503	0.20	500	0.20
0.13	442	0.23	-	-
0.26	448	0.22	425	0.24
0.43	430	0.23	-	-
0.62	421	0.24	-	-
1.07	425	0.24	412	0.24

The MEA-measurements carried out in steps of 10°at θ from 0 to 90°, providing the angular-resolved information of the plasma, comprised of (*i*) an energy-scan of $^{40}Ar^{+}$ to determine the specific energy with the highest signal intensity (I_{peak}) of this ion, followed by (*ii*) a mass-scan at this specific energy. Subsequently, (*iii*) energy-scans of $^{40}Ar^{+}$, $^{58}Ni^{+}$ and $^{184}W^{+}$, corresponding to the isotopes with the highest natural abundance (Table 4), were recorded. The collected RAW data was converted to ASCII files and evaluated using Matlab R2019a. Right before plotting, the data was treated with the Matlab function *smoothdata*. This function considers the average of ±10 measurement points for every data point in order to eliminate excessive noise from the measurement. 2D plots were prepared using the *contourf* function of Matlab.

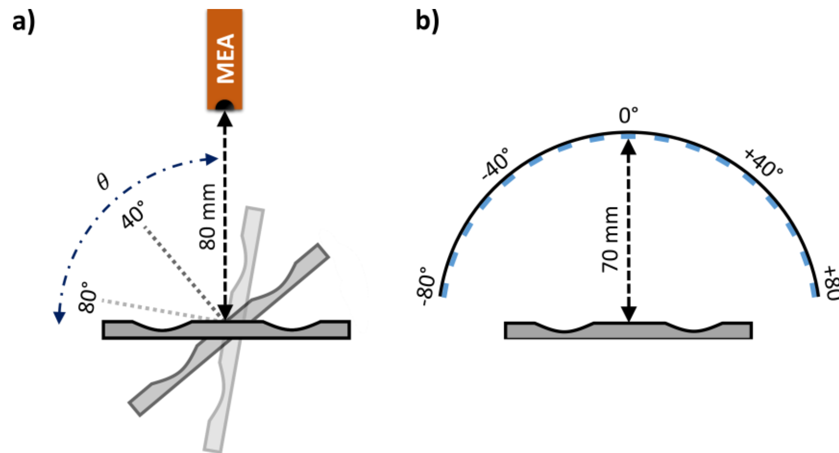

Figure 29: Geometrical arrangement used for (a) mass-energy analyzer (MEA) measurements and (b) film deposition. The distance of the MEA from the target center was held constant at 80 mm. The distance from all substrates to target center was constant at 70 mm. θ defines the angle of the MEA or substrate axis with respect to the target normal, as indicated in (a).

7.2.2 Thin film deposition

To correlate MEA-measurements with film deposition experiments, a spherical-shell Al substrate holder with a width of 30 mm, covering the examined angles at deposition positions from θ = 0 to 80° in steps of 10° (Figure 29 (b)), was used to deposit a series of films on (100) Si substrates at Ar pressures p of 0.09, 0.26 and 1.07 Pa. The chosen pressures correspond to the pressures with the most pronounced changes observed in the MEA-measurements. The distance from substrate to target was equivalent for all samples at d = 70 mm. Before mounting on the substrate holder (held on floating potential) with Kapton tape, the substrates were ultrasonically cleaned in isopropanol for 10 min. The base pressure of the chamber before each deposition was < 3×10^{-4} Pa. To further clean the substrates and increase the film adhesion, an etching step was carried out before each deposition at an Ar pressure p of 1.07 Pa for 15 min. This etching was powered by an asymmetrically bipolar pulsed d.c. power supply (ENI RPG-100) at a constant power of 50 W, a frequency of 150 kHz and a pulse duration of 4.65 µs. For thin film deposition, a d.c. power supply (Advanced Energy MDX-5K) was operated at a constant power of 100 W (power-controlled mode) for 60 min. The resulting target voltages (U_{dc}) and currents (I_{dc}) are shown in Table 3. No additional substrate heating was applied, however, due to the deposition time of 1 h, a substrate holder/gas temperature of 400 K can be assumed [49]. Since the substrate holder was made from thermally well conductive Al, the substrate temperature is considered to be constant for all films grown at different θ.

7.2.3 Thin film characterization

The film thickness was measured using a white light optical profilometer (Veeco Wyko NT1000) with Vision64 software package. Scanning electron microscopy (SEM, Zeiss LEO 1525) was used for film

surface investigations and focused ion beam milling (FIB, Zeiss LEO 1540XB), with stepwise reduced ion beam currents down to 100 pA, was used for cross-sectional studies of the obtained films. Energy dispersive X-ray spectroscopy (EDX, Oxford Instruments INCA), using built-in sensitivity factors for calibration, was used to investigate the elemental composition of the deposited thin films. For selected films, the elemental composition was measured by X-ray fluorescence (XRF, Thermo Scientific ARL 8410), yielding a linear relationship between EDX and XRF data. All EDX data were then corrected using this calibration.

7.3 Results and discussion

7.3.1 Angular resolved plasma characterization

7.3.1.1 MEA mass-scans

An overview of species detected at different θ angles in an Ar sputter plasma at p = 0.09 Pa is shown in Figure 30. At this pressure, a collision free trajectory from the target to the mass-energy analyzer can be assumed [9]. In order to improve readability, the current thesis uses the $^{A}_{Z}E$ notation for isotopes (i.e., $^{40}Ar^{+}$, $^{58}Ni^{+}$ and $^{184}W^{+}$) without specifying the atomic number Z. There, A represents the mass number and E the chemical symbol. For single charged ions, the m/q ratio (with m and q representing the mass and the charge state of the ion) corresponds numerically to the mass of the detected ion .

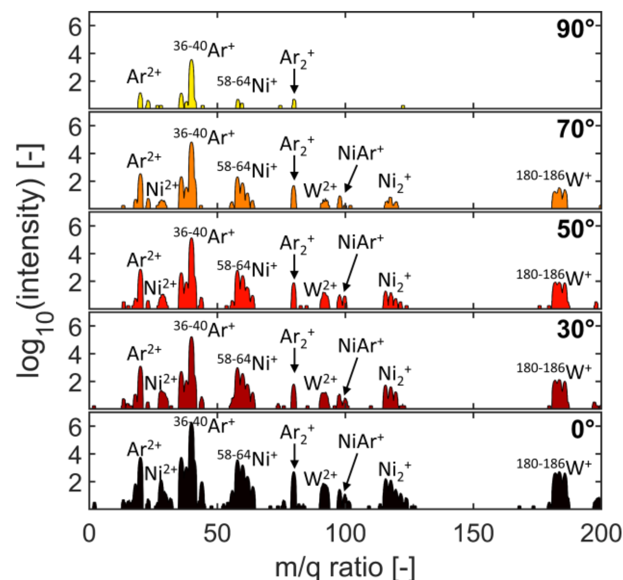

Figure 30: MEA mass-scans conducted at p = 0.09 Pa and a kinetic energy of detected ions E = 2.42 eV at different θ angles (see Figure 29(a) for comparison). Note the decrease in signal intensity with increasing angles.

At θ = 0°, the main fraction of detected ions consists of $^{36}Ar^+$, $^{38}Ar^+$ and $^{40}Ar^+$ at m/q = 36-40. The recorded intensities are consistent with the natural relative abundance of the particular atoms, as summarized in Table 4. It is worth noting that doubly charged Ar^{2+} (m/q = 18-20) as well as Ar_2^+ ion clusters (m/q = 76-80) are present in the plasma with the same amount as $^{36}Ar^+$ and $^{38}Ar^+$, respectively. Besides ionized background gas atoms, various single charged metal ions are detected; $^{58}Ni^+$, $^{60}Ni^+$, $^{61}Ni^+$, $^{62}Ni^+$ and $^{64}Ni^+$ (m/z = 58-64) as well as $^{180}W^+$, $^{182}W^+$, $^{183}W^+$, $^{184}W^+$ and $^{186}W^+$ (m/z = 180-186). The detected intensities agree with the relative abundance of the atoms (Table 4) and the target composition Ni81W19. The similar abundance of the Ni^+ and W^+ ions in the plasma and in the target can be rationalized by the comparable ionization potentials of Ni and W ($E_i(Ni)$ = 7.6 eV, $E_i(W)$ = 7.98 eV [121]). Similar to Ar^{2+} and Ar_2^+, a noticeable amount of doubly charged metal ions Ni^{2+} (m/z = 28-32) and W^{2+} (m/z = 90-93), and Ni_2^+ ion clusters (m/z = 116-128) is present in the plasma. Besides these ions, also small fractions of $NiAr^+$ (m/z = 96-102) ion clusters are detected, which is in good agreement with a work by Hippler *et al.* [122], who identified M-Ar ion clusters (M = Ti, m/z = 88) under comparable conditions.

For θ = 30, 50, 70 and 90° in Figure 30, the recorded spectra are similar to the spectra recorded at θ = 0°, with slightly decreasing intensities. Only spectra recorded at θ > 70° show a vast drop of intensity and are therefore not considered in further discussions.

Table 4: Relative abundance of the natural isotopes of Ar, Ni and W [123].

Ar		Ni		W	
Isotope	**rel. abundance [%]**	**Isotope**	**rel. abundance [%]**	**Isotope**	**rel. abundance [%]**
$^{36}Ar^+$	0.34	$^{58}Ni^+$	68.08	$^{180}W^+$	0.12
$^{38}Ar^+$	0.06	$^{60}Ni^+$	26.22	$^{182}W^+$	26.50
$^{40}Ar^+$	99.60	$^{61}Ni^+$	1.14	$^{183}W^+$	14.31
		$^{62}Ni^+$	3.63	$^{184}W^+$	30.64
		$^{64}Ni^+$	0.93	$^{186}W^+$	28.43

7.3.1.2 Angular resolved energy spectra

Positively charged ions sputtered from the target are not able to leave the sheath region due to the electrical potential, but are accelerated back to the target [9,13]. Therefore, in the current thesis, all detected ions have their origin in inelastic ionization processes of neutral particles in the plasma region. Besides inelastic collisions, atoms and ions will also experience elastic collisions. In every elastic collision, a certain amount of the kinetic energy of the energetic particle is transferred to the slower

collision partner. This energy transfer ε (Equation 1 in section 2.1) and the maximum scattering angle $sin\alpha^{\max} = m_{Ar}/m_M$ [59], stemming from classical mechanics of elastic collisions, with the mass of Ar (m_{Ar} = 39.95 amu) and the mass of the respective metal atom (m_M, namely m_{Ni} = 58.69 amu and m_W = 183.84 amu) will influence the trajectories of the colliding particles. The energy transfer coefficient ε for head-to-head collisions [31], defined in section 2.1, determines the amount of energy that is transferred between two colliding particles. Besides the atomic mass of the collision partners, also the mean free path (λ), defined in section 2.2, with the atomic radii of Ar (r_{Ar} = 71 pm [114]) and the metal atoms (r_M, with r_{Ni} = 125 pm and r_W = 141 pm [121]), corresponding to the average distance a particle can travel between two subsequent collisions, is an important measure [35,124]. The average number of collisions a sputtered particle experiences on its way from the target to the substrate (d) is defined as $N = d/\lambda$. Table 5 gives an overview of λ and N, calculated for the conditions covered within the current thesis with d = 80 mm, corresponding to the target-MEA distance. A gas temperature of 400 K was assumed. It is evident that higher gas pressures lead to more particle collisions and therefore less energetic film growth conditions. Together, N and ε determine the number of collisions needed until an energetic particle is fully thermalized and only possesses the thermal energy of Ar atoms (T_{Ar}) [9].

Table 5: Calculated mean free paths (λ) and average numbers of collisions (N) for the conditions covered within the current thesis with an assumed temperature of 400 K and d = 80 mm, corresponding to the target-MEA distance.

	Ar		**Ni**		**W**	
	λ [mm]	**N [-]**	**λ [mm]**	**N [-]**	**λ [mm]**	**N [-]**
0.09 Pa	685.0	0.1	359.5	0.2	307.3	0.3
0.13 Pa	474.2	0.2	248.9	0.3	212.7	0.4
0.26 Pa	237.1	0.3	124.4	0.6	106.4	0.8
0.43 Pa	143.4	0.6	75.2	1.1	64.3	1.2
0.62 Pa	99.4	0.8	52.2	1.5	44.6	1.8
1.07 Pa	57.6	1.4	30.2	2.6	25.8	3.1

An overview over the ion energy distribution functions (IEDF) recorded for 40Ar+, 58Ni+and 184W+ at different θ angles is shown in Figure 31. 40Ar+ shows the highest intensity, followed by 58Ni+ and 184W+. It has to be noted that due to the Ni81W19 target composition as well as the natural abundance of 184W+ (30.64 %) compared to 58Ni+ (68.08 %) (Table 4), the signal intensity of 184W+ is much smaller compared to 40Ar+ and 58Ni+. For all recorded species, the IEDFs shift to lower

energies with increasing Ar pressure, with the most pronounced decrease from 0.26 to 1.07 Pa. The spectra of 40Ar+ consist of a main peak at E_{peak} = 2.3, 2.4 and 1.8 eV at p = 0.09, 0.26 and 1.07 Pa at θ angles close to the target normal (0 and 10°), as summarized in Table 6. Since the kinetic energy of gas atoms relates to the temperature as $E_k = \frac{3}{2} k_B \cdot T$, the kinetic contribution of thermalized Ar^+ ions to this energy is only 0.05 eV for an assumed deposition temperature of 400 K [49]. Therefore, the $^{40}Ar^+$ peak energy represents the plasma potential at the chosen pressure. Besides the main peak, a high energy tail is visible for all recorded Ar^+ IEDFs. Basically, this high energy tail can have different origins [122]:

(*i*) Sputtered (in this work, Ni and W) atoms, with energy gained from the sputtering process, can transfer part of their energy via elastic collisions to Ar background gas atoms. Ar background gas atoms that have received energy from elastic collisions can be ionized in the plasma and subsequently detected.

(*ii*) A part of the arriving Ar^+ ions is implanted into the target. These implanted ions will be sputtered at a later moment with sputter energies of some ten eVs.

(*iii*) A part of the Ar^+ ions impinging onto the target is neutralized and reflected as Ar neutrals, with energies corresponding up to U_{dc}, under consideration of ε. These reflected neutral Ar atoms may be ionized on their way through the plasma region and detected as Ar^+ ions with high energy.

For small pressures, the peak energies of the IEDFs of the detected metal ions 58Ni+ and 184W+ are slightly higher compared to 40Ar+ (Table 6). This higher peak energies can be explained by not fully thermalized ionized sputtered atoms, which still possess a fraction of their initial energy gained during the sputtering process. A slightly higher peak energy of W compared to Ni can be rationalized by the less efficient energy transfer ε from W to Ar, compared to ε from Ni to Ar (ε(W→Ar) = 0.59, ε(Ni→Ar) = 0.96,). Similarly, the high energy tail of the metal ions is more pronounced at all detected angles and pressures compared to 40Ar+, which can also be attributed to the fact that the sputtered atoms are not fully thermalized. To draw further conclusions, a different style of data representation was chosen, as shown in Figure 32.

Table 6: Peak energies of $^{40}Ar^{+}$, $^{58}Ni^{+}$ and $^{184}W^{+}$ and the θ angles, where the respective spectrum with the peak energy was recorded.

	Ar		Ni		W	
	E_{peak} [eV]	θ	E_{peak} [eV]	θ	E_{peak} [eV]	θ
0.09 Pa	2.3	10	2.9	0	2.9	10
0.26 Pa	2.4	0	2.7	0	3.2	0
1.07 Pa	1.8	0	1.9	0	2.2	0

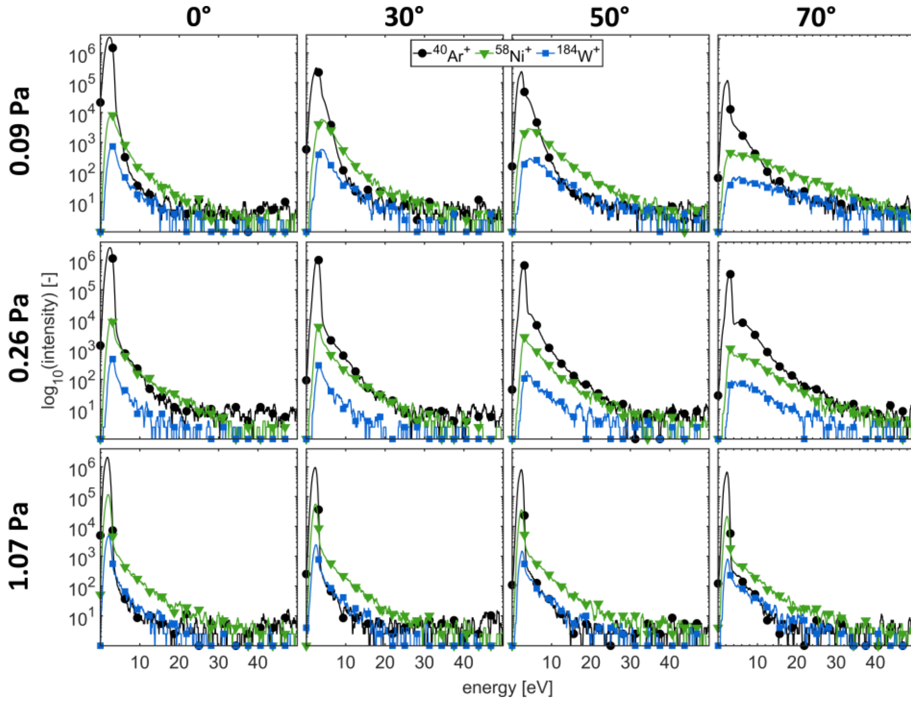

Figure 31: IEDFs of $^{40}Ar^{+}$ (black circles), $^{58}Ni^{+}$ (green triangles) and $^{184}W^{+}$ (blue squares) at p = 0.09, 0.26 and 1.07 Pa at different angles from the target normal (see Figure 29(a) for comparison). For θ > 80°, the intensity of the signal dropped vastly (Figure 30). Therefore, the representation of MEA spectra in the current thesis focusses on θ = 0 – 70°.

A set of 2D contour IEDFs plots of $^{40}Ar^{+}$, $^{58}Ni^{+}$ and $^{184}W^{+}$ at 0.09 Pa is shown in Figure 32. The plots represent IEDFs, as shown in Figure 31, in a single graph, with the x-axis and the contour plot's color-code representing the energy and intensity (logarithmic scale), respectively. The detection probability of either species at a certain angle $P(\theta)$, calculated as a quotient of the total signal intensity at the defined angle $I(E,\theta)$ over the summed total signal intensities of the spectra recorded at all θ from 0 to 90°, defined as

$$P(\theta) = \sum_{E=0}^{50\,eV} I(E,\theta) \Bigg/ \sum_{\theta=0^\circ}^{90^\circ} \sum_{E=0}^{50\,eV} I(E,\theta), \qquad (9)$$

is plotted in Figure 32, represented with white filled squares (left y-axis). $P(\theta)$ is determined by the respective emission, ionization, and transport probabilities of either species.

For $^{40}Ar^+$, low energetic species < 10 eV are predominant for all investigated angles, with the highest abundance for thermalized Ar^+ ions with energies around 2 eV and an energy tail < 30 eV. The population of $^{40}Ar^+$ ions shows a strong preferential distribution along the target normal, which is related to the unbalanced magnetron setup used in the current thesis with open magnetic field lines directing charge carriers towards the MEA [125].

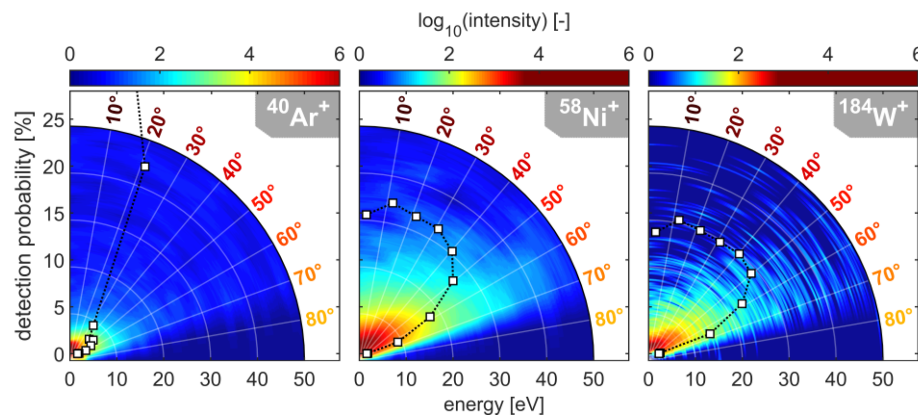

Figure 32: Angular resolved energy plots for $^{40}Ar^+$, $^{58}Ni^+$ and $^{184}W^+$, recorded at 0.09 Pa. The x-axis and the contour plot's color-code represent the energy and intensity (logarithmic scale) of the detected species. The filled white squares connected by a black dashed line (drawn to guide the eye) represent the normalized detection probability $P(\theta)$ of the different species (y-axis). Note that the shown color-code represents the intensity of either species at any θ and energy.

As stated before, all detected metal ions are neutral atoms that were ionized on their way from the target to the MEA. For d.c. magnetron sputtering, electron impact ionization is the dominant ionization mechanism [13]. Considering an average of 0.2 - 0.3 collisions of sputtered metal atoms with Ar atoms on their way from the target to MEA at 0.09 Pa (Table 5), the IEDFs in Figure 32 are considered to represent the initial IEDFs of the sputtered atoms. The detected emission profiles of $^{58}Ni^+$ and $^{184}W^+$ exhibit heart-like shapes (Figure 32), as already observed for various other elements like Cu, W, Ti, Mg, Cr, Zn, Zr and Nb [55,126–129]. Both elements show pronounced high energy tails with energies up to 50 eV. These high energy tails are most pronounced for high angles θ at 60 and 70° and can be explained by Sigmund's linear collision cascade model [51]. During sputtering, Ar^+ ions initiate the formation of collision cascades within the target, where its initial energy is distributed. With the assumption that Ar^+ ions hit the target at an angle θ = 0° [9], the vector of the collision cascade initially points directly into the target. Every collision will change its direction [130]. For the extreme case, in order to sputter a metal atom along the target normal, the vector of the collision cascade has to change

by 180°. Since for a change by 180° more collisions are needed than for 120 or 110° (corresponding to θ = 60 or 70° in Figure 32), it can be expected that atoms sputtered at an angle θ of 60 and 70° will possess more energy from the initial energy of Ar^+ (that initiated the collision cascade), than particles sputtered at smaller θ. Still, according to Sigmund [51], the emission along the target normal is more favorable, since all of the atom's kinetic energy E is available to overcome the surface binding energy E_b. For atoms sputtered at larger θ, their available kinetic energy to overcome E_b reduces to $E\cos^2\theta$ (for details see section 2.1) [9,131]. Therefore, although more particles are emitted at small θ, their energy is much lower compared to particles emitted at large θ.

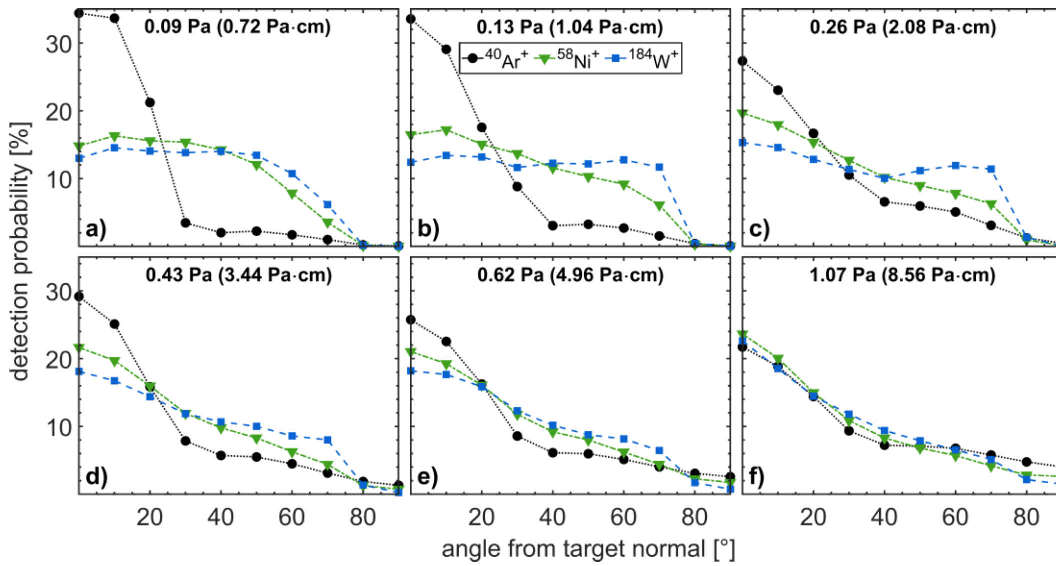

Figure 33: Angular detection probabilities of $^{40}Ar^+$ (black circles), $^{58}Ni^+$ (green triangles) and $^{184}W^+$ (blue squares) at all investigated Ar pressures. The interconnecting lines are only drawn to guide the eye. Note that the shown detection probabilities do not represent absolute, but rather normalized values.

7.3.1.3 Angular resolved detection probability of $^{58}Ni^+$ and $^{184}W^+$

The angular detection probabilities for $^{40}Ar^+$, $^{58}Ni^+$, and $^{184}W^+$ are shown in Figure 33. At p = 0.09 Pa, i.e. a pressure when it can be assumed that the MEA data essentially reflect the initial emission characteristics of Ni and W (as discussed in section 7.3.1.2), the ion fluxes for θ < 40° are Ni rich, whereas ion fluxes for θ > 40° are W rich. Note that the shown detection probabilities do not represent absolute, but rather normalized values. With increasing p, both $P_{Ni}(\theta)$ and $P_W(\theta)$ change their shape due to an increased number of collisions with the background gas atoms (Table 5). It is apparent that the initial emission profile of $^{58}Ni^+$ changes at lower pressures than $^{184}W^+$ does, although the latter possesses a larger atomic radius and a larger collision cross-section than the former. The maximum scattering angle of the sputtered atoms in a collision with an Ar atom is larger for Ni than for W ($\alpha^{\max}$(Ni→Ar) = 43°, $\alpha^{\max}$(W→Ar) = 13°), meaning that W will retain more of its initial angular

distribution. Moreover, the energy transfer coefficient ε in a collision with Ar is larger for Ni than for W (ε(Ni→Ar) = 0.96, ε(W→Ar) = 0.59), meaning that the IEDF of Ni will be more affected by collision with Ar than the IEDF of W. Therefore, the higher atomic mass of W (m_W = 183.84 u) compared to Ni (m_{Ni} = 58.69 u) seems to be the reason that W retains more of its initial angular and energy distribution at higher pressures compared to Ni. The angular distribution profile of $^{58}Ni^+$ already begins to change at p = 0.13 Pa towards its profile at p = 1.07 Pa, whereas only $p \geq$ 0.43 Pa greatly affects the angular distribution profiles of $^{184}W^+$. At $p \geq$ 0.43 Pa, the profiles of both metal species start to converge to the profile of $^{40}Ar^+$. Since all angular distribution profiles are comparable at p = 1.07 Pa, it is evident that all detected particles have undergone enough collisions that their angular distributions are similar to each other.

7.3.2 Angular resolved thin film deposition

7.3.2.1 Thin film deposition

The thickness of the films located at different θ, deposited at p = 0.09, 0.26 and 1.07 Pa, is shown in Figure 34. With increasing θ, the film thickness continuously decreases for all deposition pressures, where films grown at $\theta \geq$ 50° show a sharp drop of the film thickness. It is worth nothing that it is mostly the neutrals, which are responsible for film growth during sputter deposition. The ionized species that where recorded via MEA measurements play only a minor role [9]. For films deposited at angles θ from 0 to 80°, the deposition pressure does not greatly affect the film thickness, as shown in Figure 34. Films grown at θ = 0° have a thickness of 2.85, 2.80 and 2.57 µm for p = 0.09, 0.26 and 1.07 Pa, respectively. The decrease of deposition rate at θ = 0° at the highest pressure is likely the result of an increased number of scattering events of the sputtered atoms. In reverse, it is reasonable to expect that the material that is not deposited at θ = 0° will be redeposited at larger θ. However, since the substrate holder is a spherical shell, the contribution of redeposition per unit area at large θ is small compared to small θ. Therefore, although the deposition rate at θ = 0° and p = 1.07 Pa is lower, the measured deposition rate virtually stays constant at large θ.

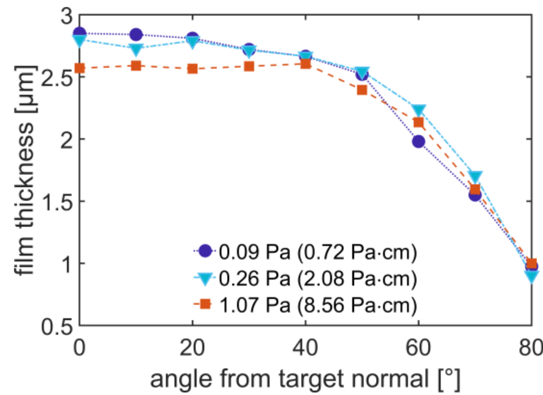

Figure 34: Film thickness of films deposited at different θ angles (Figure 29) at p = 0.09, 0.26 and 1.07 Pa.

7.3.2.2 Film morphology

X-ray diffractograms recorded for films deposited at θ = 0, 40, and 80° at a medium deposition pressure p = 0.26 Pa are shown in Figure 35. The diffractograms indicate that the films are highly textured with a single peak at 43°, attributable to a face-centered cubic (fcc) Ni-rich solid solution $Ni(W)_{ss}$ [132] with fractions of the intermetallic phases NiW and Ni_4W [133]. With increasing θ angle, the peaks are broadening, indicating a decrease in crystallinity and average grain size. This effect can in part be ascribed to the observed increase in W content from 19 to 32 at.% from θ = 0 to 80°. For the composition range covered in the current thesis, Schuh *et al.* [134] and Spolenak *et al.* [133] determined the average grain size of magnetron sputter deposited NiW thin films via transmission electron microscopy to be in the range of 10-20 nm. Moreover, according to reports of Schuh *et al.* [132,134] and Spolenak *et al.* [133], magnetron sputter deposited NiW films with W contents >30 at.% show an amorphous structure, which is in good agreement with the current thesis. Besides the observed peak broadening, the increase in W content from 19 to 21 at.% for films deposited at θ = 0 and 40° leads to a peak shift towards lower diffraction angles (Figure 35). As described in [132–134], this peak shift is due to incorporation of large W atoms into $Ni(W)_{ss}$ that expand the lattice.

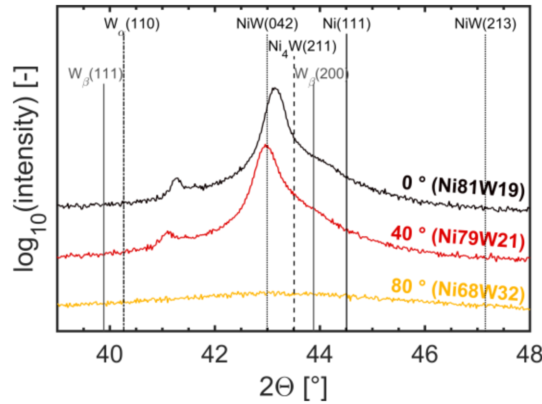

Figure 35: X-ray diffractograms of films deposited at θ = 0, 40 and 80° at p = 0.26 Pa. The designations Ni81W19, Ni79W21 and Ni68W32 represent the elemental sample composition as determined by EDX.

For films deposited at θ = 0, 40 and 80° at 0.26 Pa in the current thesis, the film surfaces and cross-sections (Figure 36) correspond well with the observations of Schuh *et al.* [132,134] and Spolenak *et al.* [133] outlined above. The surface topography investigated by SEM indicates small crystallites for θ = 0 and 40°, with θ = 80° revealing a featureless smooth surface. Both cross-sections of films grown at θ = 0 and 80° reveal dense morphologies without visible columns or grains.

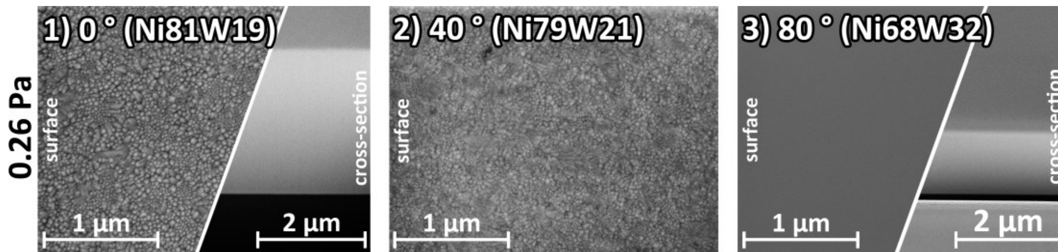

Figure 36: SEM surface and cross-sectional images of films deposited at θ = 0, 40 and 80° at p = 0.26 Pa. The designations Ni81W19, Ni79W21 and Ni68W32 represent the elemental sample composition as determined by EDX.

7.3.3 Correlation of MEA-measurements with thin film growth

The elemental composition of the deposited thin films and the results obtained by MEA measurements are compared in Figure 37. The grey circles in Figure 37 represent the experimentally determined film compositions. All films are Ni-deficient compared to the target composition. Hence, we conclude that a small fraction of sputtered Ni is redeposited on the target surface or deposited on the chamber wall behind the target. With increasing $p \cdot d$, the Ni/W atomic ratio of the films slighly decreases at θ = 0, 30 and 50°, whereas it increases at θ = 70°. We correlate the decrease of Ni at small θ and the enrichment of Ni at large θ with increasing $p \cdot d$ with an increased amount of gas phase scattering of Ni compared to W, as already stated before. The absolute Ni/W atomic ratio of MEA measurements $\tau_{Ni/W}(\theta)$ was calculated as

$$\tau_{Ni/W}(\theta) = \frac{P_{Ni}(\theta)}{P_W(\theta)} \cdot \left(\frac{Ni}{W}\right)_{target}, \qquad (10)$$

with $P_{Ni}(\theta)$ and $P_W(\theta)$ being the detection probability of either species at a certain angle (as defined in section 7.3.1.1), and $\left(\frac{Ni}{W}\right)_{target}$ being the Ni to W atomic ratio in the target. The black, dark red, light red and orange triangles in Figure 37 represent the calculated $\tau_{Ni/W}$. At low θ angles of 0 and 30°, the measured ion flux is Ni-rich based on $\tau_{Ni/W}$, whereas the measured composition of films is slightly Ni-deficient. At θ = 0° and p = 0.13 Pa, $\tau_{Ni/W}$ of 5.8 corresponds to an observed Ni/W ratio in the film of 4.3 (Figure 37). This means that the potentially expected film composition based on the MEA measurements of Ni85W15 becomes experimentally Ni81W19.

In fact, three separate phenomena occuring during film growth cannot be detected by the MEA, namely the influence of (*i*) thermal desorption, (*ii*) the respective sticking coefficients, and (*iii*) any (selective) re-sputtering by reflected Ar neutrals. Consequently, the observed discrepancy between $\tau_{Ni/W}$ and the film composition stems from those three phenomena pointed out above. The contribution of thermal desorption is considered to have only a minor effect on the variation of the film composition with θ (Figure 37), taking into account depositions without external substrate heating and a deposition time of 1 h in combination with a thermally well conducting Al substrate holder. Likewise, only a minor effect of the sticking coefficient is expected, since the substrate temperature is assumed to be constant over all θ. Therefore, the observed discrepancy between $\tau_{Ni/W}$ and the composition of the deposited thin films at θ angles of 0 and 30° (Figure 37) is likely to be dominated by selective re-sputtering of Ni atoms from the growing films by reflected Ar neutrals. With increasing $p \cdot d$, the effect of re-sputtering at θ = 0 and 30° vanishes, so that the calculated $\tau_{Ni/W}$ converge towards the observed Ni/W composition ratios of the films. The smaller difference between $\tau_{Ni/W}$ and the film compositions at higher $p \cdot d$ can be correlated with a higher number of collisions of reflected Ar neutrals with the background Ar gas atoms (Table 5). Every collision lowers the energy of reflected Ar neutrals, and their respective contribution to re-sputtering decreases. For θ of 50 and 70°, $\tau_{Ni/W}$ closer represents the film composition, which means that the influence of re-sputtering is smaller at higher θ angles as compared to 0 and 30°.

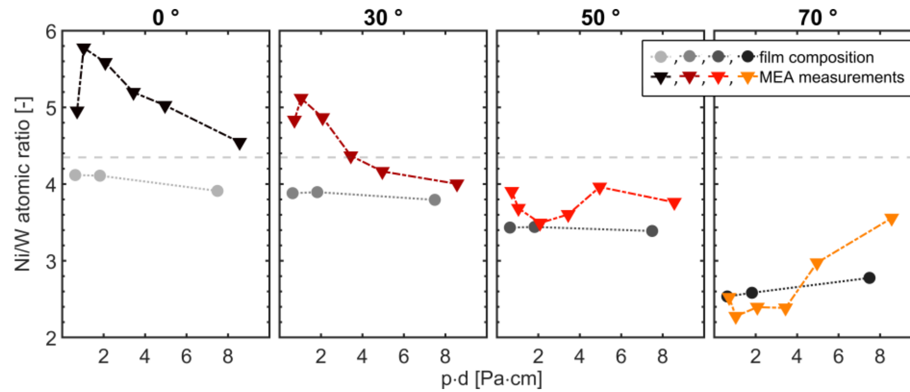

Figure 37: Comparison of $\tau_{Ni/W}$ (labeled as MEA measurements and shown in black, dark red, light red and orange) and the elemental composition of films (in gray) at θ = 0, 30, 50 and 70° at all pressures covered in the current thesis, plotted over the product $p \cdot d$. The elemental composition was determined by EDX and verified by XRF measurements. Interconnecting lines are only drawn to guide the eye. The gray dashed line represents the target Ni/W atomic ratio.

7.4 Conclusions

A circular planar Ni81W19 target was d.c. sputter eroded using an unbalanced magnetron at different Ar pressures. The magnetron was tiltable by +/- 90°, which allowed investigating all ionic species present in the plasma at any angle θ with respect to the target normal. A very low Ar pressure of 0.09 Pa allowed to directly assess the target emission characteristics of the respective elements. There, Ni is emitted at lower angles θ compared to W, with both elements showing pronounced high energy tails at 60-70° from the target normal. As the Ar pressure is increased, the trajectory of Ni is affected earlier than then the trajectory of W, which is due to (*i*) smaller atomic mass and, hence, (*ii*) smaller mean free path, (*iii*) a higher energy transfer coefficient and (*iv*) a higher scattering angle of Ni compared to W in collisions with Ar. The mass-energy analyzer measurements suggest Ni-enrichment of the plasma at low θ with respect to the target normal, and W-enrichment of the plasma at large θ compared to the target composition. In contrast to the expectation, all deposited thin films are Ni-deficient. This discrepancy between the plasma and the thin film composition can be understood by considering selective re-sputtering of Ni from the film surface by energetic reflected Ar neutrals. The current thesis contributes towards understanding of the influence of plasma characteristics on the properties of thin films sputtered from multi-element systems with considerable differences in atomic mass.

Chapter 8 is based on a manuscript in final preparation to be submitted for publication. In the current thesis, all superfluous equations were replaced with references to the main text. Moreover, the figure numbering was adapted to fit to the thesis.

8. Sputter deposition of NiW films from a rotatable target

8.1 Introduction

Magnetron sputtering is widely used for the deposition of thin films for various technological applications like displays or architectural glass [4]. With an increasing demand for films that fulfill special technological needs that can no longer be satisfied by single-element films (for instance in flexible displays [72] or electrochromic windows [6]), the use of multi-element systems is one solution [49]. However, with more elements involved in the deposition process, the complexity of the process itself increases, which presents challenges for the forecasting and for controlling the final film properties. Therefore, sputtering of multi-element systems has been the focus of extensive research over the last years, mostly on laboratory-scale systems (see section 7.1 for a comprehensive review of the studied material systems). These studies focused on three interlinked processes, each influencing the final film properties for itself [9]: (*i*) the emission behavior of particles from the target, (*ii*) the transport of the sputtered particles from target to substrate, and (*iii*) the condensation of these particles on the substrate. The vast amount of studies conducted led to immense progress in the understanding of the complex interplay of those three processes. However, up to now no general guidelines can be drawn that allow forecasting of the final composition and properties of films deposited from multi-element targets, especially when the target constituents have considerable differences in atomic weight, atomic radius and sputter yield. Films are either rich or poor in light and heavy elements compared to the target composition, following no obvious trends [135]. The lack of knowledge is even more pronounced for films grown on an industrial-scale from rectangular or rotatable targets, where – to the best of our knowledge – only two groups have made significant contributions so far. Rueß *et al*. [25] have studied the elemental composition of Cr-Al-C thin films on an industrial-scale as a function of substrate bias potential and substrate temperature, deposited via direct current magnetron sputtering (DCMS) and high power pulsed magnetron sputtering (HPPMS). They found that all films, whether deposited via DCMS or HPPMS, were rich in Cr and deficient in Al and C. Further experiments led to the conclusion that the observed elemental composition of the films is due to selective re-sputtering of Al at room temperature and an increased contribution of selective thermal desorption of Al at elevated temperatures. In previous work [49], we studied the deposition behavior of a Mo70Al20Ti10 rotatable target on an industrial-scale and found that the final film

composition depends on Ar pressure p, target-substrate distance d, and the incident angle of the particle flux from the target onto the surface of the substrates θ. Films grown opposite the target were dense, but Al deficient due to selective re-sputtering of Al. However, films grown at extended distances from the target showed an Al rich open voided structure, attributable to the preferential scattering and thermalization of Al over Mo, influencing film growth. Although those experiments were conducted without substrate carrier oscillation, the implications on dynamic depositions used for industrial applications are evident: with each oscillation, films are either grown in an Al-deficient or an Al-rich particle flux, leading to cross-sectional variations of density and composition of the films.

To widen the existing knowledge on sputter deposition from multi-element targets, the current thesis focuses on the sputter deposition of thin films grown from a Ni80W20 rotatable target on an industrial-scale. Ni and W display large differences with respect to atomic weight, atomic radius and sputter yield. Therefore, the chosen system represents an ideal model for a systematic investigation of the mechanisms leading to compositional differences between target and films.

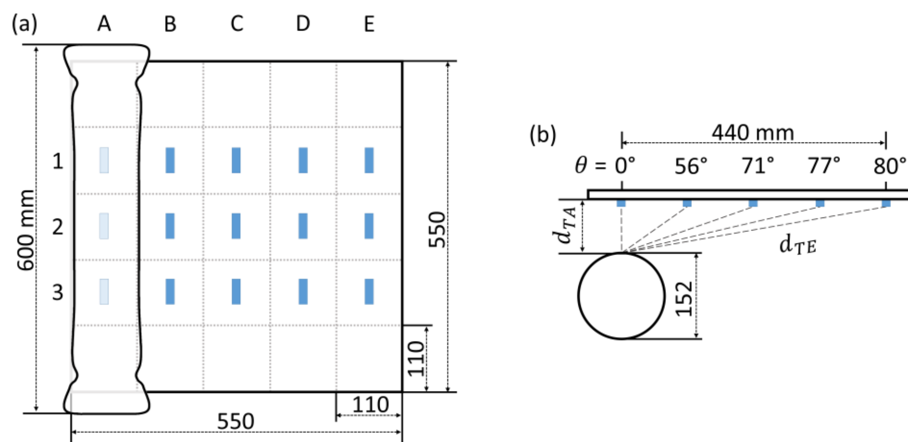

Figure 38: Schematic representation of (a) the 5 × 3 matrix of Si (100) substrates used for thin film deposition, arranged in three rows (1-3) and five columns (A-E). This designation allows to directly identify each sample, for instance 2A as the central sample opposite the target. (b) Illustrates the top view of the used setup. The distance d_{TA} corresponds to the target-substrate distance of 75 mm, whereas d_{TE} corresponds to the distance from the target to column E, which is 446 mm. θ represents the incident angle of the particle flux from the target onto the surface of the substrates, but also the emission angle from the target with respect to d_{TA}.

8.2 Experimental details

8.2.1 Thin film deposition

A rotatable Ni80W20 target with the dimension Ø 152 × 600 mm (manufactured by cold-gas-spraying [107–110], provided by Plansee SE) was mounted in an industrial-scale in-line magnetron sputter system (FHR Line.600V). A series of thin films was deposited on a 5 × 3 matrix of (100) Si substrates at equidistant positions, each 110 mm apart (Figure 38). Prior to mounting on the grounded

550 × 550 mm² substrate carrier with Kapton tape, the used (100) Si substrates (21 × 7 mm², thickness 325 µm) were ultrasonically cleaned in ethanol for 10 min. The base pressure of the chamber before each deposition run was below $1{\times}10^{-5}$ Pa. Before each deposition, a preliminary etching step was carried out for further substrate cleaning and surface activation. Only for that etching step, the substrate carrier oscillated 12 times in front of a radio-frequency (r.f.) source, which was powered by an r.f. power supply at 13.56 MHz (Advanced Energy Cesar 1310) and a discharge power of 0.8 kW. The velocity of the substrate carrier was 20 mm/s during the etching step. The Ar pressure p during etching was 0.32 Pa. Film depositions were carried out at Ar pressures p of 0.25, 0.42, 0.70 and 1.00 Pa, corresponding to gas flows of 150, 300, 500 and 750 sccm, respectively. The target was powered by a direct current (d.c.) power supply (Advanced Energy Pinnacle 20 kW) that was held at a constant current of 10 A (current-controlled mode) for 30 min. The resulting target voltages (U_{dc}), currents (I_{dc}) and the resulting sputter powers (P_{dc}) are listed in Table 7. No additional heating was applied. The substrates of column A were positioned exactly opposite the target, corresponding to an offset of 220 mm from the target axis of the grounded substrate carrier (see Figure 38). The target-carrier distance d_{TA} was constant at 75 mm.

Table 7: Target voltage U_{dc} and current I_{dc} for the depositions performed at different Ar pressures p.

p [Pa]	U_{dc} [V]	I_{dc} [A]	P_{dc} [kW]
0.25	427 ± 0.8	10	4.27
0.42	399 ± 0.9	10	3.99
0.70	388 ± 0.8	10	3.88
1.00	384 ± 0.8	10	3.84

8.2.2 Thin film and target characterization

White light optical profilometry (Veeco Wyko NT1000) with Vision64 software package was used to assess the film thickness. Deposition rates were calculated as film thickness over time, neglecting eventual changes in film density. The elemental composition of the films was determined via energy dispersive X-ray spectroscopy (EDX, Oxford Instruments INCA) with built-in sensitivity factors. The results obtained were cross-calibrated using X-ray fluorescence spectroscopy (XRF, Thermo Scientific ARL 8410) on selected samples. The microstructure of the films was investigated with X-ray diffraction (XRD, Bruker-AXS D8 Advance) in $\Theta/2\Theta$ geometry, using a Cu-K_{α} X-ray source and parallel beam optics. To avoid excessive (100) Si reflections, the measurements were performed in unlocked-coupled mode, with X-ray tube and detector tilted by 1 ° from the surface normal. The samples were constantly

rotated during the measurements. The surface of the films was investigated with scanning electron microscopy (SEM, Zeiss Evo 50) using an Everhart-Thornley secondary electron (SE) detector for surface imaging and a backscattered electron (BSE) detector for enhanced element contrast. Cross-sections of the films were prepared and investigated by focused ion beam milling (FIB, Zeiss Leo 1540 XB) with stepwise reduced ion currents down to 100 pA.

To correlate target morphology with film properties, a laboratory-scale 90 mm circular cold-gas-sprayed Ni81W19 target (also provided by Plansee SE) was d.c. sputter eroded in 1.07 Pa Ar at 1.57 W/cm² for 1 h. The eroded target surface was investigated by SEM (FEI 3D Versa). Focused ion beam milling (FEI 3D Versa) with stepwise reduced ion currents down to 7 nA was used to directly associate areas of interest on the target surface with local cross-sections. Confocal laser scanning microscopy (CLSM, Olympus LEXT OLS4100) was used to assess the surface roughness of the target.

8.2.3 Simulation

The SRIM software package (The Scattering and Range of Ions in Matter, [74]) was used to investigate the sputtering of heavy W and light Ni atoms, in particular the sputter yield amplification effect (SYA), as studied for Al on W [136]. Therefore, a Ni top-layer with a thickness t_{Ni} = 1-20 Å atop a 100 Å thick W under-layer was bombarded with 10,000 Ar^+ ions at energies between E_{Ar} = 200-600 eV perpendicular to the target surface. Since single charged Ar^+ ions are the predominant species responsible for sputtering, E_{Ar} is directly linked to the applied target voltage U_{dc}. The resulting Ni sputter yields (Y) at each E_{Ar} and t_{Ni} were compared to the respective number of Ar^+ ions used for the simulations as

$$Y_{partial} = \frac{Y}{10{,}000}, \qquad (11)$$

yielding the respective partial sputter yield $Y_{partial}$. This approach allowed to investigate the influence of the applied target voltage on the preferential emission of Ni in close proximity to W.

8.3 Results

8.3.1 Thin film deposition

Four series of NiW thin films were deposited at Ar pressures p ranging from 0.25 to 1.00 Pa. The used arrangement of five columns of substrates at different distances from the target center, shown in Figure 38, allows to systematically study the influence of Ar pressure p, target-substrate distance d and particle incident angle θ on deposition rate R as well as microstructure and elemental composition of the films. The used arrangement of three rows of substrates adds statistical significance to the results.

Figure 39 represents the deposition rates for films grown at different positions A-E on the substrate carrier (Figure 38) with respect to $p \cdot d$. Films grown in column A show a pressure dependent deposition rate R due to a drop of P_{dc} with increasing pressure p (Table 7), while R for columns B-E stays relatively constant over the pressure range investigated. The lateral position on the substrate carrier from column A to E, which influences the target-substrate distance d and the particle incident angle θ (Figure 38), has a strong impact on R. With increasing distances from the target center, the deposition rate decreases. Films in column A are grown with the highest observed deposition rates of 250-280 nm/h, whereas films deposited onto substrates in columns D and E show the lowest deposition rates of < 5 nm/min.

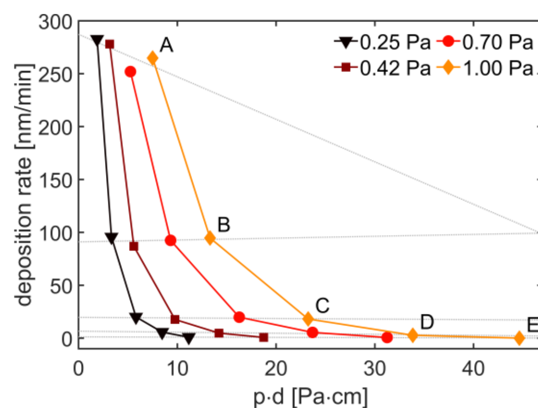

Figure 39: Average deposition rates of samples deposited at different distances from the target center (columns A-E, Figure 38) and at different Ar pressures between 0.25 and 1.00 Pa. Note that the calculated standard deviation of the thickness of films grown in row 1-3 is smaller than the size of the markers. Therefore no error bars are shown.

Figure 40 gives an overview of the elemental composition of films grown at different lateral positions on the substrate carrier at Ar pressures from 0.25 to 1.00 Pa. Due to the limited deposition rate and thickness of films grown in columns D and E, that do not allow reliable EDX and XRF measurements, only data for positions A-C are presented. From Figure 40 it is evident that both Ar pressure and lateral

position on the substrate carrier influence the Ni/W ratio in the films. The Ar pressure affects the difference in elemental composition between films grown in column A to C, with increasing p equalizing the Ni/W ratios and reducing the difference between samples grown opposite the target (column A) and at extended distances from the target center (column C, Figure 38). For films grown in column A, the Ni/W ratio decreases with increasing Ar pressure p from 0.25 over 0.42 to 0.70 Pa, and then increases again when p = 1.00 Pa. In columns B and C, the ratio only decreases for p = 0.25 to 0.42 Pa, in order to rise again when $p \geq$ 0.70 Pa.

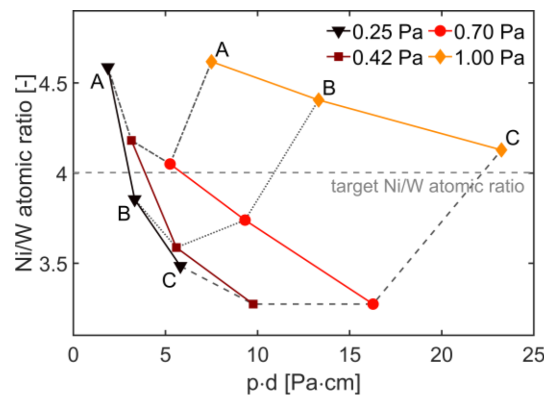

Figure 40: Elemental composition of films grown at different distances from the target center (columns A-C, Figure 38) and at different Ar pressures between 0.25 and 1.00 Pa.

X-ray diffraction revealed that all films are highly textured, showing a single peak at ~43 °, attributable to a face-centered cubic (fcc) Ni-rich solid solution $Ni(W)_{ss}$ [132]. The growing fraction of W in the films (see Figure 40) with p increasing from 0.25 to 0.70 Pa and d from column A to C leads to a peak shift towards lower diffraction angles and decreased peak height. This peak shift is attributed to the incorporation of large W atoms expanding the lattice of $Ni(W)_{ss}$, being in good agreement with work published by Schuh *et al*. [132,134] and Spolenak *et al*. [133].

Figure 41(a) gives an overview of SEM images of the surface of films deposited at different lateral positions on the substrate carrier (Figure 38) at p = 0.25 and 1.00 Pa. In addition, Figure 41(b) shows the respective cross-sections of these films, as derived by focused ion beam milling. With increasing distance from the target center, i.e. from sample 2A to 2C, the surface roughness and the size of the surface features decreases. Films grown close to the target center appear dense (Figure 41(b), samples 2A and 2B), whereas films grown at extended distances from the target center in column C show an open voided morphology (Figure 41(b), sample 2C). Compared to p = 1.00 Pa, an Ar pressure of 0.25 Pa leads to films with increased intercolumnar spacing and surface roughness. The growth direction of

the columns depends on the particle incident angle θ and Ar pressure p, with lower p increasing the inclination of the grains towards the target (Figure 41(b) 2C).

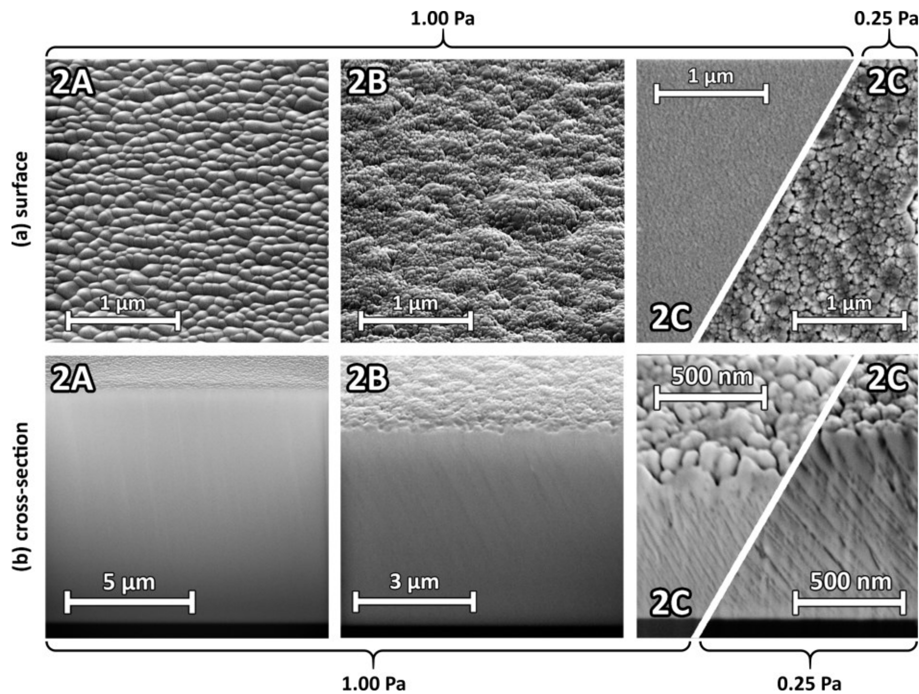

Figure 41: (a) SEM surface micrographs and (b) focused ion beam cross-sections of films grown at different lateral positions 2A to 2C at p = 1.00 Pa and 0.25 Pa.

8.3.2 Target characterization

Figure 42(a) shows SEM micrographs of the surface of the as received target recorded with a BSE detector, with Ni appearing dark and W light gray. The visible slight grinding marks stem from target manufacturing. Figure 42(b+c) display the target surface after sputter erosion at p = 1.07 Pa and a current density of 1.57 W/cm² for 1 h, resulting in a rough surface topography. Figure 42(b) shows a micrograph recorded with an SE detector (left side) and a BSE detector (right side). For both cases, a terrace-like morphology of Ni is evident, whereas W mostly reveals a platelet-like structure. Figure 42(c+d) represent SE micrographs of the target surface tilted by 52 °, indicating the height of the structures to be in the range of some 10 µm. CLSM revealed the maximum profile valley depth of the roughness profile R_v in the erosion zone to be 14.0 ± 1.1 µm, whereas it was 9.7 ± 0.7 µm in the not eroded area. Figure 42(d) shows a FIB prepared cross-section of the area marked with a white dashed rectangle in Figure 42(c), revealing light gray W particles embedded in a dark gray Ni matrix with different thickness.

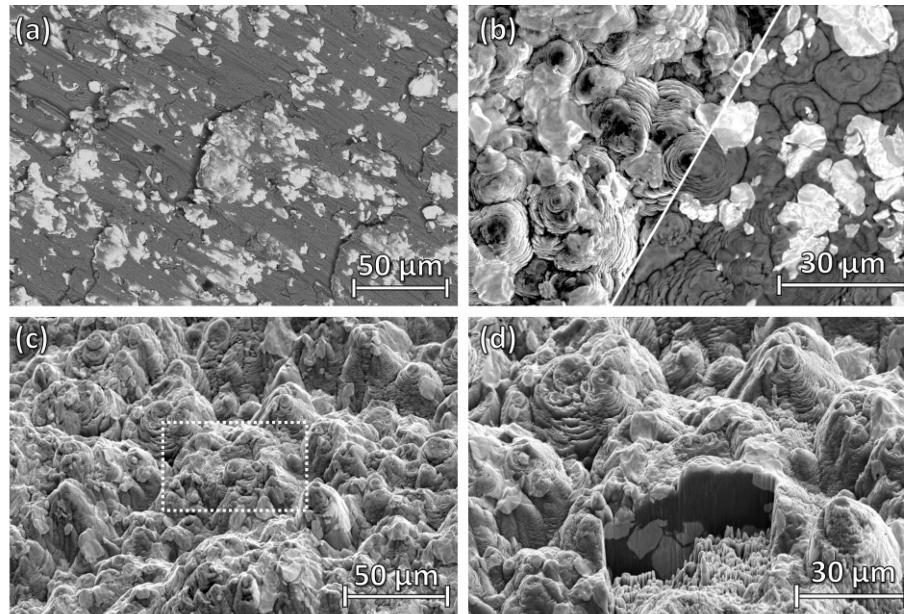

Figure 42: SEM images of (a) the surface of the as received target and (b+c) the target surface after sputter erosion. (d) represents a FIB cut of the area marked in (c) with a white dotted rectangle. All images were recorded in the central area of the erosion track.

8.3.3 Simulation

Static SRIM simulations were carried out to assess the partial sputter yield of a Ni top-layer ($Y_{partial}$) on a W under-layer with varying Ni layer thickness t_{Ni} and Ar^+ ion energy E_{Ar}. The resulting partial sputter yields of Ni are summarized in Figure 43. $Y_{partial}$ clearly depends on the Ar^+ ion energy and increases with rising E_{Ar}. For increasing E_{Ar} the maximum of $Y_{partial}$ moves towards higher top-layer thickness of Ni. Depending on E_{Ar}, for $t_{Ni} \gtrsim 10$ Å, the partial sputter yield of Ni corresponds to the sputter yield of bulk Ni. Figure 43 clearly indicates the existence of a sputter yield amplification effect for the studied system Ni/W.

8.4 Discussion

Films grown from multi-element targets rarely represent the initial target composition [25]. Although studied extensively on laboratory-scale systems [135], up to now no general rules exist allowing to predict the final properties of films deposited from multi-element systems that have not been studied before. This holds especially true when two or more target constituents have large differences in atomic radius, weight and sputter yield. Therefore, the system Ni80W20 in the current thesis represents an ideal model to shed further light onto the complex interplay of processes (*i*) on the target surface, (*ii*) during the transport of particles from target to substrate, and (*iii*) on the substrate surface, each influencing final film properties. The combination of target erosion studied on a laboratory-scale

with film deposition in an industrial-scale in-line sputter system allows discussing above processes separately.

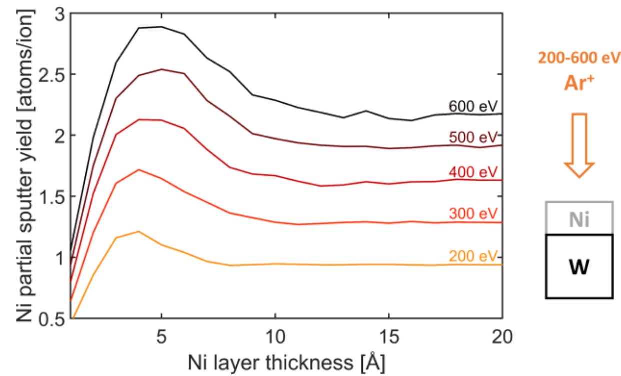

Figure 43: SRIM simulation results of the partial sputter yield of Ni. A Ni top-layer with varying thickness of 1 - 20 Å on top of a 100 Å W under-layer was bombarded with Ar^{+} ions at energies ranging from 200 to 600 eV. The respective partial sputter yield of Ni atoms per incident Ar^{+} ion was evaluated.

When sputter eroding a multi-element target, the sputter process leads to an increase of target surface roughness [50]. This increase is evident from the presented roughness measurements of the target surface, where the maximum valley depth of the roughness profile R_v in the erosion zone was 14.0 ± 1.1 µm compared to 9.7 ± 0.7 µm in the not eroded area. This increase originates from the combination of elements with high and low sputter yields within a single target (Y_{Ni} = 0.95, Y_W = 0.40, both for normal incidence Ar^{+} with energies of 300 eV [118]). Consequently, W with its low sputter yield protects Ni with its high sputter yield, whereas unprotected areas of Ni will efficiently be sputter eroded. The combination of elements with high and low sputter yields in a single target leads to the formation of cones on the target surface and an increase of R_v, as observed in earlier studies [9,50]. According to Boydens *et al.* [55], this rise of surface roughness leads to two competing effects: Firstly, due to the topography of a rough surface with valleys and hills, Ar^{+} ions locally hit the target surface under oblique angles, increasing the sputter yield [9]. Secondly, that morphology will increase the amount of re-deposition of sputtered particles onto the target surface, decreasing the sputter yield. For microscopically rough multi-element targets this implies that re-deposition of atoms can either occur on similar or dissimilar atomic surfaces. For the system Ni80W20 in the current thesis, the latter leads to an increase of surface roughness when W is re-deposited on Ni, whereas it causes a local sputter yield amplification effect when Ni is re-deposited on W (Figure 43). However, an increase of surface roughness not solely changes the sputter yields of different elements, but also influences their emission angles. The preferential emission angle follows a cosine-like distribution for atomically flat surfaces, whereas it shows a heart-like distribution for rough target surfaces [55]. This finding was

validated in our previous work [135] where we conducted angular resolved mass-energy analyzer (MEA) measurements for the system Ni81W19. We showed that the preferential emission angles of both Ni and W follow a heart-like distribution, with W being preferentially emitted at larger angles from the target normal (θ) compared to Ni.

Following this notion, the decrease of the Ni/W atomic ratio from column A to C at constant Ar pressure p in the current thesis (Figure 40) has to be related to the preferential emission angles of Ni and W from the target surface. Ni is enriched opposite the target, corresponding to low θ, whereas W is enriched at extended distances from the target center, corresponding to large θ. The observed trends of the Ni/W atomic ratio in dependence of $p \cdot d$ - no matter their lateral position - can be explained by the three deposition-pressure-determined regimes for particle transport through the gas described by Rossnagel [29]. Rossnagel distinguished (*i*) a ballistic, (*ii*) an intermediate and (*iii*) a diffusive regime when sputter depositing multi-element systems. Rossnagel's considerations are based on the atomic weight of the respective species and scatter events with background gas atoms that affect their trajectories differently. The ballistic regime is characterized by lacking collisions of sputtered atoms with background gas atoms, while solely the trajectories of the light atoms are influenced in the intermediate regime. The diffusive regime is fully diffusion controlled, no matter the atomic weight of the involved atoms. For the current thesis, this means that films deposited at p = 0.25, 0.42 and 0.70 Pa are either grown in a ballistic (0.25 Pa) or an intermediate regime (0.42 and 0.70 Pa), whereas films deposited at p = 1.00 Pa are grown in a diffusive regime. The Rossnagel model agrees well with our earlier reported findings on thin films sputtered from a planar Ni81W19 target [135], where we found Ni to be influenced by background gas scattering before W.

All films deposited in column A are generally Ni-rich compared to the target composition (Figure 40). However, with p increasing from 0.25 to 0.70 Pa, films grown in column A experience a Ni loss. With the observed decrease of U_{dc} (Table 7), a decrease of E_{Ar} goes along [9] lowering the partial sputter yield of Ni, as visible from SRIM simulations conducted in the current thesis (Figure 43). Therefore, the Ni/W atomic ratio of films grown in column A is also expected to decrease, as corroborated for the pressures up to ≤ 0.70 Pa. At p = 1.00 Pa the Ni/W atomic ratio increases again, which intuitively contradicts this notion. It has to be noted that with increasing p also the deposition rate R decreases (Figure 39) and, according to Rossnagel [29] and our own findings [135], not only Ni is affected by gas scattering, but also W. This means that not only the overall flux of particles towards the substrate decreases with increasing p, but also that its composition changes towards higher Ni/W atomic ratios.

Therefore, the observed increase of the Ni/W atomic ratio at p = 1.00 Pa seems to be reasonable and correlates well with Rossnagel's model [29].

It is worth noting that for the current system Ni80W20 the differences in elemental composition with respect to the lateral position on the substrate carrier and p are not as pronounced as for the system Mo70Al20Ti10, studied before in the same deposition chamber [49]. We attribute the observed differences to the atomic mass of the involved species with respect to the background gas ($m_{Al} = 26.98$ u, m_{Ar} = 39.95 u, $m_{Ti} = 47.87$ u, $m_{Mo} = 95.95$ u). Since $m_{Al} < m_{Ar}$, Al is scattered much more effectively than Mo and Ti, leading to a scatter-dominated deposition behavior of MoAlTi. Within the current thesis, both the atomic masses of Ni m_{Ni} and W m_W are greater than m_{Ar}. Therefore, the influence of scattering of Ni and W during the transport through the gas is small compared to the differences of preferential emission angles of Ni and W, leading to an emission-dominated deposition behavior of NiW films.

The observed decrease of U_{dc} (with a concomitant decrease of P_{dc}, Table 7) with increasing p (Figure 39) inherently lowers the deposition rate R in column A. In contrast to column A, columns B-E show constant R with increasing Ar pressure. Sputtered particles experience more collisions with Ar background gas atoms during their transport through the gas when travelling from the target towards columns B-E, since the target-substrate distance for columns B-E is larger than for column A. Background gas scattering influences the trajectories of sputtered particles and directs them towards columns B-E. The higher number of scatter events with increasing p counterbalances the decrease of R in columns B-E (as observed in column A), keeping R on a constant level. However, with every scatter event the involved particles lose parts of their energy. When particles with low energies hit the substrate, their respective adatom mobility is low, so that they cannot move to already existing grains [8]. This, in combination with low substrates temperatures in column C, i.e. at extended distances from the target, leads to open voided film morphologies (Figure 41(b)). In contrast, films grown in columns A and B are dense, since the arriving particles have conserved high energies during the transport through the gas. Moreover, the substrate temperature of films grown in column A and B is much larger than in column C [7,89], further promoting the growth of dense films [8]. In addition it is evident that the trajectories of sputtered particles are less significantly affected at low p compared to high p. Films grown in column C at p = 0.25 Pa are formed by grains more strongly inclined towards the target center compared to those grown at p = 1.00 Pa (Figure 41(b)), since the particle flux at p = 0.25 Pa is more ballistic than at p = 1.00 Pa [49].

The findings presented within the current thesis clearly demonstrate the complex interplay of various parameters (target composition, target surface morphology, deposition pressure, and target-substrate distance) on the properties of films grown from a multi-element target. The chosen arrangement of (100) Si substrates in a 5 × 3 matrix revealed that especially the lateral distance of the substrate from the target center influences the growth of thin films, affecting elemental composition and microstructure. However, that effect has strong implications on dynamic depositions performed on an industrial-scale, when the substrates carrier oscillates in front of the target: films that simultaneously are grown in column A or E (Figure 38), for instance during large-area depositions, experience completely different growth conditions. Of course, the growth conditions in column A and E reverse when the substrate carrier moves towards the other vertex of the oscillation (in our case from the position depicted in Figure 38 at 440 mm to the left). However, this change of film growth conditions over deposition time inherently leads to an alternating gradient of film properties over film thickness, ultimately changing the overall film properties.

8.5 Conclusions

NiW thin films were sputter deposited from a rotatable Ni80W20 target on a set of (100) Si substrates arranged in a 5 × 3 matrix, covering the whole substrate carrier. Since films were deposited without substrate carrier movement, this approach allowed to study the lateral differences in growth conditions and film properties. The lateral position on the substrate carrier governs deposition rate, elemental composition and microstructure of the films, which was attributed to (*i*) the respective emission profiles of Ni and W, and (*ii*) scatter events of sputtered particles during their transport through the gas. Not only the lateral position, but also an increasing Ar pressure affects film properties due to the increased number of scatter events. Consequently, an increase in Ar pressure up to p = 0.70 Pa results in smaller Ni contents of the films, which is related to the more efficient scattering of Ni compared to W. In contrast, films grown at p = 1.00 Pa are Ni-rich. At this pressure, scatter events not only affect the trajectories of Ni, but also those of W, which reduces the flux of W particles arriving at the film surface. Microscopic investigations of the target surface revealed a high roughness, stemming from the interplay between the high and low sputter yield elements Ni and W. W sputtered on top of Ni contributes to an increase in surface roughness of the target, whereas Ni sputtered in the close proximity of W leads to a sputter yield amplification effect. Optimization of Ni and W grain size could therefore allow to selectively strengthen or lower the respective effect.

In conclusion, the observed changes of film properties with respect to the lateral position of the substrates on the carrier have strong implications on films grown via dynamic depositions, i.e. with an

oscillating substrate carrier. The use of multiple magnetrons and a proper adjustment of substrate carrier movement with respect to the magnetrons will help to avoid alternating gradients of film properties over film thickness, which may affect the overall film performance.

9. CONCLUSIONS AND OUTLOOK

Magnetron sputter deposited thin films show a wide variety of applications. In particular, Mo-based films are used in displays and microelectronics, whereas NiW-based electrochromic films are used for architectural glass. Nonetheless, from a scientific point of view there are still various questions to be answered, especially concerning the process-stability and deposition behavior of different coating systems on an industrial-scale. Therefore, one of the aims of the current thesis is adding substantial knowledge to the process stability of a planar industrial-scale Mo target. A systematic study of the influence of the depth of the target erosion groove on film properties revealed a non-linear evolution of film properties over target usage. The changes in film quality were attributed to the varying influence of reflected Ar neutrals to the overall energy input into the growing film. Ar atoms that are reflected from a new, uneroded target surface contribute to a large energy input into the growing film. With the evolution of an erosion groove, the reflecting angle of the Ar neutrals changes, which results in a decreasing energy input into the growing film. When the target erosion proceeds, the target surface gets closer to the magnet bars behind the target, leading to an increase of charge carriers in the plasma and a rise in deposition current. Therefore, a larger amount of Ar^+ ions bombard the target, with a concomitant larger amount of Ar neutrals reflected from the target surface. This increases the energy input into the growing film again, revealing the importance of reflected Ar neutrals on film growth. Similar conclusions were drawn from the systematic study of the deposition behavior of MoAlTi and NiW films from rotatable targets on an industrial scale. In both cases, reflected Ar neutrals were identified as main source of selective re-sputtering of the film constituent with higher sputter yield. Since the amount of selective re-sputtering is pressure-dependent, changing the Ar pressure allows controlling the elemental composition of films grown from multi-element targets to a certain degree. However, the two studied multi-element systems MoAlTi and NiW showed an opposite trend concerning lateral elemental distribution, with “light” Al being depleted and “light” Ni being enriched opposite the target center. Mass-energy analyzer measurements and Monte-Carlo simulations led to the conclusion that during magnetron sputtering of multi-element targets two atomic-mass depended mechanisms exist, namely a scatter-dominated and an emission-dominated regime. When the mass of the target element is smaller than the mass of the background gas, the sputtered elements tend to be predominantly scattered. This leads to a depletion of the light element opposite the target center. On the contrary, when the mass of the target element is larger than the mass of the background gas, the emission characteristics of the sputtered elements are conserved throughout the deposition process.

This leads to an enrichment of that element opposite the target that is preferentially emitted close to the target normal.

To conclude, the current thesis underlines the importance of reflected Ar neutrals on the growth of both single-element and multi-element thin films. Not only microstructure and accompanying film properties like stress and electrical resistivity, but also the elemental composition can be influenced by this high-energetic particle bombardment. The findings reported within this thesis can therefore contribute to a wider understanding and improved process control of sputter processes in industry and academia. Further experiments need to be conducted to prove the hypothesis about the existence of a scatter-dominated and an emission-dominated regime for sputter deposition of multi-elemental films. To do so, a simplified binary system of a light and heavy element with varying composition has to be systematically studied, using a combinatorial approach of mass-energy analyzer and film growth experiments. Ideally, the films should not exhibit any intermetallic phases, but rather form a solid solution to facilitate analysis.

REFERENCES

[1] J.E. Greene, Applied Physics Reviews 1 (2014) 41302.

[2] O. Vittori, Endeavour 3 (1979) 128–131.

[3] H. Lechtman, Scientific American 250 (1984) 56–63.

[4] J.E. Greene, Journal of Vacuum Science & Technology A: Vacuum, Surfaces, and Films 35 (2017) 05C204.

[5] M. Ohring, Materials science of thin films: Deposition and structure, 2nd ed., Academic Press, San Diego, Calif., 2002.

[6] C.G. Granqvist, SPIE Newsroom (2006) 2–4.

[7] T. Jörg, M.J. Cordill, R. Franz, O. Glushko, J. Winkler, C. Mitterer, Thin Solid Films 606 (2016) 45–50.

[8] I. Petrov, P.B. Barna, L. Hultman, J.E. Greene, Journal of Vacuum Science & Technology A: Vacuum, Surfaces, and Films 21 (2003) S117-S128.

[9] W. Westwood, Sputter deposition, 1st ed., AVS Education Committee, New York, 2003.

[10] D.M. Mattox, Handbook of physical vapor deposition (PVD) processing, 2nd ed., William Andrew, Oxford, UK, 2010.

[11] R.A. Powell, S.M. Rossnagel, PVD for Microelectronics: Sputter Deposition applied to Semiconductor Manufacturing, 26th ed., Academic Press, San Diego, 1999.

[12] W.D. Sproul, Surface and Coatings Technology 49 (1991) 284-289.

[13] P.M. Martin, Handbook of deposition technologies for films and coatings, 3rd ed., Elsevier, Amsterdam, Boston, 2010.

[14] A.M. Hofer-Roblyek, K.-H. Pichler, C. Linke, R. Franz, J. Winkler, C. Mitterer, Surface and Coatings Technology 352 (2018) 354–359.

[15] J.A. Thornton, Journal of Vacuum Science and Technology 15 (1978) 171–177.

[16] J.A. Thornton, Thin Solid Films 54 (1978) 23–31.

[17] T. Fukami, F. Shintani, M. Naoe, Thin Solid Films 151 (1987) 373–381.

[18] S. Swann, Journal of Vacuum Science & Technology A: Vacuum, Surfaces, and Films 5 (1987) 1750–1754.

[19] S. Swann, Vacuum 38 (1988) 791–794.

[20] J.F. Whitacre, W.C. West, B.V. Ratnakumar, Journal of Power Sources 103 (2001) 134–139.

[21] E. Shidoji, M. Nemoto, T. Nomura, Y. Yoshikawa, Electrochemical and Solid-State Letters 33 (1994) 4281–4284.

[22] E. Shidoji, M. Nemoto, T. Nomura, Journal of Vacuum Science & Technology A: Vacuum, Surfaces, and Films 18 (2000) 2858–2863.

[23] Q.H. Fan, L.Q. Zhou, J.J. Gracio, Journal of Physics D: Applied Physics 36 (2003) 244–251.

[24] M. Rausch, M. Golizadeh, P. Kreiml, M.J. Cordill, J. Winkler, C. Mitterer in final preparation.

[25] H. Rueß, M. to Baben, S. Mráz, L. Shang, P. Polcik, S. Kolozsvári, M. Hans, D. Primetzhofer, J.M. Schneider, Vacuum 145 (2017) 285–289.

[26] P. Eklund, M. Beckers, U. Jansson, H. Högberg, L. Hultman, Thin Solid Films 518 (2010) 1851–1878.

[27] J.-O. Achenbach, S. Mráz, D. Primetzhofer, J. Schneider, Coatings 9 (2019) 206.

[28] Y. Murakami, T. Shingyoji, Journal of Vacuum Science & Technology A: Vacuum, Surfaces, and Films 8 (1989) 851–854.

[29] S.M. Rossnagel, I. Yang, J.J. Cuomo, Thin Solid Films 199 (1990) 59–69.

[30] T. Yamazaki, N. Ikeda, H. Tawara, M. Sato, Thin Solid Films 235 (1993) 71–75.

[31] C. Mitterer, Journal of Solid State Chemistry 133 (1997) 279–291.

[32] M.Y. Liao, Y. Gotoh, H. Tsuji, J. Ishikawa, Journal of Vacuum Science & Technology B: Microelectronics and Nanometer Structures 22 (2004) L24-L27.

[33] C. Walter, C. Martinez, T. El-Raghy, J.M. Schneider, T. Ei-ragh, steel research international 76 (2005) 225–228.

[34] P. Eklund, M. Beckers, J. Frodelius, H. Högberg, L. Hultman, Journal of Vacuum Science & Technology A: Vacuum, Surfaces, and Films 25 (2007) 1381–1388.

[35] J. Neidhardt, S. Mráz, J.M. Schneider, E. Strub, W. Bohne, B. Liedke, W. Möller, C. Mitterer, Journal of Applied Physics 104 (2008) 63304.

[36] Y. Jiang, S. Mráz, J.M. Schneider, Thin Solid Films 538 (2013) 1–6.

[37] S. Mráz, J. Emmerlich, F. Weyand, J.M. Schneider, Journal of Applied Physics 46 (2013) 135501.

[38] D. Liu, S.K. Dew, M.J. Brett, T. Smy, W. Tsai, Journal of Applied Physics 75 (1994) 8114–8120.

[39] B.R. Rogers, C.J. Tracy, T.S. Cale, Journal of Vacuum Science & Technology B: Microelectronics and Nanometer Structures 12 (1994) 2980–2984.

[40] H. Ramarotafika, G. Lemperiere, Thin Solid Films 266 (1995) 267–273.

[41] D.B. Bergstrom, F. Tian, I. Petrov, J. Moser, J.E. Greene, Applied Physics Letters 67 (1995) 3102–3104.

[42] B.R. Rogers, T.S. Cale, Y.K. Chang, Journal of Vacuum Science & Technology A: Vacuum, Surfaces, and Films 14 (1996) 1142–1146.

[43] L.B. Jonsson, C. Hedlund, I.V. Katardjiev, S. Berg, Thin Solid Films 348 (1999) 227–232.

[44] R.A. Simao, A.K. Costa, C.A. Achete, S.S.C. Jr, R. Simão, Thin Solid Films 377-378 (2000) 490–494.

[45] L.R. Shaginyan, M. Mišina, S. Kadlec, L. Jastrabı, A. Macková, V. Peřina, L. Jastrabík, Journal of Vacuum Science & Technology A: Vacuum, Surfaces, and Films 19 (2001) 2554–2566.

[46] J.-P. Palmquist, U. Jansson, T. Seppänen, P.O.Å. Persson, J. Birch, L. Hultman, P. Isberg, Applied Physics Letters 81 (2002) 835–837.

[47] M.Y. Liao, Y. Gotoh, H. Tsuji, J. Ishikawa, Journal of Vacuum Science & Technology A: Vacuum, Surfaces, and Films 23 (2005) 1379–1383.

[48] R. Lorenz, M. O'Sullivan, D. Sprenger, B. Lang, C. Mitterer, Journal of Vacuum Science & Technology A: Vacuum, Surfaces, and Films 35 (2017) 41504.

[49] M. Rausch, M. Pavlovič, P. Kreiml, M.J. Cordill, J. Winkler, C. Mitterer, Applied Surface Science 455 (2018) 1029–1036.

[50] R.F. Bunshah, Handbook of deposition technologies for films and coatings: science, technology, and applications, 2nd ed., Noyes Publications, Park Ridge, New Jersey, USA, 1994.

[51] P. Sigmund, in: R. Behrisch (Ed.), Sputtering by Particle Bombardment I: Physical Sputtering of Single-Element Solids, Springer, Berlin, Heidelberg, 1981, pp. 9–71.

[52] L.I. Maissel, R. Glang, P.P. Budenstein, Journal of The Electrochemical Society 118 (1971) 114C.

[53] Y. Matsuda, Y. Yamamura, Y. Ueda, K. Uchino, K. Muraoka, M. Maeda, M. Akazaki, Japanese Journal of Applied Physics 25 (1986) 8–11.

[54] R.S. Bailey, N.C. Hill, SPIE 2637 (1995) 56–64.

[55] F. Boydens, W.P. Leroy, R. Persoons, D. Depla, Thin Solid Films 531 (2013) 32–41.

[56] H. Oechsner, Applied physics 8 (1975) 185–198.

[57] T.P. Drüsedau, T. Bock, T.-M. John, F. Klabunde, W. Eckstein, Journal of Vacuum Science & Technology A: Vacuum, Surfaces, and Films 17 (1999) 2896–2905.

[58] K. van Aeken, S. Mahieu, D. Depla, Journal of Applied Physics 41 (2008) 205307.

[59] Landau Lifshitz, E.M., L D, Mechanics, Butterworth-Heinenann, Oxford, 1993.

[60] H. Lüth, Solid surfaces, interfaces and thin films, 5th ed., Springer, Berlin, 2010.

[61] J.A. Venables, Introduction to Surface and Thin Film Processes, Cambridge University Press, Cambridge, 2000.

[62] E. Bauer, Zeitschrift für Kristallographie 110 (1958) 372–394.

[63] B.A. Movchan, A.V. Demchishin, Fizika metallov i metallovedenie 28 (1969) 653–660.

[64] J.A. Thornton, Annual Review of Materials Science 7 (1977) 239–260.

[65] A. Anders, Thin Solid Films 518 (2010) 4087–4090.

[66] M. Zeuner, H. Neumann, J. Zalman, D. Slavínská, H. Biederman, Vacuum 51 (1998) 417–426.

[67] M.P. Allen, D.J. Tildesley, Computer simulation of liquids, Oxford university press, 2017.

[68] M.C. Payne, M.P. Teter, D.C. Allan, T.A. Arias, a.J.D. Joannopoulos, Reviews of Modern Physics 64 (1992) 1045–1097.

[69] G. Kresse, J. Furthmüller, Vienna: Vienna University (2001).

[70] K. Binder, D.M. Ceperley, J.-P. Hansen, M.H. Kalos, D.P. Landau, D. Levesque, H. Mueller-Krumbhaar, D. Stauffer, J.-J. Weis, Monte Carlo methods in statistical physics, Springer Science & Business Media, 2012.

[71] K.-H. Müller, Journal of Applied Physics 62 (1987) 1796–1799.

[72] T. Jörg, D. Music, F. Hauser, M.J. Cordill, R. Franz, H. Köstenbauer, J. Winkler, J.M. Schneider, C. Mitterer, Scientific Reports 7 (2017) 278.

[73] J.F. Ziegler, J.P. Biersack, in: D.A. Bromley (Ed.), Treatise on Heavy-Ion Science: Volume 6: Astrophysics, Chemistry, and Condensed Matter, Springer, Boston, MA, 1985, pp. 93–129.

[74] J.F. Ziegler, M.D. Ziegler, J.P. Biersack, Nuclear Instruments and Methods in Physics Research, B 268 (2010) 1818–1823.

[75] J.F. Ziegler, J.P. Biersack, M.D. Ziegler, SRIM: The stopping and range of ions in matter, SRIM Co, Chester, Md., 2008.

[76] M. Pavlovič, I. Strašík, Nuclear Instruments and Methods in Physics Research Section B: Beam Interactions with Materials and Atoms 257 (2007) 601–604.

[77] W. Dewald, V. Sittinger, W. Werner, C. Jacobs, B. Szyszka, Thin Solid Films 518 (2009) 1085–1090.

[78] H. Kupfer, R. Kleinhempel, B. Graffel, T. Welzel, T. Dunger, F. Richter, W.-M. Gnehr, T. Kopte, Surface and Coatings Technology 201 (2006) 3964–3969.

[79] A. Loop, J. Trube, M. Geisler, M. Ruske, H. Claus, Boston, Mass., USA 29–31.

[80] A. Pflug, M. Siemers, T. Melzig, L. Schäfer, G. Bräuer, Surface and Coatings Technology 260 (2014) 411–416.

[81] G.G. Stoney, Proceedings of the Royal Society A: Mathematical, Physical and Engineering Sciences 82 (1909) 172–175.

[82] G.C.A.M. Janssen, M.M. Abdalla, F. van Keulen, B.R. Pujada, B. van Venrooy, Thin Solid Films 517 (2009) 1858–1867.

[83] H.F. Winters, E. Kay, Journal of Applied Physics 38 (1967) 3928–3934.

[84] T.P. Drüsedau, F. Klabunde, P. Veit, T. Hempel, Physica Status Solidi (a) 161 (1997) 167–184.

[85] M. Andritschky, F. Guimaraes, V. Teixeira, Vacuum 44 (1993) 809–813.

[86] A. van der Drift, Philips Research Reports 22 (1967) 267–288.

[87] Y. Kajikawa, Y.K. Ã, Journal of Crystal Growth 289 (2006) 387–394.

[88] P.B. Barna, M. Adamik, Thin Solid Films 317 (1998) 27–33.

[89] T. Jörg, M.J. Cordill, R. Franz, C. Kirchlechner, D.M. Többens, J. Winkler, C. Mitterer, Materials Science and Engineering: A 697 (2017) 17–23.

[90] International Center for Diffraction Data, Powder diffraction file 03-065-7442, 2007.

[91] P.M. Martin, Handbook of deposition technologies for films and coatings: Science, applications and technology, 3rd ed., Elsevier, Amsterdam, Boston, 2010.

[92] D.M. Mattox, G.J. Kominiak, Journal of Vacuum Science and Technology 9 (1972) 528–532.

[93] A.M. Hofer, J. Schlacher, J. Keckes, J. Winkler, C. Mitterer, Vacuum 99 (2014) 149–152.

[94] D.W. Hoffman, J.A. Thornton, Journal of Vacuum Science and Technology 20 (1982) 355–358.

[95] T.J. Vink, M.A.J. Somers, J.L.C. Daams, A.G. Dirks, Journal of Applied Physics 70 (1991) 4301–4308.

[96] K.-H. Müller, Journal of Applied Physics 62 (1987) 1796–1799.

[97] C.R. Tellier, Journal of Materials Science 20 (1985) 1901–1919.

[98] T. Jörg, A.M. Hofer, H. Köstenbauer, J. Winkler, C. Mitterer, Journal of Vacuum Science & Technology A: Vacuum, Surfaces, and Films 36 (2018) 21513.

[99] F. Kunc, J. Musil, P.H. Mayrhofer, C. Mitterer, Surface and Coatings Technology 174-175 (2003) 744–753.

[100] A.G. Dirks, R.A.M. Wolters, Nellissen A.J.M., Thin Solid Films 193/194 (1990) 201–210.

[101] J. Willer, S. Pompl, D. Ristow, Thin Solid Films 188 (1990) 157–163.

[102] R. de Gryse, D. Depla, S. Mahieu, J. Haemers, Mater. Technol. 26 (2013) 3–9.

[103] D. Depla, S. Mahieu, R. de Gryse, Thin Solid Films 517 (2009) 2825–2839.

[104] M. Arif, C. Eisenmenger-Sittner, Surface and Coatings Technology 324 (2017) 345–352.

[105] M. Arif, T. Ernstbrunner, C. Eisenmenger-Sittner, Vacuum 138 (2017) 205–212.

[106] J.F. Ziegler, M.D. Ziegler, J.P. Biersack, Nucl. Instrum. Methods Phys. Res., Sect. B 268 (2010) 1818–1823.

[107] T.H. van Steenkiste, J.R. Smith, R.E. Teets, J.J. Moleski, D.W. Gorkiewicz, R.P. Tison, D.R. Marantz, K.A. Kowalsky, W.L. Riggs, P.H. Zajchowski, B. Pilsner, R.C. McCune, K.J. Barnett, Surface and Coatings Technology 111 (1999) 62–71.

[108] T. Schmidt, H. Assadi, F. Gärtner, H. Richter, T. Stoltenhoff, H. Kreye, T. Klassen, Journal of Thermal Spray Technology 18 (2009) 794–808.

[109] H. Assadi, F. Gärtner, T. Stoltenhoff, H. Kreye, Acta Materialia 51 (2003) 4379–4394.

[110] S. Grigoriev, A. Okunkova, A. Sova, P. Bertrand, I. Smurov, Surface and Coatings Technology 268 (2015) 77–84.

[111] W.D. Westwood, Sputter deposition, AVS, New York, 2003.

[112] K. Wittmaack, Journal of Applied Physics 96 (2004) 2632–2637.

[113] R. de Gryse, D. Depla, S. Mahieu, J. Haemers, Materials Technology 26 (2013) 3–9.

[114] E. Clementi, D.L. Raimondi, W.P. Reinhardt, The Journal of Chemical Physics 47 (1967) 1300–1307.

[115] J.C. Slater, The Journal of Chemical Physics 41 (1964) 3199–3204.

[116] A. van der Drift, Philips Research Reports 22 (1967) 267–288.

[117] B. Chapman, Glow discharge processes, Wiley, New York, 1980.

[118] N. Laegreid, G.K. Wehner, Journal of Applied Physics 32 (1961) 365–369.

[119] T. Jörg, M.J. Cordill, R. Franz, C. Kirchlechner, D.M. Többens, J. Winkler, C. Mitterer, Mater. Sci. Eng., A 697 (2017) 17–23.

[120] R.V. Stuart, G.K. Wehner, Journal of Applied Physics 33 (1962) 2345–2352.

[121] A.F. Holleman, E. Wiberg, N. Wiberg, Lehrbuch der anorganischen Chemie, 102nd ed., De Gruyter, Berlin, 2007.

[122] R. Hippler, M. Cada, V. Stranak, Z. Hubicka, C.A. Helm, J. Phys. D: Appl. Phys. 50 (2017) 445205.

[123] K.J.R. Rosman, P.D.P. Taylor, Pure and Applied Chemistry 70 (1998) 217–235.

[124] F. Cadieu, N. Chencinski, IEEE Trans. Magn. 11 (1975) 227–230.

[125] B. Window, N. Savvides, Journal of Vacuum Science & Technology A: Vacuum, Surfaces, and Films 4 (1986) 453–456.

[126] M. Horkel, K. van Aeken, C. Eisenmenger-Sittner, D. Depla, S. Mahieu, W.P. Leroy, Journal of Physics D: Applied Physics 43 (2010) 75302.

[127] R. Ramos, G. Cunge, M. Touzeau, N. Sadeghi, Journal of Physics D: Applied Physics 41 (2008) 152003.

[128] A. Goehlich, D. Gillmann, H.F. Döbele, Nuclear Instruments and Methods in Physics Research Section B: Beam Interactions with Materials and Atoms 179 (2001) 351–363.

[129] Y.V. Martynenko, A.V. Rogov, V.I. Shul'ga, Technical Physics 57 (2012) 439–444.

[130] R.R. Olson, M.E. King, G.K. Wehner, Journal of Applied Physics 50 (1979) 3677–3683.

[131] W. Möller, W. Eckstein, J.P. Biersack, Computer Physics Communications 51 (1988) 355–368.

[132] A.J. Detor, C.A. Schuh, Acta Materialia 55 (2007) 371–379.

[133] C. Borgia, T. Scharowsky, A. Furrer, C. Solenthaler, R. Spolenak, Acta Materialia 59 (2011) 386–399.

[134] T.J. Rupert, J.C. Trenkle, C.A. Schuh, Acta Materialia 59 (2011) 1619–1631.

[135] M. Rausch, S. Mráz, P. Kreiml, M.J. Cordill, J.M. Schneider, J. Winkler, C. Mitterer (2019).

[136] S. Berg, I.V. Katardjiev, Journal of Vacuum Science & Technology A: Vacuum, Surfaces, and Films 17 (1999) 1916–1925.